The Henryk Niewodniczański Institute of Nuclear Physics
Polish Academy of Sciences

Changes in mechanical properties of single cells in the oxygen and glucose deprivation (OGD) model

Tomasz Zieliński

A thesis submitted for the Degree of Doctor of Philosophy in Physics
Prepared under the supervision of
Prof. dr hab. Małgorzata Lekka (thesis supervisor)
Prof. dr hab. Joanna Pera (thesis supervisor)

Kraków 2023

InterDokMed

Rozprawa doktorska powstała w trakcie realizacji
Środowiskowych Studiów Doktoranckich
w ramach Projektu nr POWR.03.02.00-00-I013/16,
"Interdyscyplinarność dla medycyny innowacyjnej" InterDokMed,
realizowanych w ramach Programu Operacyjnego Wiedza Edukacja Rozwój 2014-2020, współfinansowanego ze środków Europejskiego Funduszu Społecznego

Fundusze Europejskie
Wiedza Edukacja Rozwój

Unia Europejska
Europejski Fundusz Społeczny

List of publications

Publications included in thesis:

1. A.Kubiak, **T.Zieliński**, J.Pabijan, M.Lekka, *“Nanomechanics in Monitoring the Effectiveness of Drugs Targeting the Cancer Cell Cytoskeleton.”* – **Int. J. Mol. Sci. 21 (2020) 8786.**
2. **T.Zieliński**, J.Pabijan, B.Zapotoczny, J.Zemła, J.Wesołowska, J.Pera, M.Lekka, „Changes in nanomechanical properties of single neuroblastoma cells as a model for oxygen and glucose deprivation (OGD)” – **Sci. Rep. 12 (2022) 16276**
3. **T.Zieliński**, B.Strach, J.Pabijan, B.Zapotoczny, J.Zemła, J.Wesołowska, J.Pera, M.Lekka, in preparation

Other publications:

1. J.Zemła, J.Bobrowska, A.Kubiak, T.Zieliński, J.Pabijan, K.Pogoda, P.Bobrowski, M.Lekka, *“Indenting Soft Samples (Hydrogels and Cells) with Cantilevers Possessing Various Shapes of Probing Tip.”* – **Eur. Biophys. J. 49 (2020) 485**.
2. M.Lekka, K.Gnanachandran, A.Kubiak, T.Zielinski, J.Zemła, *“Traction force microscopy – Measuring the forces exerted by cells.”* –**Micron 150 (2021) 103138.**

Abstract

Stroke is one of the leading causes of death in people over 40. Stroke is one of the leading causes of death over the age of 40. In terms of etiology, it can be divided into hemorrhagic and ischemic stroke, accounting for the vast majority of cases (about 90%). An ischemic stroke occurs when blood clots or other particles block a blood vessel's lumen, depleting supplies of fresh blood. Currently, pharmacotherapy of stroke uses drugs to dissolve the clot (recombinant tissue plasminogen activator) and restore blood flow. Despite many clinical trials and potential cures, there is still no effective therapy to protect neurons from death.

Examination of alterations in nanomechanical properties of nervous tissue and individual cells might shed light on mechanisms engaged in pathological changes present in cells during stroke exposure and understand molecular processes lying behind them. Combined atomic force microscopy (AFM) techniques, confocal microscopy, and metabolic activity analysis were applied to estimate and explain alterations in the nanomechanical properties of cells subjected to oxygen and glucose deprivation (OGD). First, the changes in the nanomechanical properties of human neuroblastoma SH-SY5Y cells exposed to OGD for 1, 3, and 12h were evaluated directly after OGD and after 24h of re-oxygenation (RO). Obtained results showed that the viability of SH-5YSY cells remained unchanged, but, in parallel, the metabolic activity of these cells decreased with OGD duration. 24h RO did not recover the metabolic activity fully. Cells subjected to OGD expressed higher deformability than control cells. Cell softening was strongly present in cells after 1h of OGD and with longer OGD duration, and in RO conditions, cells recovered their mechanical properties. Next, mice primary hippocampal neurons were exposed to OGD conditions for 1 and 3h. The results revealed a significant decrease in cell survival during prolonged OGD exposure and re-oxygenation. AFM-based assessment of nanomechanical and microrheological properties of neurons showed the increased deformability of neurons and a shift in transition frequency, suggesting alterations in the cytoskeleton and cytoplasm ion equilibrium. Confocal images confirmed disturbances in actin network organization and loss of the integrity of microtubules. Additionally, microrheological analysis confirmed alterations in a viscous

component of nanomechanical properties of neuronal cell cultures, which correlated with OGD duration.

Changes in the nanomechanical properties observed for both cell types were attributed to the remodeling of various cytoskeleton components. Understanding of cytoskeleton remodeling was mainly based on the response of actin cytoskeleton and their regulation via actin-associated protein, cofilin. In active form (unphosphorylated), cofilin is responsible for the actin cytoskeleton severing, nucleation, and branching. Each studied cell type responded differently to OGD conditions. In neuroblastoma SH-SY5Y cells, mainly a decrease in actin polymerization is responsible for the alteration in the nanomechanical properties of these cells. Cofilin activity plays a compensatory role in prolonged exposure. In the case of neurons, the cofilin activity increases, which pointed to other mechanisms of cytoskeleton activity modulation, including microtubule re-organization, and cytotoxic cell swelling. The presented study shows the importance of nanomechanics in research on ischemic-related pathological processes such as stroke.

Streszczenie

Udar mózgu jest jedną z głównych przyczyn zgonów u osób w wieku powyżej 40 lat. Pod względem etiologii wyróżnia się udar krwotoczny i niedokrwienny, ten drugi stanowi znaczną większość przypadków (około 90%). Przyczyną udaru niedokrwiennego jest zablokowanie światła naczynia krwionośnego (na przykład skrzepliną) prowadzące do zablokowania przepływu natlenowanej krwi przez tkankę. Obecnie w terapii udaru stosuje się leki rozpuszczające skrzeplinę (rekombinowany tkankowy aktywator plazminogenu) i przywracające przepływ krwi. Pomimo wielu badań klinicznych i setek potencjalnych leków, wciąż nie ma skutecznej terapii opartej na neuroprotekcji.

Badanie zmian właściwości nanomechanicznych tkanki nerwowej oraz poszczególnych komórek może rzucić światło na mechanizmy zaangażowane w patologiczne zmiany zachodzące w komórkach podczas udaru i zrozumieć procesy molekularne, które za nimi stoją. Do oceny i wyjaśnienia zmian właściwości nanomechanicznych różnych modeli komórkowych zastosowano połączone techniki mikroskopii sił atomowych (AFM), mikroskopii konfokalnej i analizy aktywności metabolicznej. Pierwszy model oparty jest na modelu komórkowym SH-SY5Y ludzkiej neuroblastomy. Komórki poddano deprywacji tlenu i glukozy (OGD) przez 1, 3 i 12 godzin. Ich odpowiedź biomechaniczną badano bezpośrednio po ekspozycji na OGD i po 24-godzinnej reoksygenacji (24h RO). Uzyskane wyniki wykazały, że żywotność SH-SY5Y pozostała niezmieniona, ale równolegle aktywność metaboliczna komórek zmniejszała się wraz z czasem trwania OGD. Po 24h RO nie zaobserwowano powrotu do pełni aktywności metabolicznej. Komórki poddane OGD wykazywały wyższą deformowalność niż komórki kontrolne. Zwiększenie deformowalności komórek było silnie obecne w komórkach już po godzinnym OGD, a w warunkach 24h RO deformowalność komórek była na poziomie deformowalności komórek kontrolnych.

Drugi model, oparty na mysich pierwotnych neuronach hipokampa, które były komórkami traktowanymi w warunkach OGD przez 1 i 3 godziny, wykazał znaczne zmniejszenie przeżywalności komórek podczas przedłużonej ekspozycji na OGD i reoksygenacji. Badania AFM, analogicznie do modelu SH-SY5Y, wykazały zwiększoną deformowalność komórek. Analiza za pomocą mikroskopu konfokalnego potwierdziła

zaburzenia w organizacji sieci aktynowej oraz utratę integralności mikrotubul. Dodatkowo analiza mikroreologiczna potwierdziła zmiany we własnościach lepkich neuronów, korelujące z czasem trwania OGD.

Zmiany właściwości nanomechanicznych obu modeli komórkowych przypisano przebudowie różnych składników cytoszkieletu. Zrozumienie przebudowy cytoszkieletu opierało się głównie na odpowiedzi cytoszkieletu aktynowego i jego regulacji przez białko związane z aktyną, kofilinę. W postaci aktywnej (nieufosforylowanej) kofilina odpowiada za przecięcie, zarodkowanie i rozgałęzienie cytoszkieletu aktynowego. Zastosowane modele w różny sposób reagują na warunki OGD. W komórkach SH-SY5Y za zmianę właściwości nanomechanicznych odpowiedzialny jest głównie spadek polimeryzacji aktyny. Aktywność kofiliny odgrywa rolę kompensacyjną w przedłużonej ekspozycji. W modelu neuronalnym aktywność kofiliny wzrasta, istnieje jednak wiele innych mechanizmów modulacji aktywności cytoszkieletu, w tym reorganizacja mikrotubul oraz wzrost objętości komórek (tzw. *cell swelling*). Przedstawione badanie pokazuje znaczenie nanomechaniki w badaniach nad procesami patologicznymi związanymi z niedokrwieniem, takimi jak udar.

List of abbreviations

2D – two-dimensional

3D – three-dimensional

AFM – atomic force microscopy

ARAC – Cytosine β-D-arabinofuranoside hydrochloride - used in B27/neurobasal-A medium to inhibit the growth of glial cells

ATRA – All Trans Retinoic Acid – used in differentiation into neuron-like cells of SH-SY5Y cell line

B27 – supplement - a complex mixture of antioxidant enzymes, proteins, vitamins, and fatty acids that are combined in optimized ratios to support neuronal survival in culture

BBB - the blood-brain barrier

C cells – control cells

Cyto D – cytochalasin D

DMEM – Dulbecco's Modified Eagle's Medium containing 4500 mg/L of glucose (high glucose

DMEM(-G) – Dulbecco's Modified Eagle's Medium containing no glucose

DPBS – Dulbecco's Phosphate Buffered Saline

FBS – Fetal Bovine Serum

GlutaMax – supplement of cell culture

HBSS - Hank's Balanced Salt Solution

LD – LIVE/DEAD Assay

LDH – Lactate Dehydrogenase Assay

L-GLN – L-glutamine

MTS – CellTiter 96® AQueous One Solution Cell Proliferation Assay

NB(+G) – Neurobasal Culture Medium containing 4500 mg/L of glucose

NBA(-G) – Neurobasal A experimental medium – without glucose and sodium pyruvate

NFs - neurofilaments

NTC – non-treated cells

OGD – Oxygen and Glucose Deprivation

PI – propidium iodine

RO – re-oxygenation in the presence of glucose and oxygen

Acknowledgments

The possibility of doing a Ph.D at the Institute of Nuclear Physics, Polish Academy of Sciences, gave me many chances to expand my knowledge and build scientific experience; therefore, it was quite challenging and cost a lot of effort. Without the support and presence of many people, it probably could not have been accomplished.

First of all, I would like to express my sincere gratitude to my advisor, the head of Department of Biophysical Microstructures Prof. dr hab. **Małgorzata Lekka** for the continuous support of my Ph.D. study and related research, for her patience, motivation, and immense knowledge. Without your support, this thesis could never arise. I could not have imagined having a better mentor for my Ph.D study. I would like to thank Prof. dr hab. **Joanna Pera**, my second advisor, for precious ideas and suggestions on neuroscience.

I would like to thank all my colleagues from the Department of Biophysical Microstructures. **Joanna Pabijan**, **Barbara Orzechowska**, **Bartłomiej Zapotoczny**, **Andrzej Kubiak**, **Kajangi (Kanji) Gnanachandran**, **Renata Szydlak**, **Marcin Luty**, **Joanna Zemła**. I would like to thank you all for your support and precious advice in projecting experiments, for help writing manuscripts, and for your presence.

I would like to express special gratitude to my Mom, **Bożena**, Dad, **Marian**, and brother **Maciej**. Your belief in my work and chosen career path gave me additional motivation in hard moments. I always knew I could rely on you.

Table of content

1. Introduction

The development of advanced spectroscopic techniques, such as force-volume elasticity estimation and microrheology analysis of visco-elastic properties, allows for estimating changes in nanomechanical properties of living cells under specific conditions such as drug treatment or oxygen and glucose deprivation (OGD) exposure. Alterations of nanomechanical properties might predict the occurrence of some diseases before the first visible symptoms. A good example of this relation is studies applied in the murine model of multiple sclerosis [1]. On the other hand, spectroscopy techniques applied in verifying disease progression might be involved in better recognizing and evaluating invasiveness and cancer progression. Many types of tissue, including nervous tissue, exhibit mechanosensitivity, the response to changes in visco-elastic properties of the surrounding environment. There is a chance that identification and understanding of nanomechanical changes will allow obtaining knowledge about pathology and potential ways of treating many disorders, including stroke and cancers. In the case of cancers, studies confirmed higher deformability compared to their normal, healthy counterparts [2-4]. It is particularly significant for cancer development as recent data have demonstrated the importance of mechanical forces in the formation of metastasis [5,6]. One technique that enables the measurement of the biomechanical properties of cells in conditions mimicking natural ones is atomic force microscopy (AFM).

The presented thesis is organized in the following order. **Chapter 1** introduces basic information about stroke, including statistics and descriptions of *in vivo* and *in vitro* models of stroke applied description of cell cytoskeleton structure and molecular pathways involved in the cytoskeleton remodeling after stroke exposure. This chapter highlights the importance of using different models to study particular aspects of short- and long-term alterations. In **Chapter 2**, the main objectives of the thesis are presented. **Chapter 3** presents the characteristics of the cells (three immortalized cell lines: HeLa, U118 MG, SH-SY5Y cells, and mice primary hippocampal neurons) used during the study. It also describes experiments inducing OGD and procedures for assessing metabolic activity and cell viability, including MTS and LDH assays, live/dead staining, and cofilin/phospho-cofilin assay (cell-based ELISA and Western blot). It also presents the techniques used in the presented research, i.e., fluorescence and confocal microscopy and atomic force microscopy (AFM), including a detailed description of data analysis and image processing. Finally, statistical methods applied in the thesis are described. **Chapters 4, 5, and 6** gather all results obtained during this Ph.D. work. **Chapter 4** treats the importance of cell morphology, in particular actin cytoskeleton architecture, in the nanomechanical properties of cells. The other two chapters describe the nanomechanical response of cells to OGD for neuroblastoma SH-SY5Y non-differentiated cells and mice primary hippocampal neurons, respectively. Cofilin activity was postulated as the main factor responsible for the alterations in nanomechanical properties. In **Chapter 7**, the obtained results are gathered and discussed. They are explained, including additional modulation of nanomechanics dependent on other factors, including microtubule organization, cytoskeleton tension governed by myosin light chain (MLC) activity, and cytoplasm pressure combined with cytotoxic cell swelling, in the neuronal model.

1.1. Stroke – basic information

A stroke is a condition in which impairments in blood flow cause brain damage due to a lack of nutrient supply like oxygen and glucose [7]. Two types of stroke can be distinguished: hemorrhagic and ischemic (**Figure 1.1.**). Regardless of the type of stroke, the brain cannot function properly, leading to losing body control and functioning. Such symptoms as a loss of body balance, problems with seeing, face drooping, slurred speech, and arm or leg weakness can be observed [8].

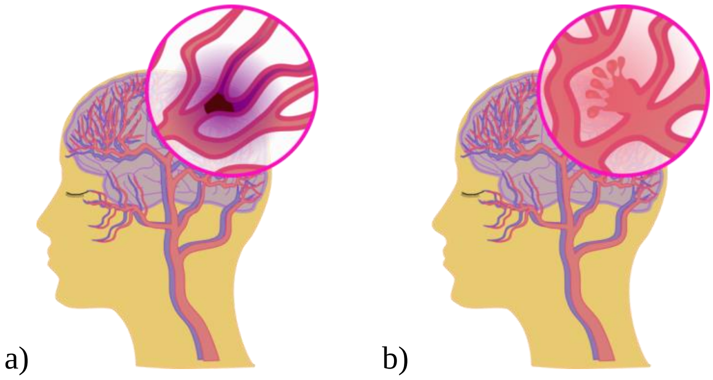

Figure 1.1. Scheme describing the direct cause of two types of stroke **a)** ischemic stroke caused by a blockage in blood flow to the brain by a clot, and **b)** hemorrhagic stroke caused by loss of artery integrity and sudden bleeding (inspired from: https://healthjade.net/cva-stroke/)

A hemorrhagic stroke occurs after loss of artery integrity that causes bleeding into the brain. This type of stroke is less frequent (10-15% cases) than ischemic stroke, which is caused by a blockage of the blood vessels in the brain. A disrupted blood flow results in oxygen and glucose deficiencies in the surrounding cells [9].

Every 8 minutes, a stroke event in Poland is noted, which results in over 60,000 cases per year [10]. Worldwide, the number of strokes exceeds 15 million cases annually. One person is estimated to die from a stroke every 6 seconds globally, and more than 5 million people annually [11]. A statistical analysis shows that stroke is 2nd cause of second leading cause of death and the third leading cause of disability [12]. The last three decades have significantly improved treatments for this disease, resulting in increased life expectancy after treatment and rehabilitation [13,14]. Currently, one of the treatment methods applies thrombolytic drugs such as recombinant tissue plasminogen activator (rtPA) [15]. This therapy can be applied in approximately 10% of patients. The second method is mechanical thrombectomy, which involves removing the clot [16]. Although there are already over 1026 potential drugs and nearly 200 in clinical trials, there are no effective therapies based on neuroprotection [17].

1.2. *In vivo* models of stroke

In *in vivo* studies, mainly rodent and non-human primates are applied to model ischemic stroke. Using appropriate animal models of human diseases is crucial in understanding pathology and proposing effective treatment strategies. Humans from rodents differ by 10% in the genome and about 300 genes [18]. Some essential differences in the nervous system are *(i)* the expression levels of transporters and ionic pumps located at the blood-brain barrier (BBB), and *(ii)* the functional diversity and abundance of astrocytes [19]. Additionally, rodents (especially mice) exhibit different duration of excitotoxicity in comparison to humans [20]. Importantly, the immune system plays a role in restoring brain functions within the brain region affected by stroke. This points to differences in the immune systems of rodents and humans linked with the inflammatory response to stroke. Such signaling molecules as interleukin-8, chemokine (C-X-C motif) ligand 7, chemokine (C-C motif) ligand [CCL] 18, monocyte chemoattractant protein-4 and CCL24/CCL26) are only expressed in humans. Such molecules as CCL6, CCL9, and monocyte chemoattractant protein-5 are present only in mice [18]. These differences may result in various, not always needed, and expected effects of potential therapeutics.

In vivo studies apply two major ischemic models, i.e., "*global*" and "*local (or focal)*" ischemia. Induction of the global ischemia is frequently performed by ligating for 5–15 min the vertebral arteries (two-vessels), carotid arteries (two-vessel occlusion, 2-VO), or both (four-vessel occlusion, 4-VO) [21-23]. It results from the total cessation of cerebral blood flow, and usage of this model is mainly focused on hippocampal damage. Its significant advantage is the possibility of investigating metabolic alterations after restoring blood flow [24,25]. The two-vessel occlusion method (occlusion of both common carotid arteries) is coupled with hypotension to produce ischemia in the forebrain region [23]. Focal models can give insight into many stroke symptoms more closely than global models. Cell death in stroke-affected tissue accrues in a time and region-dependent manner, a primary insult to a specific set of cells within the targeted brain region – the infarcted core, and secondary symptoms resulting in cell death (i.e., oxidative stress, inflammation, mitochondrial dysfunction, altered synaptic plasticity) to neighboring tissue – referred to ischemic penumbra. Stroke in the cortex and striatum can be conducted by applying a ligation or occlusion of the proximal and distal middle cerebral artery (MCA) using sutures/filaments [26], coagulation/ligation of MCA [27,28], photothrombotic approaches (rose Bengal – after injection, irradiating the exposed region with green light (560 nm) induces thrombotic plugs [29,30]), and arterial or intracerebral placement of autologous blood and clot-forming agents [31].

Rodent stroke models allow for the simulation of complete and transient occlusion; however, clinical stroke is not precisely described because complete occlusion rarely occurs. Typically, their spontaneous recanalization is observed. In most studies, the stroke model is applied to healthy animals. In contrast, in humans, age and multiple other factors such as hypertension, diabetes, hyperlipidemia, heart disease, patients' medications, etc. [32-34] can play a crucial role in stroke pathophysiology and response to therapeutics. For a close approximation of accrued pathology and preclinical readouts of novel therapies, consideration of the factors mentioned above is necessary for further conclusions.

The procedure of stroke induction itself is prone to factors such as a high rate of variability with the location and size of the lesion [35-40]. More limitations of rodent models are mentioned below. The first factor is connected with the difficulty in visualizing the MCA occlude placement; however, it has mostly been solved by applying flowmeters [41,42]. Using models in acute stroke neuroprotection studies requires functional assays for determining safety and efficacy profiles with short animal survival times [43]. Additionally, for prolonged studies of therapeutics efficiency, longer survival of animals after ischemia exposure and blood flow restoration is required. Important limitations in the application of rodents in ischemic stroke studies are anatomical differences in vascularity and brain anatomy compared to humans. Therefore, the design of experiments in translational studies should include sample size, randomization, investigator bias, and treatment condition blinding, all of which should allow for the avoidance of confounding variables that may decrease the effectiveness in further clinical applications [44,45].

Compared to rodent models, non-human primates (NHP) models give many advantages according to their vascular anatomy, including anatomically and genetically higher relevance [46]. Currently used NHP models include squirrel monkeys, macaques, and baboons. However, translation studies from primates to humans must also be carefully verified. For example, the clinical trial of theralizumab (TGN1412, a humanized monoclonal antibody binding to the CD28 receptor on T lymphocyte surface) almost resulted in the deaths of 6 healthy volunteers because of differences in binding characteristics between humans and rhesus monkeys, which resulted in a severe inflammatory response [47]. *In vitro* studies of the effect of theralizumab on human peripheral blood mononuclear cells and activated human T cells have shown that enhanced cytokine release evaded previous preclinical trials [47,48]. Drug safety regulations require that all data obtained on animal models must be reproduced using a proper human *in vitro* model [49]. Some research groups focus on human tissues provided during neurosurgeries. The latter approach constitutes the human models; however, such models are not always accessible.

1.3. *In vitro* stroke models

Understanding processes occurring during stroke exposure are often conducted at the cellular level using OGD, which is also successfully applied in ischemic cell death studies [50]. In the OGD models, cells, tissue slices, or other samples can be exposed to reduced oxygen (hypoxia) or total lack of oxygen (anoxia) and cultured in glucose-deprived media. Additionally, the effect of media exchange and re-oxygenation/reperfusion has to be considered. With prolonged OGD exposure, the re-oxygenation may paradoxically result in inducing further damage to cell functioning. For example, ischemia-reperfusion injury is linked with the immediate generation of reactive oxygen species and calcium influx [51].

Ischemic stroke can be mimicked in cell cultures by applying chemical, enzymatic methods (enzymatic inhibition of cell metabolism) or by OGD with accompanying reperfusion/re-oxygenation (restoration of oxygen and glucose) [52]. Applying combined inhibition of glycolysis and cell respiration allows for obtaining *in vitro* chemical model of stroke. Comparing this method with OGD lasting for 1 hour followed by 3-hour reperfusion resulted in higher reproducibility and efficiency than OGD [52]. Chemical and enzymatic methods encounter high throughput, easy application techniques, with high relevance and rapid response (chemical hypoxia results in a larger generation of free radicals than anoxia), there does not allow investigations of alterations in cell metabolism, and regeneration processes occur in cells during reperfusion. Ischemic conditions can also be generated by replacing the O_2/CO_2 equilibrated culture medium with N_2/CO_2 equilibrated one, followed by maintaining cell culture in a hypoxic chamber in a 95% N_2 and 5% CO_2 atmosphere. Typically, oxygen deprivation is accompanied by glucose deprivation. Hypoxia alone can significantly alter the actin cytoskeleton and tight junctions of endothelial cells in BBB models [53]. Glucose deprivation alone is rarely applied in modeling stroke because of its low efficiency (> 4 hours does not significantly affect rat cortical neurons) [54]. Acute cell body swelling, provoked by combined oxygen and glucose deprivation, has already been observed in primary neurons leading to acute cell body swelling, followed by excitotoxic necrotic and apoptotic cell death [55,56], despite a return to standard culture conditions supplemented with both oxygen and glucose [57]. The large increase in extracellular glutamate concentration consistent with excitotoxic effects *in vivo* is also observed during OGD in primary mouse cortical neurons [57].

Investigation of ischemic pathology and potential neuroprotective drug efficiency can be performed by applying various samples providing cell-cell interaction and tissue organization [58]. The study of thin brain slices (≈ 400 μm) allows for investigating brain cell interactions [58,59]. Rodent brain slices were maintained for ≤ 12 hours under perfusion with artificial cerebral spinal fluid. OGD induction was conducted by replacing oxygen with nitrogen and removing glucose. The use of slices allowed for investigating various cell types in nervous tissue and the effects of ischemia from cerebrovascular influence [59,60]. In the other method, human cortical slices were studied in search of evidence of glutamate receptor involvement in ischemic injury in the human brain [61]. Usage of human material is rare and limited to samples collected during neurosurgeries of young epileptic patients. This experimental group cannot be directly treated as physiological. Additionally, they do not represent a group prone to stroke events; however, they are still precious in translational studies.

Organotypic *ex vivo* cultures can be obtained from neonatal animals and allowed to mature *in vitro*. Apart from structural preservation, many cultures exhibit synaptic rearrangement caused by a lack of extrinsic afferent and efferent signals *in vitro* [62]. These cultures are widely used for investigating neuronal cell death, myelination, synapse plasticity, and potential stroke therapies after OGD.

The application of primary cells gives many advantages. In the context of AFM studies, primary neurons reflect more closely the morphology and physiology of hippocampal neurons in nerve tissue. However, terminally differentiated primary cells and their inability to replicate diminish the efficient usage of the model in high throughput studies. Isolation and purification of cells are time-consuming, and the amount of cells is limited. Additionally, primary cells exposed to nonphysiological conditions of 2d culture might also lose their phenotype [63,64].

Immortalized cell lines allow the introduction of high throughput studies on the human model in vitro, reducing complications combined with different gene expression profiles. According to present studies, many models were introduced, including immortalized human microglia cells displaying various inflammatory responses typical for the primary cells. Further conclusions should consider the presence of oncogenes that distinguish them from endogenous cells by increased proliferation, cell adhesion, and variance of morphologies. Sometimes, cells derived from different human body parts are considered neural cell models. SH-SY5Y neuroblastoma cells are a good example of this statement. These are adrenergic and dopaminergic cells derived from cells of a bone marrow biopsy taken from a 4-year-old patient with neuroblastoma [65]. Additionally, both non-differentiated and differentiated SH-SY5Y cells have their advantages and drawbacks in the model of neuron cells [66]. The human-origin cell line allows for a better reflection of the stroke-induced alterations and testing of potential drug therapy. For further clinical studies, it is necessary to obtain proper models of drug targeting through the Blood Brain Barrier. In *in vitro* studies are applied various types of *in vitro* BBB models, including nonhollow fiber-based microfluidic models [67].

Another cellular model is embryonic stem cells. In principle allow the application of high throughput studies on every cell type in vitro. Many methods were applied to obtain lineage-restricted neural progenitor cells for their further specific differentiation into neurons, astrocytes, or oligodendrocytes [68]. The application of embryonic stem cells is facing some crucial issues, including ethical limitations of human embryonic stem cell usage and the introduction of oncogenes. Partially these problems have been solved by obtaining efficient and safe methods of reprogramming somatic cells into induced pluripotent stem cells (iPSCs) [69,70]. Furthermore, it is possible to obtain fully differentiated iPSC cells to neurons with around ≈ 100% purity of cells [71].

Independently from the applied *in vitro* model, there are still only a few studies focusing on changes in nanomechanical properties and their importance in the context of stroke. Various studies confirmed nervous tissue and cells as mechanosensitive and able to respond to alterations in the biomechanical properties of surrounding tissue [72]. However, there is no sufficient information about changes in mechanical properties and the response of neurons to stroke conditions.

1.4. The structure and organization of cell cytoskeleton

The cell cytoskeleton supports cellular functions such as cell morphology, cell migration, cell division, and intracellular transport [73]. Its action is regulated by the polymerization and depolymerization of cytoskeletal elements through various associated proteins. Almost all eukaryotic cells possess a cytoskeleton, which consists of three major fibrous components, i.e., microfilaments (actin filaments), intermediate filaments, and microtubules (**Figure 1.2).**

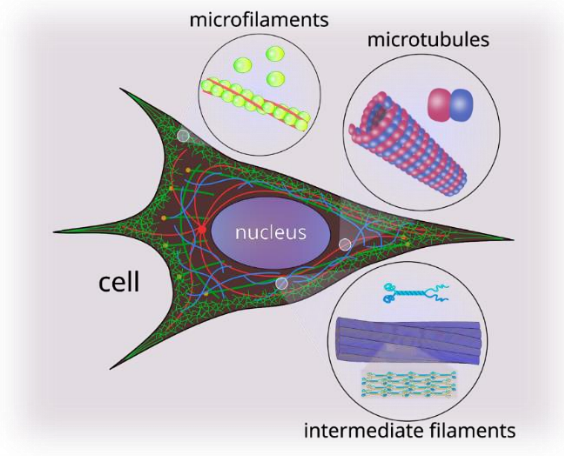

Figure 1.2. Scheme showing localization, morphology, and interactions of three main filamentous structures of cell cytoskeleton: intermediate filaments, microtubules, and microfilaments.

These filaments are composed of proteins, i.e., actin in the case of actin filaments, tubulin in the case of microtubules, and vimentin or keratin in the case of intermediate filaments.

Microfilaments (actin filaments) are composed of actin that polymerizes into a fibrous structure with a diameter of 7 nm. In cells, these filaments are mainly present beneath the cell membrane in two forms [74,75], i.e., a meshwork composed of a short polymerized form of actin (F-actin) and bundles of parallel organized fibers that may span over the whole cell body (in specific case they are called stress fibers). Microfilaments, assembled from monomeric actin (G-actin), form twisted strands interacting with various actin-associating proteins, including, for example, that of the tropomyosin family. Microfilaments are characterized by a polar organization with fast-growing "*barbed*" and slow-growing "*pointed*" ends. Regulation of actin cytoskeleton dynamics depends on many actin-associated proteins such as filament crosslinkers, promoters, and inhibitors of actin monomer assembly. The continuous control between G-actin and F-actin amounts that translates into the balance between polymerization and depolymerization leads to a dynamic equilibrium state. By this, cell architecture and mechanical resistance are maintained by employing various actin-binding proteins [76,77]. Microfilaments regulate various biological processes, including cell migration, division, and vesicle trafficking. In neurons, numerous studies have demonstrated the critical role of the actin cytoskeleton in neurite outgrowth, neurite regeneration, and synapse function.

Intermediate filaments comprise various proteins forming a fibrous structure of about 10 nm. They exhibit nonpolar characteristics, whereas microfilaments and microtubules show polarity in their organization. The role of these cytoskeletal components is to establish a structural framework and support dynamic processes such as the transport of molecules and organelles during cell migration. Additionally, they provide mechanical resistance toward tension or stretching by distributing the forces over a cell body [73]. In the nervous system, intermediate filaments are named by the term neurofilaments [78]. They are heteropolymers composed of four subunits classified depending on the apparent molecular mass. There are light (NF-L), medium (NF-M), and heavy (NF-H) neurofilaments. Neurofilaments are mainly thought to be responsible for controlling axonal growth [79,80], their conduction velocity [81,82], or maintaining mitochondrial stability [83].

Microtubules form a tube, which is long, empty inside, and very dynamic. The diameter of a single microtubule is around 25 nm. Their polar organization enables the transport of proteins by the coordinated assembly of α/β-tubulin dimers leading to the formation of fast-growing plus and slow-growing minus ends. In most eukaryotic cells, microtubules are formed in the centrosome (a microtubule organizing center) located close to the cell nucleus and grow towards the cell membrane [84]. They play a crucial role in the organization of molecular complexes and organelles within the cytoplasm. Members of the motor protein families, like kinesins and dyneins, responsible for plus-end-directed and minus-end-directed transports, drive cargo transport along microtubules.

All cytoskeletal components (microfilaments, intermediate filaments, and microtubules) interact by employing numerous linker proteins between the filaments or through shared signaling pathways. For example, neurofilaments interact with microtubules during the transport of NFs (neurofilaments) via dynein and kinesin motors along microtubule tracks [85-87]. Neurofilament proteins also interact with microtubule-associated protein 2 (MAP2), showing a direct link between these filament systems [89-90].

Communication and interaction of microtubules and actin cytoskeleton are crucial in neuritogenesis [91]. The application of drugs (taxol, nocodazole, latrunculin A, and cytochalasin B) changes the organization and dynamics of one cytoskeletal system, like microfilaments or microtubules. Inhibition of the polymerization of one of the fibrous networks can lead to changes in the branching of neurons [92]. It is because many actin-associated proteins interact with microtubules or play a regulatory role like it is in the case of the formin family of proteins [93] or microtubule plus-end-tracking protein (CLIP-170, [94,95]). Microtubule-associated proteins (MAP1, MAP2, and tau). MAP1 proteins are also engaged in interactions between microtubules and actin filaments. Their role is essential in the development and elongation of axons [96]. Additionally, in primary hippocampal neurons, changes in the distribution of tau protein have already been reported during microtubule disruption and by cytochalasin-induced depletion of filamentous actin [97].

1.5. The activity of small GTPases and cofilin involvement

The Rho[1]-family of small GTPases[2] regulates numerous cellular processes such as motility, mitosis, proliferation, and apoptosis [98-104]. Rho GTPases function as molecular switches and interact with downstream effector molecules to propagate the signal transduction in their GTP (guanosine triphosphate) loaded "*on*" state. In contrast, the activity of intrinsic phosphatase hydrolyzes the GTP to GDP (guanosine diphosphate), turning the protein "*off*" [105,106]. The role of small GTPases in neurons lies in controlling distinct aspects such as neurite outgrowth, the protrusive behavior of growth cones, addition and retraction of neurite branches, attenuation of neurite extension, and growth cone collapse [107].

GTPases act through various downstream effectors on the microfilament and microtubule systems. The downstream targets of Rho include kinases, formins, families of WASp proteins, and other scaffolding molecules [108]. Including these subclasses, direct effects on actin cytoskeleton rearrangements resulting in modulation of motility, exhibit the Rho-associated coiled-coil kinase1/2 (ROCK), the p21-activated kinase (PAK), the mammalian Diaphanous formin (mDia) and proteins of the WASp family including WASp, N-WASp and WAVE. RhoA, B, and C activate the immediate downstream kinase target ROCK, which is responsible for the direct phosphorylation of numerous actin cytoskeleton regulators, including myosin light chain phosphatase and LIM kinase (LIMK) [109,110]. Phosphorylation of the myosin light chain and myosin

---

[1] Rho – The Ras homologous protein family

[2] GTPases are a large family of hydrolase enzymes binding to the nucleotide guanosine triphosphate (GTP) and hydrolyzing it to guanosine diphosphate (GDP).

light chain phosphatase alters the phosphorylated myosin light chain level, leading to contractility changes [111].

Activation of LIMK by ROCK is combined with the activity of the ADF[3]/cofilin protein family [110,112-114]. The ADF/cofilin family regulates microfilament dynamics by severing, nucleation, and capping within the protrusive machinery [115-121]. Cofilin participates in the process of forming an actin nucleus consisting of three actin monomers from which actin filaments elongate. It binds to filamentous (F-actin) and monomeric (G-actin) actins with high affinity with a preference for ADP[4]-actin [101-103] and regulates actin cytoskeleton structure by increasing the dynamics of filament assembling and/or disassembling. Modulation of microfilaments conformation is realized by accelerating the dissociation of actin monomers from the filament-pointed end [106] and severing existing filaments [122], regulating protrusive dynamics in the leading edge [123-126], cell motility [98,127], cytokinesis [99], and endocytosis [100]. Additionally, ADF/cofilins increase the dissociation of phosphate from ADP-Pi[5] filaments and promote the debranching of the Arp2/3[6]-nucleated actin filament network [128,129]. Cofilin activity is regulated by direct phosphorylation at Ser3 through the LIMK [121]. For dephosphorylation of the inactive form (phospho-cofilin) into active form ale responsible Slingshot and Chronophin family of phosphatases activated by Rac1[7] [130,131]; however, the coordination of multiple pathways governing its regulation seems to be unclear.

Studies performed on the Swiss3T3 cell line revealed that microinjection of the activated mutants of Rho GTPases into starved and quiescent cells significantly altered actin cytoskeletal structure and organization [98,99,127,132,133,134]. In the brain, OGD affects the actin cytoskeleton leading to blood-brain barrier disruption and alterations in endothelial cells [135], non-neuronal brain cells [136], and neurons [137]. Reported changes might mainly involve cofilin-based regulation. As an actin-depolymerizing factor, cofilin was highlighted to participate in the actin remodeling in axons [137-139]. In ischemia-induced actin disruption, cofilin activity is connected with ATP depletion

---

[3] ADF – actin depolymerizing factor

[4] ADP – adenosine-di-phosphate

[5] ADP-Pi – ADP with inorganic phosphate

[6] Arp2/3 – actin related protein 2/3 complex

[7] Rac1 – human Ras related C3 botulinum toxin substrate 1

[140]. Cofilin plays a crucial role in an early phase of apoptosis [140] and intracellular contractile force generation [141]. The role of cofilin regulation in many pathological processes and diseases make this protein a potential target for neuroprotective approaches in the early stages of ischemic brain injury.

1.6. Biomechanics of cells using atomic force microscopy (AFM)

The development of various advanced biophysical methods enabled the nanomechanical characterization of biological samples. To these techniques belongs atomic force microscopy (AFM), [4,142-144] magnetic twisting cytometry [145], magnetic [146], or optical tweezers [147], and micropipette aspiration [148]. AFM was developed in 1986 [149] and belonged to the family of scanning probe microscopy (SPM) techniques [150]. AFM was initially established as a technique for the morphology analysis of nanometer-size objects. With time, it has been widely applied in biological studies [151]. AFM is a widely used technique that combines nanoscale and high-resolution imaging to determine the nanomechanical properties of cells and tissues [152]. Additionally, AFM has an important advantage compared to other microscopy techniques. They are linked with sample preparation, as dehydration, surface coating, or labeling are not required. Measurements can be carried out in air, vacuum, and liquids (including culture media) [153]. Depending on the interaction of the AFM tip with the sample, contact (the tip is in contact with the sample surface), tapping (the tip–surface interactions are minimized), and non-contact (the cantilever oscillates at a certain distance from the surface) modes of the AFM operations can be distinguished. Force spectroscopy mode, where the previously calibrated cantilever acts as a force sensor, gives insight into the nanomechanical properties of biological samples [152,153].

Despite various theoretical models, the description of the nanomechanical response of biological samples is sophisticated and requires specific simplifications [154-157]. Mostly, cells are approximated as a homogenous material without internal structure [157]. Current approaches allow comparing sufficient viscosity and elasticity of cells between various [158,159]. Mechanical properties of materials can be described by the nature of deformation generated by the external force. Elastic material exhibits resistance to external force and returns to its original size and shape after stress removal. Plastic materials exhibit different characteristics; they adapt to external forces and irreversibly change their shape. In other cases, a combination of the elastoplastic behavior is included [160]. Biological objects mainly reveal viscoelastic behavior [161-163]. Application of theoretical models is difficult; thus, very frequently, only elastic contribution is considered in further studies.

Quantifying each deformation type can be done by determining the corresponding modulus, such as Young's (elastic) modulus, which describes the resistance to a compressive or tensile force or shear modulus quantifying mechanical response to shear force [164]. Nevertheless, it is crucial not to forget the limitations of this approach. Hooke’s law is related to the linear elastic region of the material and is described by using the following equation:

$$\sigma = E\varepsilon \tag{1}$$

where: σ – the applied stress, E - a material constant called Young's modulus, ε – fractional strain. It is defined as the ratio of the stress along an axis (described as force per unit area) to the strain along that axis (calculated as deformation of the initial length) in the range where Hooke’s law is working. During stretching, a material tends to contract in the directions transverse to the direction of stretching. In this case, the fraction of relative contraction to relative expansion is called the Poisson ratio. Poisson’s coefficient value for the vast majority of materials is between 0 and 0.5. For living cells, Poisson’s ratio is approximated to 0.5. Small strains can be treated as a perfectly incompressible material deformed elastically [165,166].

Explanation of alterations in nanomechanical properties of cells and tissue usually is hidden behind disturbances in cytoskeleton organization. Mainly and most often, actin cytoskeleton remodeling is taken into consideration. Changes in the structure of actin are closely related to cell migration and invasion due to the crucial role of actin in those processes [167]. Disruption in the structure of all cytoskeleton components, which can be detected by applying AFM, results in diminished efficiency of numerous cellular processes, including transport, signaling, and support of cells.

Application of AFM in nanomechanical studies of cell cultures was performed for various cell types, including stem cells [168,169], fibroblasts [179,171], endothelial, cardiac muscle, and skeletal muscle cells [172], neurons [173], and ultimately cancerous cells [174]. Analysis of microrheological properties was applied to lung epithelial cells, which physiologically are subjected to large cyclic forces from breathing [166]. Recent studies have demonstrated that AFM can also be applied for simultaneously mapping the nanomechanical characteristics of cells, fibrous components (such as collagen), and even other non-cellular components of the tissue [175-178]. A comparison of nanomechanical properties of healthy and pathological tissue was performed on an example of Duchenne muscular dystrophy in murine muscles [179]. In further studies, AFM elasticity measurements were applied to monitor less severe muscular dystrophies and evaluate the effectiveness of the treatment [180-182]. As an excellent example of AFM, tissue studies can be mentioned in nanomechanical studies of nervous tissue in the context of stroke [183], where authors showed drop of Young's moduli in the stroke-exposed brain region. Alterations in nanomechanical properties might be the first symptom of the disease progression. Before the first visible symptoms of multiple sclerosis, spinal cord nanomechanical studies indicated early alterations [1]. In cancer studies, AFM force spectroscopy on snap-frozen mammary tissues (ex vivo) to explore the origin of the tissue stiffening associated with mammary tumor development in mice revealed that the malignant epithelium *in situ* was far stiffer than in isolated breast tumor cells [184].

The development of AFM techniques goes with the increasing demands of users, such as the ability to direct observation of biological phenomena, including dynamic cellular processes and visualization of the dynamics of biological molecules and their complexes. A good example of the application of HS-AFM was the visualization of nanoscale alterations of the nuclear pore inner channel in colorectal cancer cells [185]. The need to increase imaging speed resulted in the construction of other modes, especially High-Speed AFM (HS-AFM) [186,187]. High-speed performance was achieved thanks to the modification of crucial parts of AFM, including the electronic circuits, the sample-stage scanners, and the cantilever deflection system. Additionally, the combination of high-resolution AFM with other microscopy techniques (e.g., scanning electron microscopy [188], optical/fluorescence and confocal microscopy [189], multiphoton microscopy, and second harmonic microscopy [190] can give insight into cellular components architecture and biochemical functions [191] and can further expand AFM capabilities. In recent years, the development of AFM techniques and the number of combinations of AFM with other microscopic techniques increased, which is a good sign for the future of nanomechanical studies.

2. Aims of the thesis

Ischemic stroke remains one of the leading causes of patient death in the elderly. However, despite about two hundred clinical trials and thousand potential cures, there are still no effective neuroprotective strategies [17]. Understanding of mechanisms involved in stroke is essential in developing novel treatment or prevention strategies. Regulation of actin-associated proteins and disassembly of actin filaments might be a crucial cause responsible for actin cytoskeleton remodeling manifested as the alteration in nanomechanical properties of OGD-exposed cells. The cofilin protein family is responsible for severing actin filaments and modulating depolymerization. In physiological conditions with oxygen and glucose, the active (unphosphorylated) cofilin form enables the branching of actin in the leading edge of the cell and promotes migration. Thus, the main goals of the presented thesis focus on evaluating the alterations in the biomechanical properties of cells affected by OGD. The driving hypothesis is that alterations in metabolic activity due to depletion in oxygen and glucose alter the cytoskeleton architecture through decreased actin fiber polymerization and altered cofilin activity. These alterations are involved in the early stages of cell cytoskeleton response to ischemic conditions.

The detailed objectives are:

- Optimization methodology of study cytoskeleton reorganization, including AFM evaluations of nanomechanics and analysis of shape descriptors.
- Optimization of *in vitro* OGD for treating neuroblastoma SH-SY5Y cells and mice primary hippocampal neurons to investigate time-dependent changes.
- Nanomechanical and microrheological characterization of OGD-induced changes in living neuroblastoma SH-SY5Y cells and mice primary hippocampal neurons directly after OGD and 24h after re-oxygenation
- Characterization of OGD duration-dependent alterations in the organization of actin and microtubular cytoskeleton, followed by assessment of cell viability and metabolic activity.

- Proposing cofilin as the main player in the early stages of cell cytoskeleton remodeling manifested as the change in cell mechanics
- Evaluating nanomechanical changes in response to the stroke and understanding governing mechanisms might be crucial in developing new therapeutics targeting the cytoskeleton.

3. Materials and methods

3.1. Cell cultures

3.1.1. Human glioblastoma cell line – U118 MG

U118 MG is a cell line isolated in 1966 from malignant gliomas from a 50-year-old male with grade IV glioblastoma (a kind gift from prof. Katarzyna Rolle, Institute of Bioorganic Chemistry Polish Academy of Science, Poznań). Cells were cultured in 25 cm^2 culture flasks (TPP) in a Dulbecco's Modified Eagles' Medium (DMEM, ATCC, LGC Standards) supplemented with 10% Fetal Bovine Serum (FBS, ATCC, LGC Standards). Cells grew in the CO_2 incubator (NUAIRE) at 37°C and 5%CO_2/95% air atmosphere.

3.1.2. Human epithelioid cervix carcinoma – HeLa

HeLa cells were isolated in 1951 from a cervical carcinoma of a 31-year-old woman [192] (a kind gift from prof. Katarzyna Rolle, Institute of Bioorganic Chemistry Polish Academy of Science, Poznań). Cells were cultured in 25 cm^2 culture flasks (TPP) in an Eagle's Minimum Essential Medium (EMEM, ATCC, LGC Standards) supplemented with 10% Fetal Bovine Serum (FBS, ATCC, LGC Standards). Cells grew in the CO_2 incubator (NUAIRE) at 37°C and 5%CO_2/95% air atmosphere. The number of passages was kept below 10.

3.1.3. Human neuroblastoma cell line - SH-SY5Y

SH-SY5Y human neuroblastoma cell line was initially derived from a metastatic bone tumor biopsy [65]. SH-5YSY cells grew in 25 cm^2 culture flasks (TPP) in a Dulbecco's Modified Eagles' Medium (DMEM, ATCC, LGC Standards) supplemented with 10% Fetal Bovine Serum (FBS, ATCC, LGC Standards). Cells were cultured in the CO_2 incubator (NUAIRE) at 37°C and 5%CO_2/95% air atmosphere. The number of passages was kept below 10. This cell line was obtained thanks to a prof. Danuta Jantas from Maj Institute of Pharmacology Polish Academy of Science and prof. Halina

Jurkowska from Collegium Medicum Jagiellonian University. Undifferentiated cells grew as adherent and floating cells (**Figure 3.1.**).

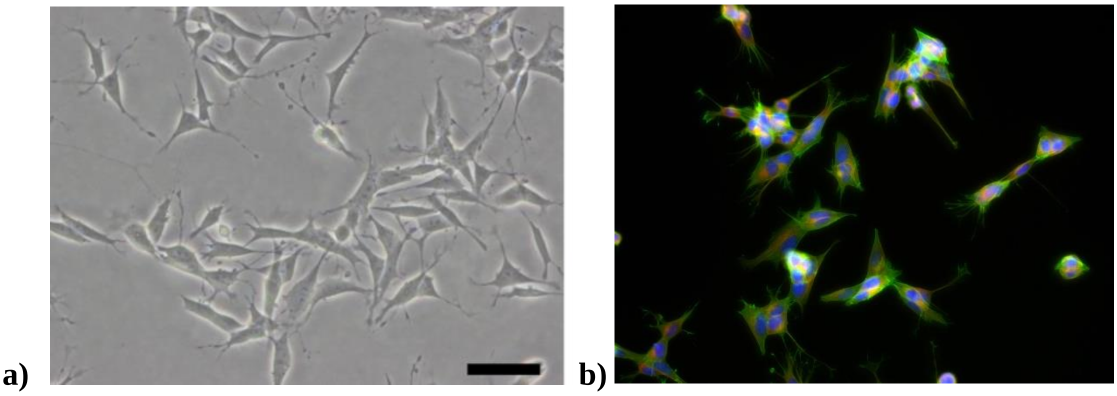

Figure 3.1. a) Phase-contrast and **b)** fluorescence image of undifferentiated SH-SY5Y cells. Fluorescence staining: actin filaments – phalloidin conjugated with Alexa Fluor 488, microtubules – primary antibody conjugated with Cy3, cell nuclei – Hoechst 33342.

Undifferentiated cells exhibit neuroblast-like non-polarized morphology (cell body with few protrusions), tend to grow in clusters, and may form clamps as cells appear to grow on top of another cell. Undifferentiated SH-SY5Y cells exhibit markers characteristic of immature neurons.

3.1.4. E18 Mice primary hippocampal neurons

Hippocampal primary neurons were isolated by mgr. Beata Strach from Collegium Medicum, Jagiellonian University, and plated to 2d culture from E18 embryos using the following protocol (isolation and culture of hippocampal neurons from prenatal mice) with some modifications [193]. To obtain prenatal pups, the breeding of adult mice (2-8 months) was conducted for 19 days before isolation. Before isolation, well plates, Petri dishes, and glass coverslips were coated with the poly-D-Lysine solution for 1h, followed by rinsing in sterile deionized water three times. During isolation, sterilization of instruments was realized by flame-cleaning. All preparations apart from initial procedures are performed under laminar flow.

Pregnant mice were euthanized by decapitation, then the uterus was opened, and the pups were removed. Pups' heads after decapitation were placed on sterile gauze under a dissecting microscope. The cranium of each pup was opened, the brains were carefully removed and placed on sterile gauze, hemispheres were separated, and dissection of the hippocampus was performed. Isolated from each pup tissue was transferred into a small tissue culture dish with warmed (37°C) Hank's balanced salt solution (HBSS) under a laminar flow. Nervous tissue, combined from multiple pups, was suspended in sterile HBSS and gently minced using a sterile scalpel, then transferred to a 15 mL conical tube. To harvest the tissue, a 0.25% solution of trypsin was added. Finally, the excess solution was carefully removed after settling the tissue on the tube, leaving the pellet at the bottom. After washing three times with 5 mL of HBSS at 37 °C for 5 minutes was removed and replaced with 2 mL of fresh HBSS. Using a completely cool (fire-polished by using Bunson burner – decreased diameter and rounded edges of pipette opening) Pasteur pipette, the tissue was gently triturated. Then the supernatant was transferred to a fresh 50 mL conical tube without larger pieces of tissue. To increase isolation efficiency, the remaining tissue was diluted with 2 mL of sterile HBSS and triturated a few times using the fire-polished Pasteur pipette.

Before plating, a 1:1 cell solution with Trypan Blue (Sigma-Aldrich) was prepared, and cells were counted using a hemocytometer. Appropriate cell number was mixed with indicated volume of neurobasal medium (Neurobasal+ medium containing B27 supplement (1 mL/50 mL), 0.5 mM glutamine solution, 25 μM glutamate (M_w = 147.13 g/mol), penicillin (10000 units/mL)/streptomycin (10000 μg/mL) (250 μL/ 50 mL), 1 mM HEPES (M_w = 238.3 g/mol), 10% heat-inactivated donor horse serum (HI-DHS) and plated with gentle swirling on previously prepared plastics at the density of 50000 cells/cm^2. HI-DHS was added to the plating media to enrich the cells during the first 24 hours of growth, then subsequently removed by serial reduction of the serum at each media replacement. Every 3 days of culture, half the volume of media from the cells is replaced with the same volume of the neurobasal medium. After 7 days of conditioning (37°C, 5% CO_2 incubator), neurons were stained for actin, microtubules, and cell nuclei (**Figure 3.2**).

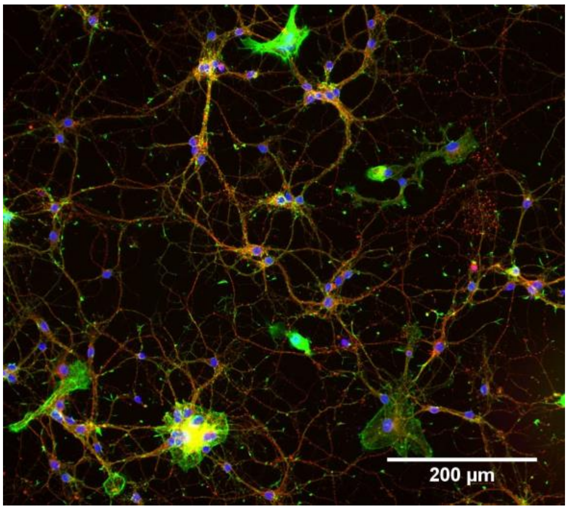

Figure 3.2. Image showing mice primary hippocampal neurons after 7 days of culture, plated on previously coated with poly-D-lysine plastic Petri dish. Actin filaments – phalloidin conjugated with Alexa Fluor 488, microtubules – primary antibody conjugated with Cy3, cell nuclei – Hoechst 33342

3.2. OGD experiments

3.2.1. Time scale of OGD for neuroblastoma SH-5YSY cells

SH-SY5Y cells were passaged from the culture flask to the plastic Petri dish, 12-well plate, or 24-well plate (TPP) and kept in the CO_2 incubator (37°C and 5%CO_2/95% air atmosphere) for 24 hours in the high glucose (4500 mg/L), DMEM containing 1 mM sodium pyruvate (ATCC, LGC Standards) supplemented with 10% FBS. After plating, the medium was replaced with neurobasal A medium (NBA, without glucose), and samples were placed in the able CO_2 incubator (Olympus) at 37°C. The atmosphere was kept at 5% CO_2, 0.1% O_2, and 94.9% N_2 maintained constant for 1h, 3h, and 12h for SH-SY5Y cells. Parallelly, control groups were rinsed with neurobasal medium containing glucose (NB) and in an atmosphere of 5% CO_2, 18% O_2, and 77% N_2. After OGD and parallel to control conditioning, cells were exposed to 24h re-oxygenation/conditioning in culture conditions in DMEM containing glucose. The time scale of the experiments is shown in **Figure 3.3.**

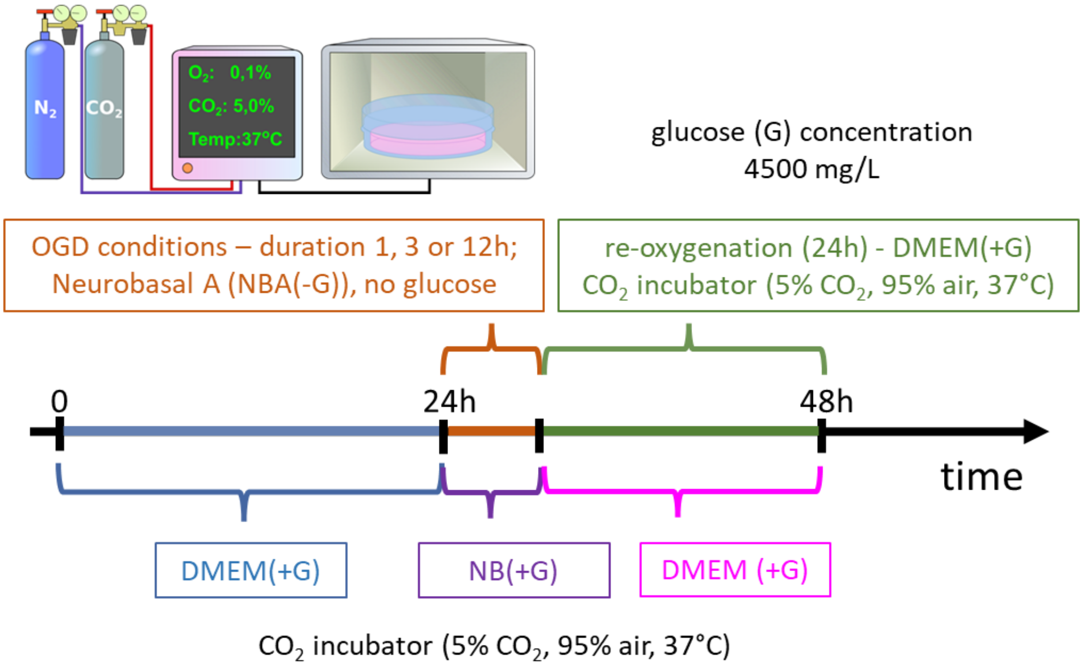

Figure 3.3. The time scale of the OGD experiment applied to SH-5YSY cells.

Experimental procedures (MTS, LDH, epi-fluorescence and confocal imaging, AFM, and cell-based ELISA) were performed directly after OGD exposure and following 24 h re-oxygenation.

3.2.2. Time scale for OGD for neurons

Mice primary hippocampal neurons were plated 7 days before experimental procedures on previously coated with poly-D-lysine plastic Petri dish, 12-well plate, or 24-well plate (TPP) and kept in the CO_2 incubator (37°C and 5%CO_2/95% air atmosphere) in Neurobasal+ medium containing 4500 mg/L glucose, 1 mM sodium pyruvate (ATCC, LGC Standards) supplemented with B27 and GlutaMax. Additionally, to prevent the overgrowth of remaining glial cells, the culture medium was supplemented with ARAC, exhibiting a cytostatic effect. After plating, the medium was replaced with neurobasal A medium (NBA, without glucose), and samples were placed in the able CO_2 incubator (Olympus) at 37°C. The atmosphere was kept at 5% CO_2, 0.1% O_2, and 94.9% N_2 maintained constant for 1h and 3h. Parallelly, control groups were rinsed with neurobasal medium containing glucose (NB) and in an atmosphere of 5% CO_2, 18% O_2, and 77% N_2. After OGD and parallel control conditioning, cells were exposed to 24 h re-oxygenation/conditioning in culture conditions in a neurobasal medium (NB) containing glucose. The time scale of the experiments is shown in **Figure 3.4.**

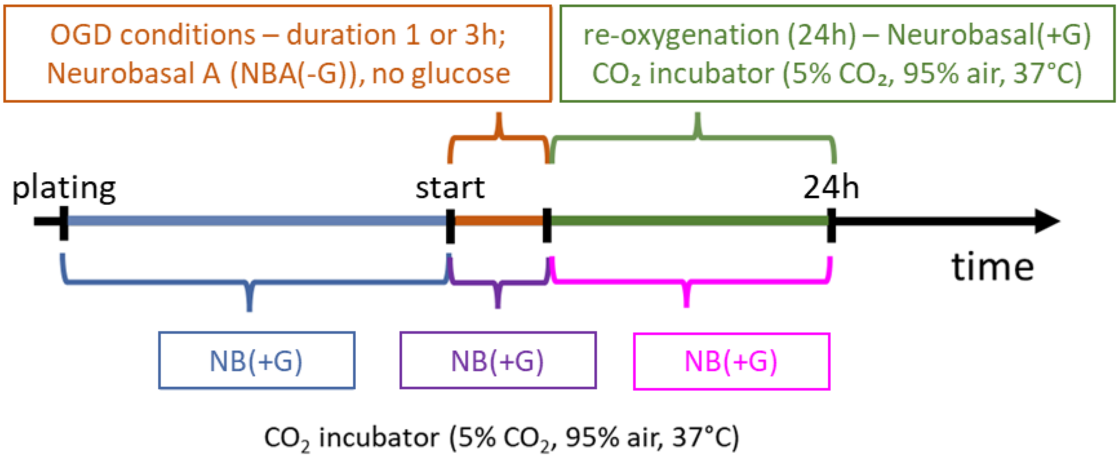

Figure 3.4. The time scale of the OGD experiment applied to neurons.

Experimental procedures (Live/Dead staining, epi-fluorescence and confocal imaging, AFM, and Western Blot analysis) were accomplished directly after OGD exposure and following 24 h re-oxygenation.

3.2.3. Cytochalasin D treatment of U118 MG and HeLa cells

After 2 days of plating, the culture medium was replaced with a medium containing 10 µM cytochalasin D. U118 MG and HeLa cells were maintained in the experimental medium for 10 and 30 minutes, respectively. After cytochalasin D treatment, the medium was replaced with a culture medium, and cell samples underwent AFM measurements and fixation for epifluorescence imaging of the actin cytoskeleton.

3.2.4. Preparation of cells for MTS assay

To describe changes in the metabolic activity of SH-5YSY cells MTS colorimetric test (Promega) was applied. Cells cultured in 24-well plates in 1 mL of DMEM at 50000 cells per 1 cm^2 were exposed to OGD. Afterwards, 100 µL of MTS reagent (tetrazolium compound) was added to the wells (final volume 1.1 mL), and samples were incubated at 37°C in 95% air/5% CO_2 atmosphere in the CO2 incubator (Nuaire) for 2 h. Then, 100 µL was aspirated and moved to the single well of the 96-well plate. The absorbance (OD = 490 nm) was recorded for 0h, 3h, and 24h after OGD using a spectrophotometer (ELISA SPECTROstar Nano, BMG LABTECH). The MTS assay was done in three biological repetitions.

3.2.5. Preparation of cells for LDH assay

The cytotoxic effect of OGD exposure was assessed using CyQUANT™ LDH Cytotoxicity Assay Kit (Invitrogen). Cells were cultured on 24-well plates in 1 mL of culture medium at a density of 50,000 per 1 cm^2. To investigate the effect of OGD exposure on cell survival, evaluation of LDH level was performed in the following samples: (i) control and OGD cells (collecting of media from wells), (ii) control and OGD cells treated with lysis buffer (10% by volume, 45 min in the CO2 incubator), (iii) culture medium (supernatant) taken from both, control or OGD 2d cultures and separately treated with lysis buffer in an analogous way as (ii) for verification of amount detached during the medium exchange cells. The first step of the LDH assay was to aspirate 50 µl of the medium from each sample type and transfer it into a 96-well plate. Next, by using the multichannel pipette, 50 µl of the reaction mixture was added to each well, and for 1h, samples were incubated, protecting against light exposure. Then, 50 µl of stop solution was added. In the next step, oxidation of reduced nicotinamide adenine dinucleotide (NADH) by diaphorase reduces a tetrazolium salt to a red formazan product and allows to read absorbance alterations. OD at 490nm was recorded using an ELISA reader (Ledetect 96 ELISA, LED-based microplate reader, Labexim Products).

3.2.6. Live/Dead staining

To evaluate how primary mice neurons survive OGD, cells were stained with calcein-AM for viable and propidium iodine (PI) for dead cells (Double Staining Kit, Sigma Aldrich). Prior to use, 10 µl of A and 5 µl of B solutions were dissolved in 5 mL phosphate-buffered saline (PBS, Sigma) to prepare the staining solution. Well, with cells culture in 12 well plates, was washed with PBS to remove residual esterase activity. Neurons at 50.000 cells per cm^2 were suspended in 0,5 mL of staining solution and incubated at 37 ºC for 15 min. Then, a fluorescence microscope with excitation at 490 nm viable cells and 545 nm dead cells were observed. An acetoxymethyl ester of calcein

(Calcein-AM) is a highly lipophilic and permeable cell membrane but is not fluorescent. Inside the living cell, the calcein is generated from Calcein-AM by esterase, showing fluorescence emission (excitation: 490 nm, emission: 515 nm). For PI, nuclei staining dye, viable cell membrane is unreachable. Compound intercalation with DNA double helix is possible only in case of lost permeability of cell membrane, which is correlated with cell death processes. Staining emits fluorescence (excitation: 535 nm, emission: 617 nm). Calcein-AM and PI can be excited with 490 nm, allowing simultaneous monitoring of viable and dead cells using a fluorescence microscope. With 545 nm excitation, only dead cells can be observed.

3.2.7. Phospho-Cofilin/Cofilin assay

Quantifying changes in cofilin activity via evaluation of phosphorylation level was performed using CytoGlow™ cofilin (phospho-Ser3) colorimetric cell-based ELISA kit (Assay Biotechnology). SH-SY5Y cells were plated 24h prior to OGD at 50000 cells per well on a 96-well plate. SH-SY5Y cells were maintained in OGD conditions for 1, 3, and 12h. After OGD, cells were fixed using 4% paraformaldehyde. Next, samples were washed three times with 200 µl with washing buffer (WB) for 5 minutes, each time with gentle shaking. Then, quenching was applied by rinsing samples for 20 minutes at room temperature (RT) with 100 µl of quenching solution. After 3 times washing with WB for 5 minutes at a time, 200 µl of blocking buffer was added for 1 hour at RT to block the nonspecific binding of antibodies. Afterward, the plate was rewashed (3 x times, WB at RT), and a solution of 50 µl of each primary antibody against phosphorylated cofilin (anti-cofilin (phospho-Ser3) antibody), cofilin (anti-cofilin antibody) and glyceraldehyde 3-phosphate dehydrogenase, GADPH (anti-GAPDH antibody) was added to the corresponding well and incubated for 16 hours (overnight) at 4°C. Afterward, samples were washed 3 times with 200 µl of WB for 5 minutes. In the next step, secondary antibodies in volume 50 µl (horseradish peroxidase (HRP)-conjugated anti-rabbit IgG antibody and/or HRP-conjugated anti-mouse IgG antibody) were added for 1.5h incubation at RT. After incubation, samples were washed, and each well was rinsed with 50 µl of Ready-to-Use Substrate for 30 minutes at RT, followed by a stop solution. OD was immediately recorded at 450 nm using a microplate reader (ELISA SPECTROstar Nano, BMG LABTECH).

3.2.8. Western blot analysis of phospho-cofilin and cofilin level

The western blot technique was applied to evaluate the expression level of cofilin and phospho-cofilin. Mice primary hippocampal neurons were plated on 36 mm plastic Petri dishes (TPP) previously coated with poly-D-lysine at 50000 cells per cm^2. After seven days of culture, an OGD was performed. Analogously to the rest of the studies of the neuronal cultures, four groups were examined, control without media change (C), control with media change on medium with glucose – Neurobasal (C-SH), and two OGD treated for 1h and 3h variants. After OGD conditioning, samples were washed with cold phosphate buffer saline PBS. Neuronal cultures were lysed in sample buffer (0.0625 M Tris/HCl pH 6.8, 2% SDS, 10% glycerol, 5% β-mercapto-ethanol) and using a spatula by scratching the surface of adherent culture, samples were collected to vials. Then samples were sonicated (300 V/T ultrasonic homogenizer) and boiled for 5 min at 95°C. The amount of protein was quantified using Qbit® Protein Assay Kit (Cat. Nos. Q33211, Q33212) (Invitrogen). Cell lysates containing equal, previously optimized amounts of protein (60 μg) were separated on 10% SDS-PAGE gels and transferred onto a PVDF membrane. Antibodies against cofilin and phospho-cofilin were used. The bands were visualized using horseradish peroxidase-coupled secondary anti-mouse or anti-rabbit antibody (Cell Signaling Technology). Total protein loading was determined by probing the membranes for GAPDH. Finally, immunoreactions were visualized by NBT/BCIP staining (Roche). Immunoblots were analyzed using the public domain ImageJ software (http://rsbweb.nih.gov/ij/). Densitometry results for a band were first divided by the corresponding amount of GAPDH content and normalized by the GAPDH content in neurons. The Western blot was repeated three times.

3.3. Experimental setup for inducing OGD

OGD experimental setup was based on a temperature table CO_2 incubator combined with a gas-flow controller (**Figure 3.5)**.

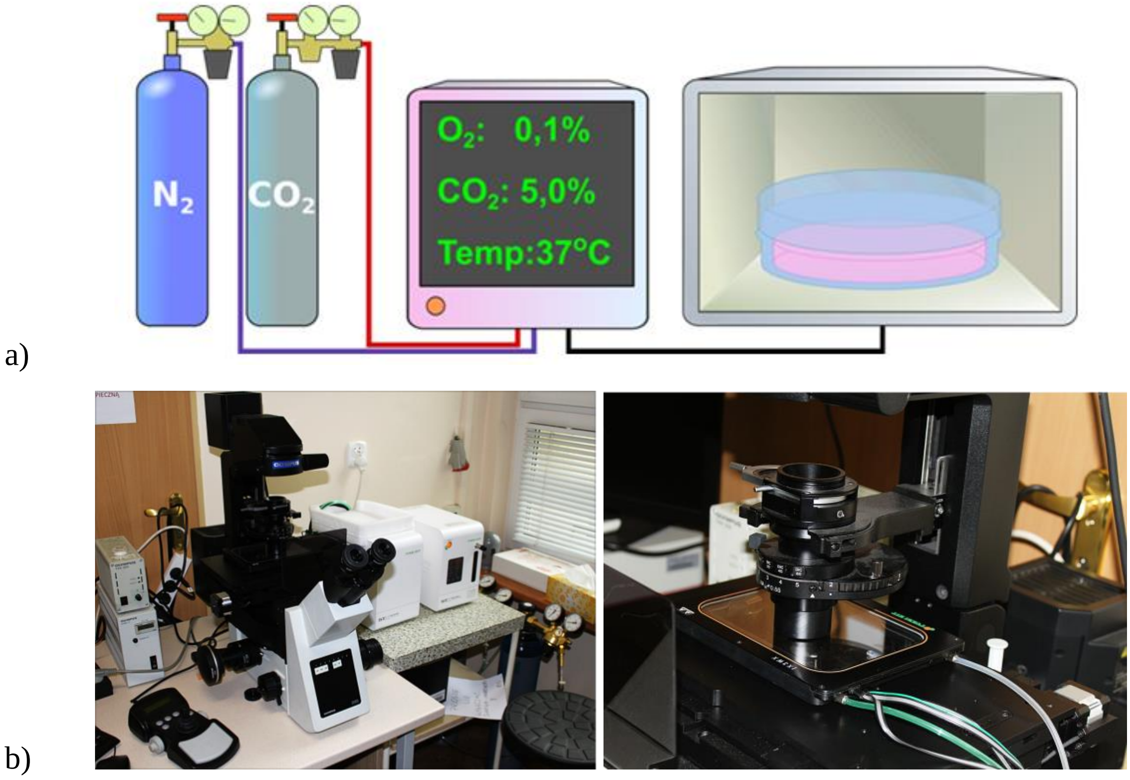

Figure 3.5. a) Scheme of the work and **b)** photos of the experimental device - table CO_2 incubator (Tokai Hit) mounted on the inverted optical microscope (Olympus IX83), combined with CO_2 and CO_2/O_2 controller, allows maintaining the temperature of 37°C.

In the system, gas bottles with CO_2 and N_2 are connected to the controller (Tokai Hit), regulating both the amount of air, CO_2, and N_2 fed into the table CO_2 incubator (Tokai Hit) and the temperature in the incubator (set to 37°C). The incubator is placed on a moving table (ProScan) settled on the inverted optical microscope (Olympus IX83). The atmosphere composed of 5% CO_2 and 0.1% O_2 was obtained by replacing air with a neutral gas, in this case – nitrogen (N_2).

3.4. MTS assay

The principle of MTS assay is based on the ability of metabolically active cells to reduce the MTS tetrazolium compound by NAD(P)H-dependent dehydrogenase enzymes. As a result, a colored formazan dye soluble in cell culture media is generated. Metabolic activity is obtained through absorbance readout at 490-500 nm.

3.5. LDH assay

The principle of LDH assay is based on the presence of lactate dehydrogenase (LDH) in the cytoplasm of various types of cells (**Figure 3.6.**).

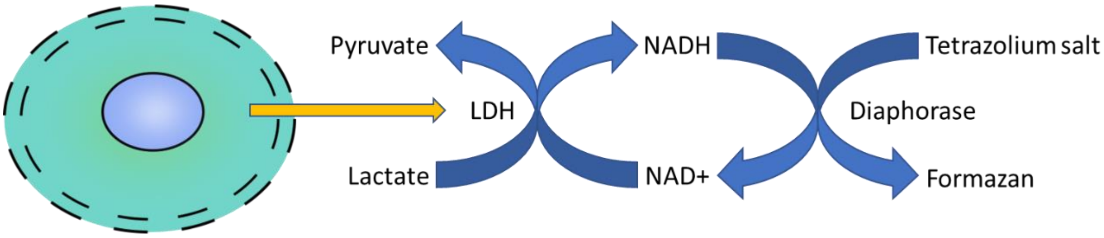

Figure 3.6. Principle of LDH assay.

Loss of cell membrane permeability is correlated with cell death. As a result, a release of LDH to the surrounding medium occurs. It can be quantified by using LDH as a catalytic enzyme converting lactate to pyruvate via NAD + reduction to NADH. The level of formazan is directly proportional to the level of LDH in the surrounding medium. To evaluate cell viability level, the following equation was used:

$$\%\,(cell\ viability) = 1 - \frac{experimental\ LDH\ release\ (OD_{490})}{maximal\ LDH\ release\ (OD_{490})} \tag{2}$$

where the maximum LDH release is the sum of LDH release in lysis buffer treated samples (cells and supernatants of control and OGD-treated cells, respectively).

3.6. Atomic force microscope (AFM)

The atomic force microscope (AFM) consists of three main elements, a probe with a tip mounted at the free end of the cantilever, an optical-based system used to detect cantilever deflection, and a piezoelectric system to scan and move **(Fig. 3.7.)**.

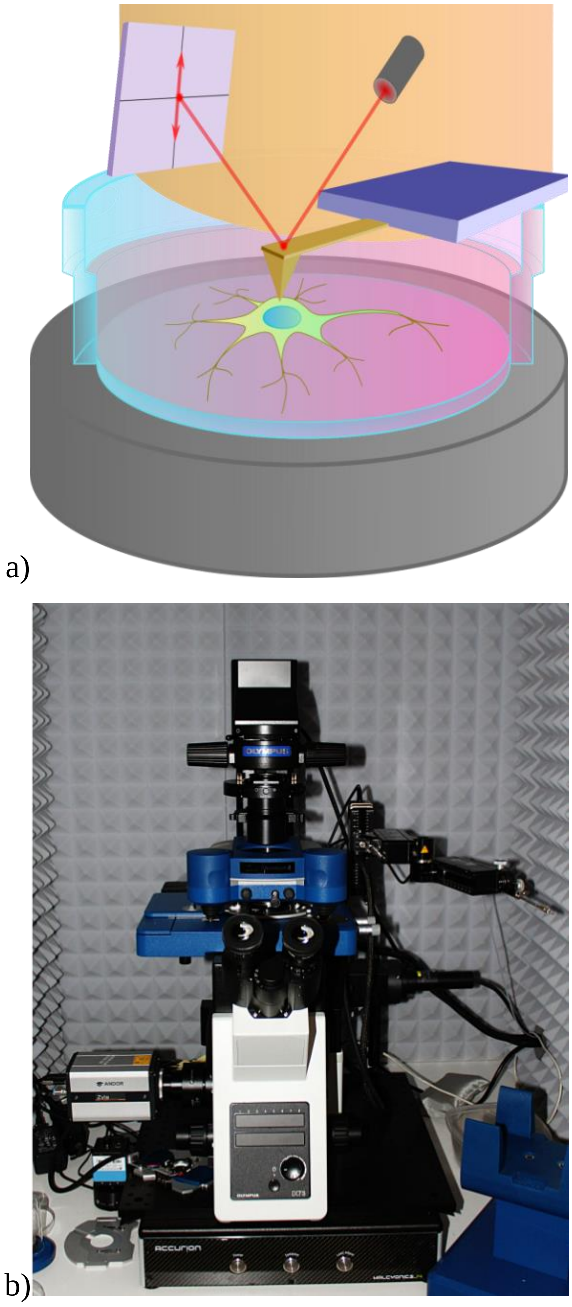

Figure 3.7. Scheme showing principle of AFM measurement **(a)**. Cells plated on plastic Petri dishes are placed under AFM. Piezo scanner is responsible for the movement of the sample, while the cantilever indents the cell. Detection of cantilever deflection is following. A laser beam is focused on the cantilever, and the reflected laser beam is recorded by the active area of the detector, divided into four quadrants measuring deflections in parallel and perpendicular directions. **(b)** Photo of JPK Atomic Force Microscope applied in measurements of OGD-induced changes in nanomechanical properties.

An optical system detects cantilever deflection by using a laser beam focused on the cantilever that reflects light into the active area of the position-sensitive detector. The active area of the photosensitive detector is divided into four quadrants, consequently allowing for measuring deflection in parallel and perpendicular directions. During the approach to the surface, the laser beam is focused in the middle. Consequently, signals from each quadrant are equal, and the difference between two upper (or two right) and two lower (two left) quadrants reaches zero. When the AFM probe reaches the sample surface, the cantilever deflects perpendicularly, and the shift between upper and lower pairs of quadrants in the voltage difference is observable.

Cantilever deflection is converted into force (F) by multiplying the recorded signal by two factors, namely, the cantilever spring constant and sensitivity of the photodetector, according to the following equation:

$$F\ [nN] = deflection[V] \cdot k \left[\frac{N}{m}\right] \cdot PSD \left[\frac{nN}{V}\right] \tag{3}$$

where k is the cantilever spring constant, and *PDS* denotes the photodetector sensitivity converting volts into nanometers. Scanning and sample movements are usually realized by piezoelectric elements operating based on the inverted piezoelectric effect.

The measurements were conducted using a commercial AFM equipped with a CellHesion head (Bruker-JPK Instruments). The microscope is equipped with a temperature control system set to 32°C to provide the cell survival conditions and the cantilever stability. The cell indentation was performed using silicon nitride cantilevers (ORC-8, Bruker). These cantilevers are characterized by a nominal spring constant of 0.03 N/m and an open half-angle of 36°. The spring constants of used cantilevers were determined using the Sader method [194]. On each cell was recorded a force map of 6 per 6 pixels (corresponding to a 6 μm × 6 μm scan size). The force curves were acquired at the approach/retract velocity of 8 μm/s. On every plastic Petri dish, calibration curves were acquired on a Petri dish bottom surface (a reference calibration curve allowing calibration of photosensitivity), and force curves were recorded on living cells – to examine changes in the biomechanical properties of conditioned groups. A grid of force maps was set over the nuclear region to minimize the influence of the underlying stiff plastic surface. In three separate biological repetitions, all measurements were conducted in DMEM at 32°C.

3.6.1. Young's modulus determination

In the AFM, the relation between the load force and the resulting indentation is derived by comparing two groups of force curves (i.e., dependencies between the cantilever deflection and relative sample or scanner position). The former are curves recorded on a stiff, non-deformable surface like glass or a Petri dish bottom surface, while the latter are curves recorded on living cells. The glass or Petri dish surface cannot be deformed within the range of forces applied by AFM, i.e., up to 10 nN. Subtracting curves recorded on the stiff surface from curves recorded on cells for a specific load force value enables us to obtain the indentation depth value (**Figure 3.8.**).

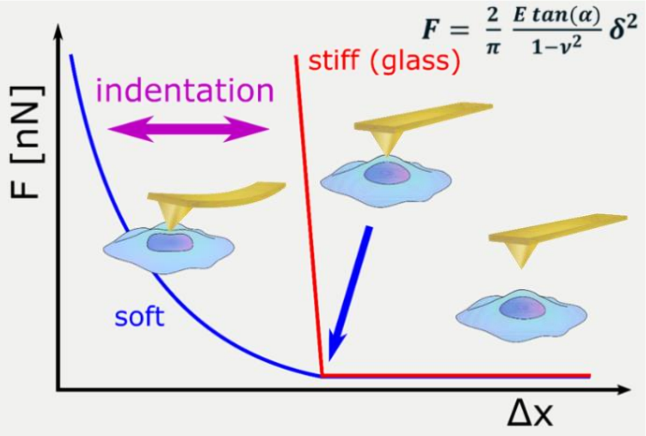

Figure 3.8. Scheme showing force (*F*) versus indentation (*Δx*) curve recorded on: stiff substrate (plastic or glass slide) – red; and soft substrate, e.g., cell – blue. The blue arrow indicates the contact point of the cantilever with the sample surface.

The Hertz-Sneddon contact mechanics analyzed the load force and indentations depth relation. The shape of the AFM probe can be approximated by a cone or paraboloid that resulted in the following relations between load force and indentation depth:

$$F(\delta) = \frac{2\cdot\tan(\alpha)\cdot E'}{\pi}\cdot\delta^2 \tag{4}$$

$$F(\delta) = \frac{4 \cdot \sqrt{R} \cdot E'}{3} \cdot \delta^{\frac{3}{2}} \tag{5}$$

where F is load force, δ is the indentation depth, α is the half-opening angle of the pyramidal indenter, R is the indenter radius. E' denotes reduced Young's modulus:

$$\frac{1}{E'} = \frac{1-\mu_{tip}^2}{E_{tip}} + \frac{1-\mu_{cell}^2}{E_{cell}} \tag{6}$$

$$E' \approx \frac{E_{cell}}{1-\mu_{cell}^2} \tag{7}$$

E_{tip} and E_{cell} are the apparent Young's modulus of the tip and the cell, respectively, and μ_{cell} is the Poisson's ratio (equaled to 0.5 assuming that cells are incompressible materials), μ_{tip} is Poisson's ratio of the tip, and its value is assumed as 0.28 ± 0.05. Young's modulus of the silicon nitride films reaches 222 ± 3 GPa, and [195]. It is much higher than the cell sample. Consequently, in equation (5), the term describing the mechanical properties of the probing tip is close to 0. Thus, it can be neglected in further calculations. Thus, equations (2) and (3) can be written in the form of:

$$F(\delta) = \frac{2 \cdot tan(\alpha) \cdot E_{cell}}{\pi \cdot (1-\mu_{cell}^2)} \cdot \delta^2 \tag{8}$$

$$F(\delta) = \frac{4 \cdot \sqrt{R} \cdot E_{cell}}{3 \cdot (1-\mu_{cell}^2)} \cdot \delta^{\frac{3}{2}} \tag{9}$$

One single cell is not enough to characterize the mechanical properties of cells; therefore, typically, a few thousand or a few hundred thousand curves are acquired. Tables 1-3 summarize the total number of curves recorded for neuroblastoma SH-5YSY cells and neurons at each condition.

Table 1. The number of force curves (the number of cells) recorded for U118 MG and HeLa cells.

Experimental conditions	**U118 MG**	**HeLa**
control	4356 curves (121 cells)	4356 curves (121 cells)
+cyto D	5004 curves (139 cells)	5076 curves (141 cells)

Table 2. The number of force curves (the number of cells) recorded for neuroblastoma SH-5YSY cells.

Experimental conditions	**0 h**	**RO 24 h**
control 1h	2160 curves (60 cells)	2160 curves (60 cells)
control 3h	2160 curves (60 cells)	2160 curves (60 cells)
control 12h	2160 curves (60 cells)	2160 curves (60 cells)
OGD 1h	2160 curves (60 cells)	2160 curves (60 cells)
OGD 3h	2160 curves (60 cells)	2160 curves (60 cells)
OGD 12h	2160 curves (60 cells)	2160 curves (60 cells)

Table 3. The number of force curves (the number of cells) recorded for neurons.

Experimental conditions	**control**	**OGD**
SO	1440 curves (40 cells)	**-**
1h	1620 curves (45 cells)	3276 curves (91 cells)
3h	3060 curves (85 cells)	3240 curves (90 cells)

Young's modulus changes that could occur during the elasticity measurements were monitored by plotting the modulus value calculated for a single cell as a function of time (**Figure 3.9**). The horizontal line denotes no time-dependent changes in mechanical properties of cells up to 2 hours, a time within which AFM measurements of the specific sample were conducted.

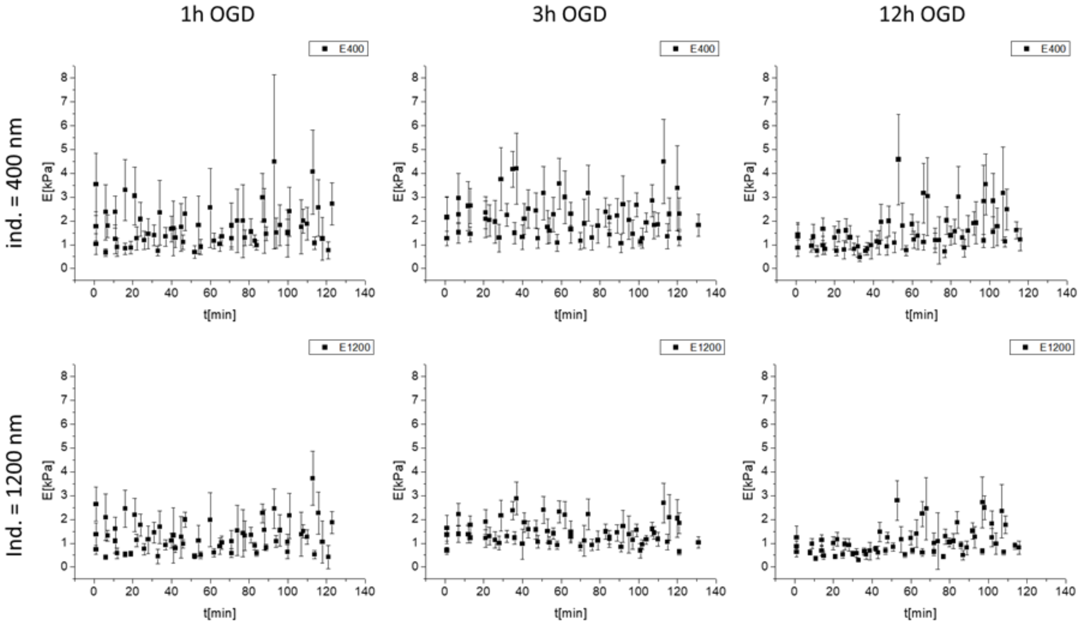

Figure 3.9. Young's modulus plotted a function of time, up to 2 hours (the time foreseen for AFM measurements).

Young's modulus distributions calculated for cells at two indentation depths are presented in **Figures 3.10** – **3.13.**

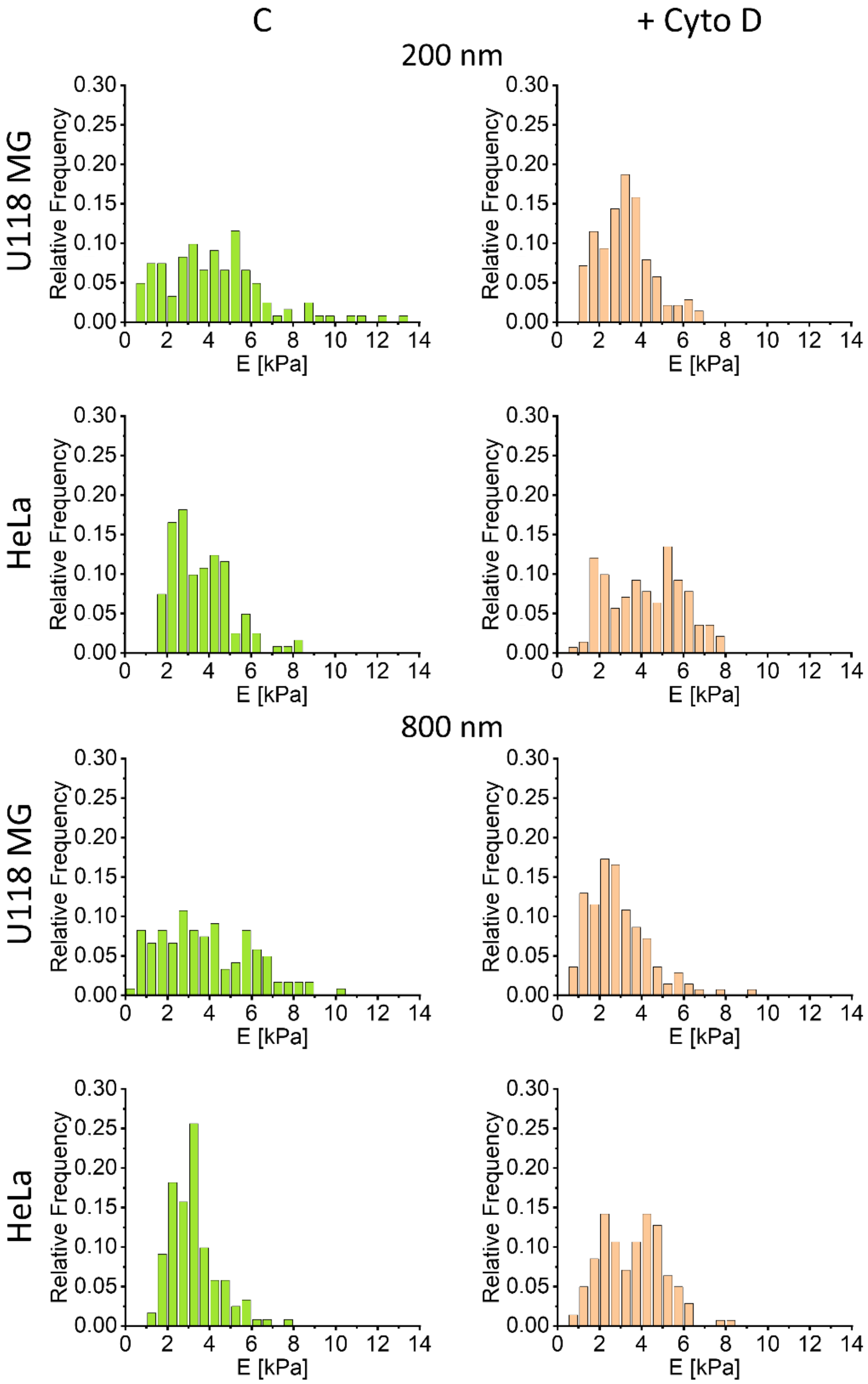

Figure 3.10. The histograms of Young's modulus obtained for control (C) and cyto D-treated U118 MG and HeLa cells, determined for indentation of 200 and 800 nm (each point in the histogram is a mean calculated for each cell separately).

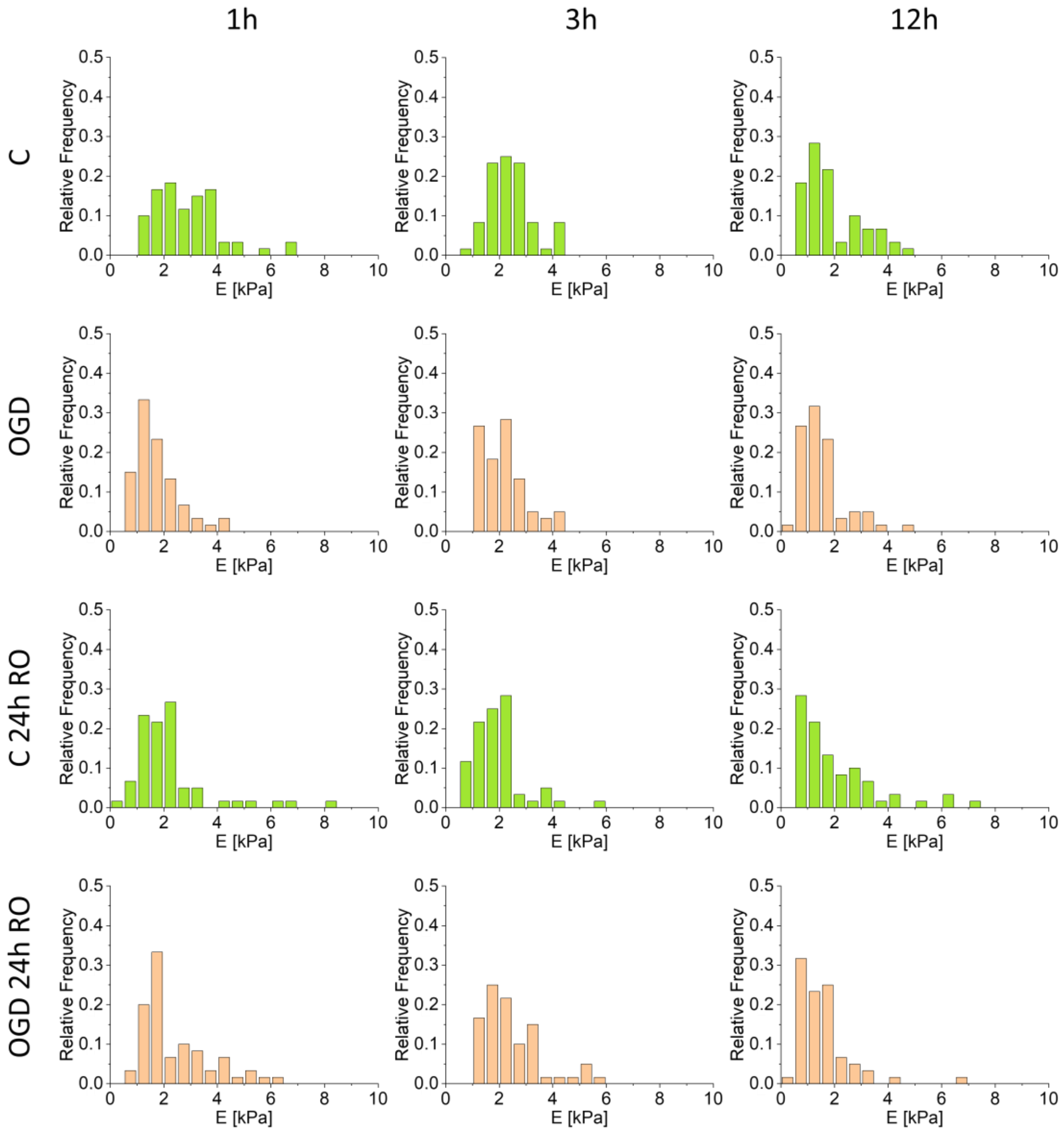

Figure 3.11. The histograms of Young's modulus calculated for C, OGD, and 24h RO treated SH-SY5Y cells, determined for indentation of 400 nm (each point in the histogram is a mean calculated for each cell separately).

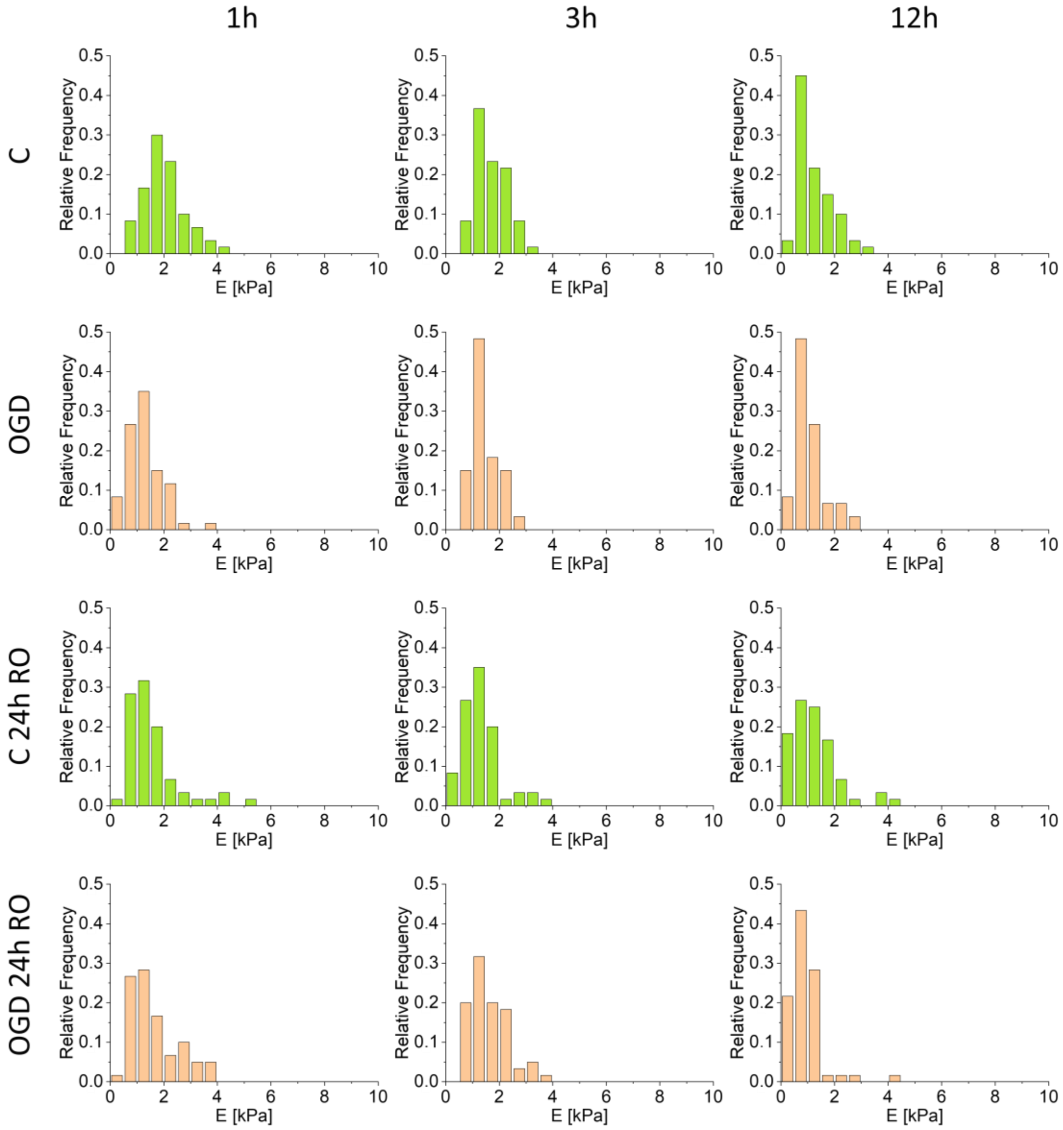

Figure 3.12. The histograms of Young's modulus calculated for C, OGD, and 24h RO treated SH-SY5Y cells, determined for indentation of 1200 nm (each point in the histogram is a mean calculated for each cell separately).

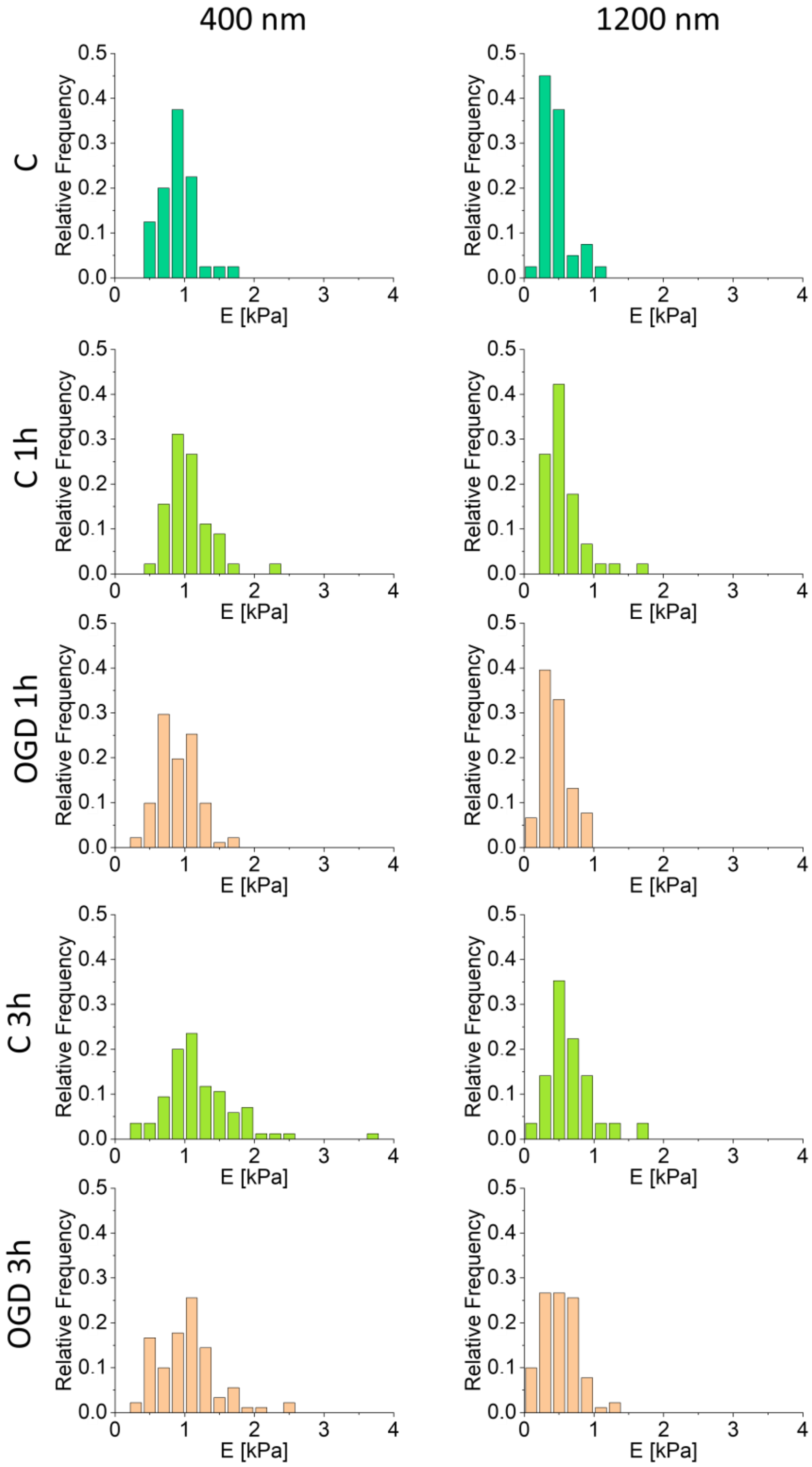

Figure 3.13. The histograms of Young's modulus calculated for C, C S-O (1h, 3h), and OGD-treated neurons determined for indentations of 400 and 1200 nm.

The final value of Young's modulus was determined as a mean and standard deviation from all measured cells to obtain fully independent results.

The nanomechanical properties of living cells change with increasing indentation depth due to the heterogeneity of the cell interior. Presence of various structures characterized by distinct mechanical properties placed in inhomogeneous order results in an irregular nanomechanical pattern of cells [196,197]. AFM probe interacts consecutively with glycocalyx, cell membrane, actin filaments, cytosol components, and cell nucleus. The dependent analysis enables us to study the heterogeneity of the cell interior, including cellular components lying in distinct indentation depths. (**Figure 3.14**).

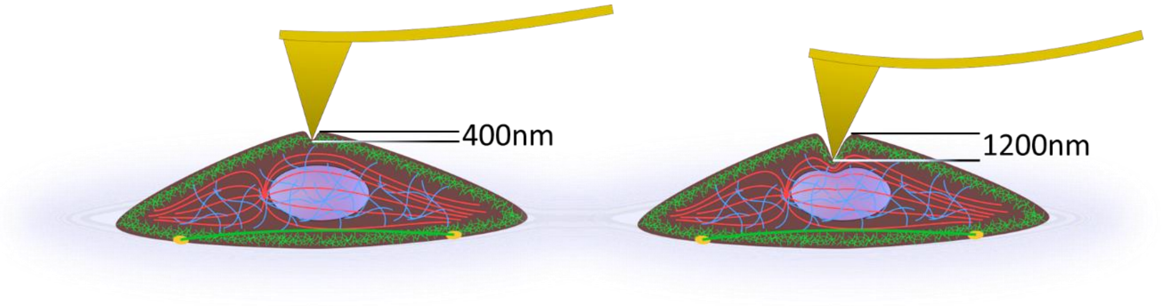

Figure 3.14. The indentation depth vs. heterogeneity of the cell interior structure.

Mechanical response up to 100 nm indentation depth originates from cell glycocalyx and cell membrane. The range of indentation between 200 nm – 400 nm corresponds with the actin cortex lying beneath the cell membrane. Evaluation of nanomechanical properties of cumulative response of the entire cell, including microtubules, intermediate filaments, cell nuclei, and also laying above actin cortex and cell membrane with glycocalyx can be obtained for analysis of indentations higher than 500 nm. For OGD experiments, two indentation depths were chosen, 400 nm and 1200 nm, to obtain a nanomechanical response from the actin cortex and for the nanomechanical response of the entire cell.

3.6.2. Quantitative imaging (QI)

The quantitative imaging (QI) mode allows for obtaining topography images and elasticity maps of single cells and groups of cells. The maps with sizes 50 µm × 50 µm and a resolution of 128 x 128 pixels were performed. Maximum force and speed were set to 4 nN and 30 μm/s, respectively. The Hertz-Sneddon estimation for the conical probe was applied in JPKSPM Data Processing software to obtain Young's moduli. Below, in **Figure 3.15.** are shown topography images of SH-SY5Y cells exposed to the OGD experiment.

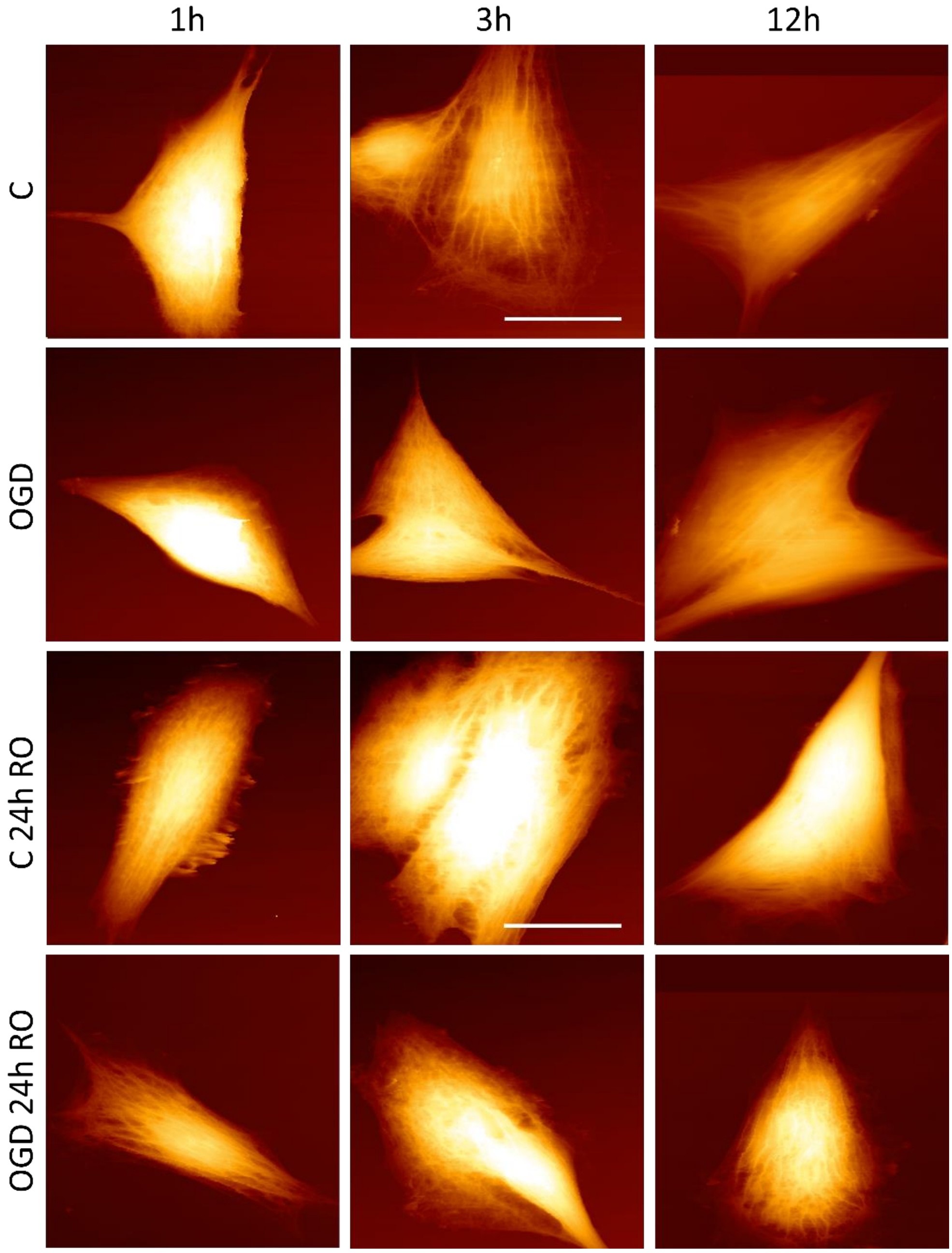

Figure 3.15. Quantitative images of SH-SY5Y cells after OGD and RO. Images were acquired at the *height (measured)* channel. Control cells (C, in NB(+G)), OGD cells (OGD 1h, 3h, or 12h, in NBA(-G)), reoxygenated OGD cells (RO 24h, in DMEM(+G)) QI mode, of control and OGD-treated SH-SY5Y cells.

3.6.3. Sample preparation for topography imaging

Mice primary hippocampal neuronal cultures cultured for 7 on 15mm round coverslips in 12 well-plate plates after the OGD experiment were fixed using 3.7% paraformaldehyde in PBS (phosphate-buffered saline, Sigma) for 20 minutes at 36°C. After 3 times rinsing them in PBS buffer, a salt removal procedure was applied. Cells were washed successively in a solution of 50% PBS (in deionized water), 25% PBS (in deionized water), and in deionized water for 2 minutes. As a crucial part of the protocol, sample dehydration was carried out. To ensure that all water molecules will be removed from the cellular samples, six dilutions of ethyl alcohol were prepared at concentrations of 40%, 50%, 60%, 70%, 80%, and 90%. Samples were rinsed in each solution for 30 seconds. After that, samples were dried for 20 min at Room Temperature (RT). The surface topography of mice primary hippocampal neurons was measured using atomic force microscopy working in contact mode (Xe120, Park Systems). The 15 mm glass coverslips with desalted and dried cells were mounted on the stage AFM piezoelectric scanner. Three sizes of scans were acquired, 90 µm x 90 µm, 50 µm x 50 µm, and 25 µm x 25 µm, at 256 x 256 pixels resolution.

3.6.4. Rheology of neurons based on AFM-measurements

Mechanical properties obtained from nanoindentation measurements can be applied to estimate only the elastic component. To extend the data analysis to cell viscoelasticity, AFM-based microrheological measurements are typically conducted according to the methodology proposed by Alcaraz et al. [166]. The sinusoidal oscillations are applied to the sample at certain indentation depths, followed by cantilever deflection recording as a function of the applied oscillation frequency (**Figure 3.16**).

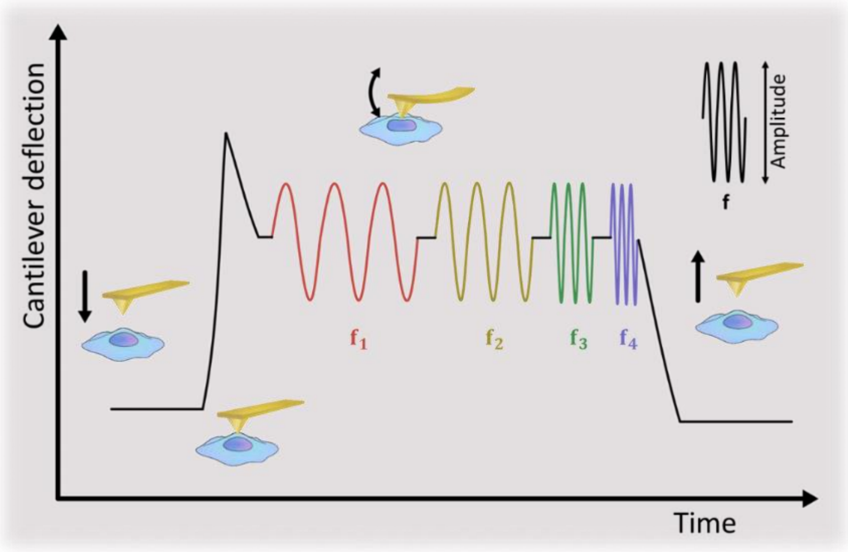

Figure 3.16. Illustration of the AFM-based microrheological measurements. Cantilever deflection is measured while applying sinusoidal oscillations at a constant amplitude to the sample. The oscillation amplitude is kept constant during the measurements. The oscillation frequency changes (here, f_1 to f_4).

The relation between the load force F and indentation depths δ for a probing tip possessing a shape of a four-sided pyramid is [166]:

$$F = \frac{3}{4} \cdot \frac{E}{1-\mu^2} \cdot \tan\theta \cdot \delta^2 \tag{10}$$

where E is Young's modulus, μ is the Poisson ratio approximated to 0.5 for biological samples, and θ is the half-opening angle of the pyramid (20°). Considering the experimental conditions, i.e., applying the small oscillations (with amplitude of 50 nm) at the indentation depths (< 1 μm), the equation (9) can be re-written as follows [165][166]:

$$dF = \frac{E \cdot \delta_0 \cdot \tan\theta}{2(1-\mu^2)} \cdot d\delta \tag{11}$$

After applying Fourier transform and a linearization for small amplitude oscillations according to Mahaffy and co-workers and transformation into the frequency regime to include energy dissipation, the following expression for the complex shear modulus:

$$G^*(\omega) = \frac{1-\mu}{3 \cdot \delta_0 \tan\theta} \cdot \frac{F^*(\omega)}{\delta^*(\omega)} \tag{12}$$

where $F^*(\omega)$ and $\delta^*(\omega)$ are Fourier transforms of measured force and indentation. The relation between the complex shear modulus and complex elastic modulus follows the Kirchoff equation:

$$G^* = \frac{E^*}{2 \cdot (1+\mu_{cell})} \tag{13}$$

Thus, the complex shear modulus $G^*(\omega)$ in the frequency domain can be written as:

$$G^*(\omega) = G'(\omega) + iG''(\omega) = \frac{1-\mu_{cell}}{3\delta_0 \tan\theta} \left\{ \frac{F^*(\omega)}{\delta^*(\omega)} \right\} \tag{14}$$

where ω is the angular frequency. The complex shear modulus contains the real part describing the elasticity called the storage shear modulus $G'(\omega)$, and the imaginary part related to dissipative (viscous-related) contribution called shear loss modulus $G''(\omega)$. Both storage and loss moduli are plotted as a function of oscillatory frequency (**Figure 3.17**).

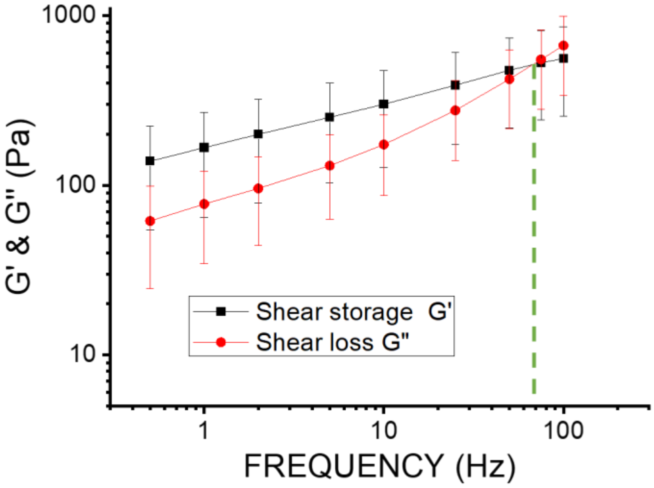

Figure 3.17. Example of storage *G'* and loss *G"* moduli plotted as a function of the oscillation frequency. The plot is in log scale, and the transition frequency, where the storage and loss moduli are equivalent, is indicated by a green dashed line.

Then, the frequency-dependent relations of storage and loss moduli are fitted with the power-law functions:

$$G'(\omega) = G_N^0 + k_1 \cdot \omega^a \tag{15}$$

$$G"(\omega) = k_0 + b \cdot k_1 \cdot \omega^a \tag{16}$$

The frequency at which $G'(\omega)$ equals $G"(\omega)$ allows for determining the so-called transition frequency used to differentiate between solid-like (elastic) and fluid-like (viscous) regimes of cell behavior. The transition frequency ω_T is:

$$\omega_T = \left(\frac{G_N^0 - k_0}{k_1 \cdot (b-1)}\right)^{\frac{1}{a}} \tag{17}$$

Another way used to estimate the viscous component of cells is called loss tangent (*tan(θ)*, where *θ8* is the phase lag between the applied oscillations and cantilever deflection) or loss factor, which is the ratio between *G"(ω)* and *G'(ω)*:

$$tan(\theta) = \frac{G"(\omega)}{G'(\omega)} \tag{18}$$

3.7. Fluorescence and phase-contrast microscopy

An optical microscope, working in fluorescent (confocal) and phase-contrast modes, was applied to evaluate changes in cell morphology during the OGD exposure. Phase-contrast images of SH-SY5Y cells under OGD and after 24h re-oxygenation conditions were collected using the inverted optical microscope (Olympus CKX53). Images were acquired using a color XC10 camera (Olympus). Fluorescent images of actin filaments, microtubules, and cell nuclei were acquired using either an epi-fluorescent or confocal microscope. Epi-fluorescence was conducted using an inverted optical microscope (Olympus IX83) equipped with a 100 W mercury lamp (illuminating the whole cell area uniformLy) and a set of filters to record emissions at 594 nm and 420 nm. Images were acquired using Orca Spark digital camera providing a 2.3 megapixel (1920x1200) pixel image and analyzed with ImageJ (ImageJ 1.53e https://imagej.nih.gov/ij/). The image acquisition was conducted in 3 separate biological repetitions, which resulted in 20 images per condition per repetition to be analyzed. Confocal images were recorded at the Laboratory of in vivo and in vitro Imaging (Maj Institute of Pharmacology Polish Academy of Science, Cracow, Poland) using Leica TCS SP8 WLL confocal microscope equipped with three new-generation detectors: HyD, PMT, and TLD. Fluorescent dyes were excited by diode laser (405 nm) and white laser with emission specter between 470 – 700 nm (HC PL Apo oil CS2 objective with 63x magnification was used). For fluorescent imaging, cells cultured on 24-well plates were fixed in 3.7% paraformaldehyde dissolved in phosphate-buffered saline (PBS, Sigma) for 5 min., then washed three times with PBS buffer. Permeabilization of the cell membrane was obtained by treating samples with a cold 0.2% Triton X-100 solution, then washed with the PBS buffer. Afterward, cells were incubated with β-tubulin antibody conjugated with Cy3 for 24 hours. The next day, samples were stained with phalloidin conjugated with AlexaFluor 488 dye during 1 h incubation. Cell nuclei were stained by 10 min incubation with Hoechst 33342 dye.

3.7.1. Determination of a single cell effective area

A single-cell effective surface area (*SA*), determined from fluorescent images, denotes the average surface area occupied by an individual cell (**Figure 3.18**).

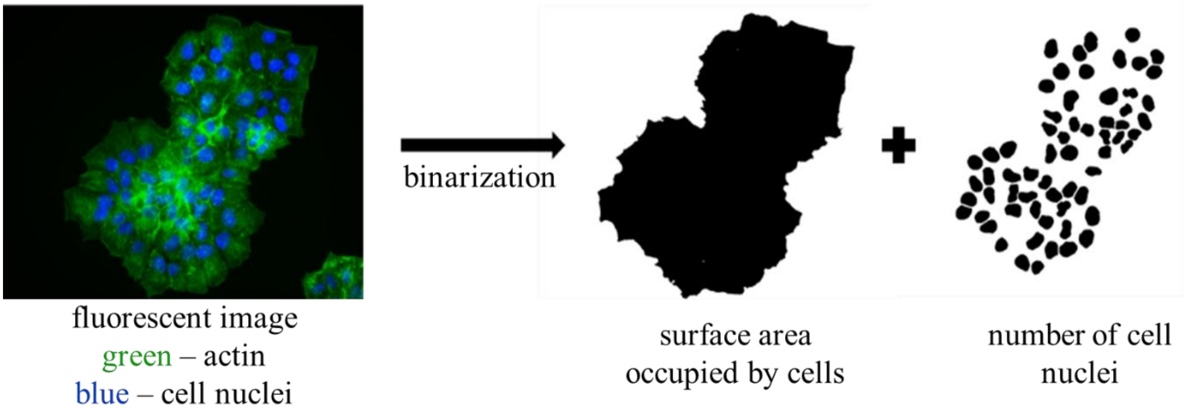

Figure 3.18. The idea of a single-cell effective surface area (SA) determination based on fluorescent images of HeLa cells.

Binarization of images (the method of converting multi-tone image into black – white image (two-tone image) by finding the threshold value of grayscale, allowing to create of mask covering object of interest – cell body or cell nucleus) collected from fluorescently stained F-actin and cell nuclei (by phalloidin-Alexa Fluor 488 dye, Hoechst 33342, respectively) was performed by ImageJ software. Then, the area occupied by cells in a single image (ROZMIAR OBRAZA in UM^2) was calculated. In parallel, in the same fluorescent image, the number of cell nuclei was counted to receive the number of cells per image. The effective surface area occupied by a single cell was determined by dividing the surface area occupied by cells by the corresponding number of cells. The total number of cells analyzed was at least 8000 cells.

3.7.2. Nucleus – to – cytoplasm (N/C ratio)

To estimate changes in organization and orientation in the space of cell nuclei, the ratio between the surface area occupied by the nucleus and cytoplasm (so-called nucleus-to-cytoplasm ratio, N/C ratio) was calculated. Here, the effective area of an individual cell nucleus was quantified analogously to the effective surface area of a single cell from binarized images of cell nuclei. Then, the effective surface area of a single nucleus was divided by the effective surface area of a single cell, and obtained ratios were compared between the control and experimental groups. The total number of images analyzed was 20 per condition in three separate biological repetitions.

3.8. Statistical analysis

Data were presented by applying box plots with mean ± standard deviation and 25% and 75% percentiles (box). Statistical significance was calculated by applying the following approach. First, normality and linearity tests were performed to qualify data to parametric or non-parametric hypothesis testing (Shapiro – Wilk, Anderson – Darling, Lilliefors, and Jarque –Bera). Characterization of distinct control and experimental groups revealed non-symmetric distribution. Application of non-parametric tests was obligatory, and statistical significance was verified by applying the non-parametric Mann-Whitney test (Origin 9.2 Pro). *P*-values indicate significance (ns – not statistically different, $p > 0.05$; $^*p < 0.05$, $^{**}p < 0.01$, $^{***}p < 0.001$).

4. Deformability of cells with different morphology

4.1. Objectives

The actin cytoskeleton is related to cell shape. Any changes in cell morphology intuitively denote the remodeling of the cell cytoskeleton. Some AFM studies showed the relation between the actin cytoskeleton and the mechanical properties of cells [198]. The objective of the study was to evaluate how cell morphology is related to mechanical properties. Therefore, glioblastoma U118 MG and cervix cancer HeLa cells were chosen for the study due to different morphology, i.e., fibroblast-like (U118 MG cells) and keratinocyte-like (HeLa cells). Cells were treated with cytochalasin D (cyto D), inhibiting the actin filament polymerization. AFM was applied to evaluate the nanomechanical properties, while cell morphology was observed on images of fluorescently stained actin filaments and cell nuclei.

4.2. Morphology of U118 MG and HeLa cells.

U118 MG and HeLa cells exhibit fibroblast-like and keratinocyte-like morphology, respectively (**Figure 4.1.**).

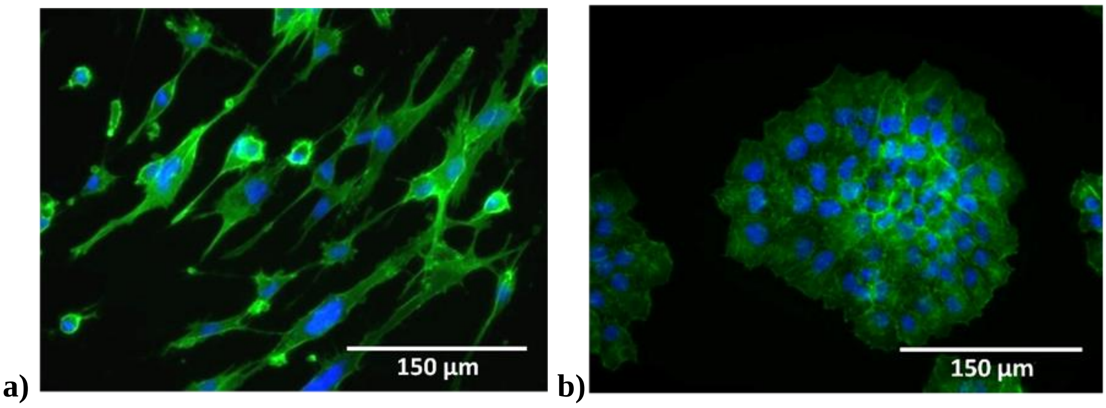

Figure 4.1. Morphology and organization of actin cytoskeleton of U118 MG (a) and HeLa (b) cells, observed under the epi-fluorescent microscope. Staining: actin filaments – phalloidin conjugated with Alexa Fluor 488 dye, cell nuclei – Hoechst 33342 dye.

U118 MG cells are growing separately, without overlapping on the area of surrounding cells, connecting with other cells with branched protrusions. The actin cytoskeleton displays short F-actin filaments (mesh-like structure) visible as a shadow in the epi-fluorescent images. Long, thin bundles of actin filaments spanning the whole cell body were barely observed. HeLa cells grow in clusters, with strong interaction with surrounding cells, but without forming the second layer and overlapping with other cells. The actin cytoskeleton shows a mesh-like structure with thick actin bundles spanning over the nuclear region of the cell. Both cell lines consist of populations of cells showing high discrepancies in the cell body and nucleus size.

4.3. Reorganization of actin cytoskeleton after cytochalasin D

AFM usage in studies of the nanomechanical properties of living cells assumes that they reflect the alterations in the organization of actin filaments due to a typical indentation range of 500 – 1000 nm. To verify this, experiments in which cells are treated with anticytoskeletal drugs are commonly conducted [199]. One of the most common compounds belongs to the cytochalasins family. They affect the organization of actin filaments by binding to a polymerized form of actin, i.e., F-actin, and preventing their polymerization [200]. As a result, the enhanced deformability of cells is typically observed after cytochalasin treatment, manifested as a decrease in Young's modulus [201,202]. However, in some cases, like for keratinocytes, the cytochalasin treatment does not lead to increased deformability of treated cells [171], which seems to depend on the organization of actin filaments inside the cells. Thus, to elaborate the relation between the actin cytoskeleton and deformability of cells, both chosen cell lines underwent the treatment with 10 μM cyto D, added to culture medium with cells for 10 and 30 min for U118 MG and HeLa cells, respectively (**Figure 4.2.**).

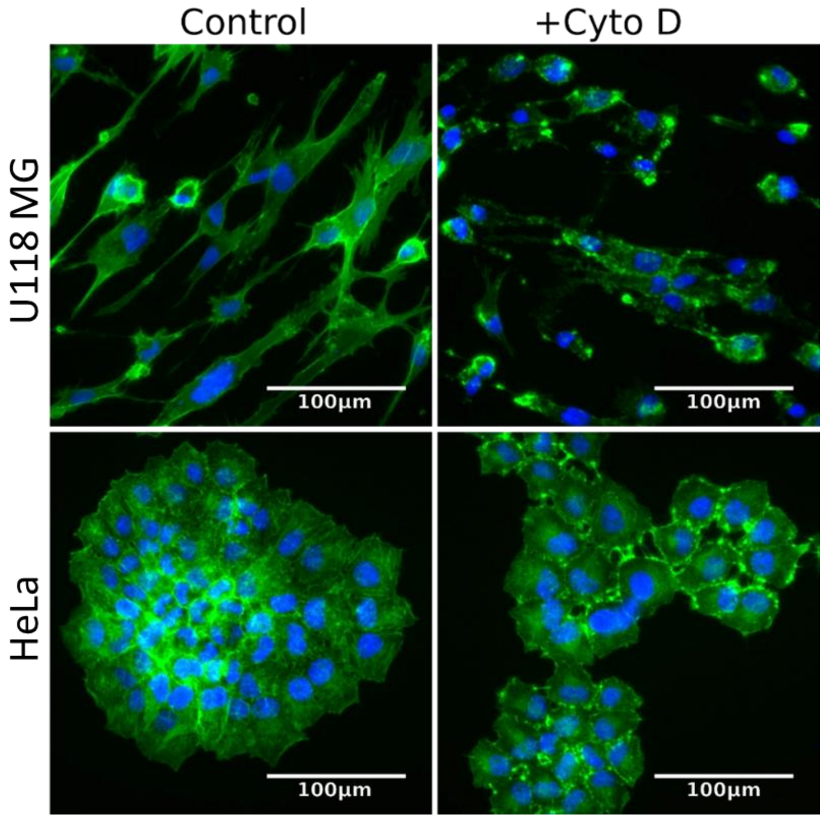

Figure 4.2. Epi-fluorescence images of cell morphology in control and cyto D treated U118 MG and HeLa cells. Staining: actin filaments – phalloidin conjugated with Alexa Fluor 488 dye, cell nuclei – Hoechst 33342 dye.

Cyto D induced changes in cell morphology in a cell-dependent manner. Aggregation of actin and loss of cell shape was observed in U118 MG cells, already after 10 min of incubation. The same concentration of cyto D added to HeLa cells required longer incubation time to observe the formation of gaps between cells in the cluster, which probably resulted in decreased cell-cell interactions. F-actin is concentrated in the border region of cells. The disintegration of the actin cytoskeleton was not observed in the central region of cells. To quantify effect of cyto D on cell morphology, the effective spreading area of a single cell was calculated (according to the procedure described in section **3.7.1.**). The results are presented in **Figure 4.3**.

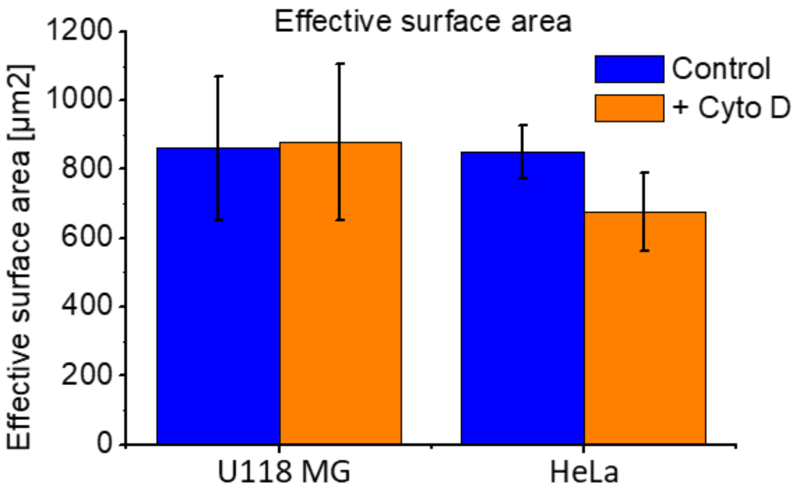

Figure 4.3. The effective spreading area of a single U118 MG and HeLa cell before and after cyto D treatment for 10 and 30 min, respectively. Data are expressed as mean with standard error.

The 10 µM cyto D did not induce changes in the spreading surface area of U118 MG cells. The corresponding values were 861.4 ± 209.7 µm^2 (*n* = 123 cells) and 877.9 ± 227.8 µm^2 (*n* = 183 cells) before and after treatment. For HeLa cells, the effect was more pronounced. The effective spreading surface area of a single cell dropped from 850.4 ± 77.3 µm^2 (*n* = 187 cells) to 677.1 ± 114.9 µm^2 (*n* = 268 cells). Notably, the drop was observed for the same cyto D concentration but for 3 times longer time.

4.4. Changes in cell mechanics after cytochalasin D

Evaluation of nanomechanical properties of U118 MG and HeLa cells was performed by AFM working in a classical force spectroscopy mode. The mechanical properties of control and cyto D treated cells were evaluated at the indentation depth of 200 nm and 800 nm. The former can be attributed to a direct response from the actin cytoskeleton, while the latter can be convoluted with the mechanical response from other cytoskeletal and cellular components lying deeper in the cell (**Figure 4.4).**

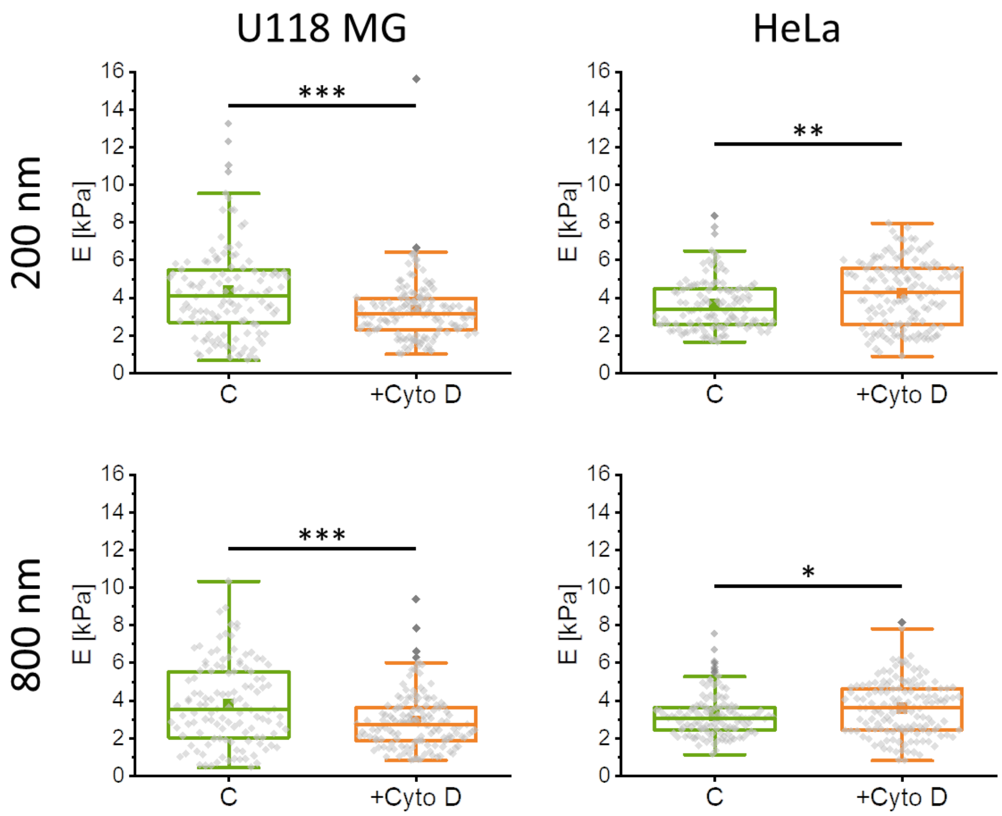

Figure 4.4. Young's modulus of U118 MG (a) and HeLa (b) cells before and after cytoD, determined for the indentations of 200 nm and 800 nm. Data are expressed as mean with standard error. Statistical significance determined: $p > 0.05$, $*p < 0.05$, $**p < 0.01$, $***p < 0.001$.

The results show a significant decrease in Young's modulus for U118 MG cells after applying 10 µM of cyto D for 10 min. A similar magnitude of changes was obtained for both indentation depths. Young's modulus calculated for the indentation of 200 nm decreased from 4.38 ± 2.69 kPa (n = 121 cells) to 3.32 ± 1.65 kPa (n = 139 cells). For larger indentation (800 nm), the analogous modulus drop was from 3.81 ± 2.17 kPa (n = 121 cells) to 2.88 ± 1.46 kPa (n = 139 cells). No change in the effective surface area of a single cell was observed for these cells (see **Figure 4.3**). For HeLa cells, prolonged (30 min) exposure to 10 µM cyto D caused opposite changes in cell mechanics, regardless of the indentation depth chosen for the analysis. Thereby, the significant increase of Young's modulus was reported to be from 3.66 ± 1.42 kPa (n = 121 cells) to

4.22 ± 1.74 kPa (n = 141 cells) and from 3.21 ± 1.16 kPa (n = 121 cells) to 3.59 ± 1.45 kPa (n = 141 cells) for the indentations of 200 nm and 800 nm, respectively.

Following the work of Pogoda et al. [196], a so-called R factor was determined. Here, it is defined as a ratio between Young's moduli determined at 200 nm and 800 nm indentation depths (**Figure 4.5)**. Its value describes the in-depth mechanical homogeneity of the studied sample (its variability quantified by standard deviation) and the direction of changes, i.e., softening ($R < 1$) or stiffening ($R > 1$). The latter estimates the contribution from other than actin cytoskeleton components.

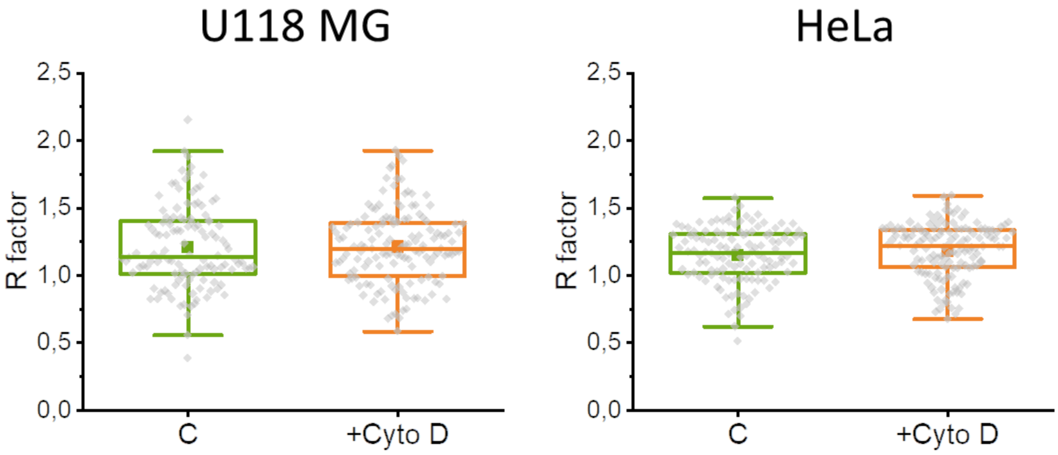

Figure 4.5. R factor, defined as a ratio between Young's modulus determined at 200 nm and 800 nm, for U118 MG (a) and HeLa (b) cells before and after cytochalasin D treatment. Data are expressed as mean with standard error. Statistically significant changes were not observed.

The obtained R factor for both studied cell lines was close to zero. For U118 MG cells, it was 1.21 ± 0.31 (n = 121 cells), and 1.21 ± 0.28 (n = 139 cells) for control and cyto D treated cells, respectively. The corresponding R factors for HeLa cells showed similar values of 1.15 ± 0.20 (n = 121 cells) and 1.18 ± 0.20 (n = 141 cells). These R factors highlight slight stiffening of the cells at 800 nm indentation depths at 15 – 21%. Such results indicate that the cell nucleus considered a stiff part of the cell, convolutes with the mechanical response originating from the actin cytoskeleton. However, regardless of the organization of actin filaments and cyto D exposure, this contribution is similar for both cell lines, which states that the mechanical response detected by AFM is mostly linked with actin filaments. The standard deviation at the level of 17% to 26% delivers the information that the mechanical properties of the studied cell populations are relatively homogenous, i.e., they did not change much from one cell to another.

4.5. Summary

A study of nanomechanical properties of cells characterized by different morphology and organization of actin cytoskeleton resulted in the following findings:

- Both cells types were characterized by similar deformability (Young's modulus of 3 – 4 kPa)
- cyto D effect was cell-type dependent and showed an inverse relation between Young's modulus and the effective surface area of a single cell (a drop in Young's modulus was not correlated with changes in the surface area values, and changes in the latter were not manifested in the alterations of cell mechanics).
- Both studied cell populations were mechanically homogenous, and the mechanical response originated mainly from the actin cytoskeleton.

These findings suggest that, despite morphological changes, the mechanical response of ODG-treated cells can be attributed to the remodeling of actin filaments.

5. 5. Nanomechanical properties of neuroblastoma SH-SY5Y cells after OGD

5.1. Objectives

Mechanisms governing alterations in nanomechanical properties and their relations to the molecular processes are essential for understanding the function and pathology of the brain [203]. The use of immortalized and easy-in-culture cellular models facilitates collecting high throughput data. Compared to the primary cell culture models, their application is independent of quality and purity of isolation, reducing factors affecting the reproducibility of results. Therefore, to elaborate AFM-related experimental conditions and properly interpret the obtained results, the human neuroblastoma SH-SY5Y cells were used. To obtain a complete image of how OGD exposure (5% CO_2, 0.1% O_2, lack of glucose and sodium pyruvate) changes the mechanochemical properties of cells, the AFM measurements were accompanied by such experiments as the determination of cell viability, metabolic activity, and imaging of cell cytoskeleton were conducted. The working hypothesis assumed that the cofilin/phosphocofilin balance guides the reorganization of the actin cytoskeleton; thus, the expression level of these cofilin forms was estimated. The results presented here have already been published in Zielinski et al. *Scientific Reports* **12** (2022) 16276.

5.2. The nanomechanical properties of OGD-treated SH-SY5Y cells

The elasticity measurements were conducted using AFM working in a force spectroscopy mode. Young's (elastic) modulus, a measure of cell mechanics, was calculated by applying Hertz-Sneddon contact mechanics, assuming that the shape of the probing tip can be approximated as a cone [204,205]. Details are presented in section **3.6.1.** The mechanical properties of OGD-treated cells were determined for two indentation depths of 400 nm and 1200 nm. The former reflects mainly the mechanics of the actin cortex, while the latter may indicate the contribution from structures lying in deeper parts of the cells, such as microtubules and cell nuclei. It should be noted here that AFM measurements are limited to only adherent cells. Thus, examined changes refer to cells surviving OGD (cells detached from the surface after OGD are inaccessible for AFM measurements). The applied experimental conditions are summarized in section **3.6.** It has been demonstrated that the mechanical properties of cells spread on the stiff substrate are not uniformly distributed [206]. Therefore, images showing the distribution of Young's modulus over the whole cells were acquired using the QI mode (as described in section **3.6.2.**). The elasticity maps for control and OGD-treated cells are presented in **Figure 5.1**.

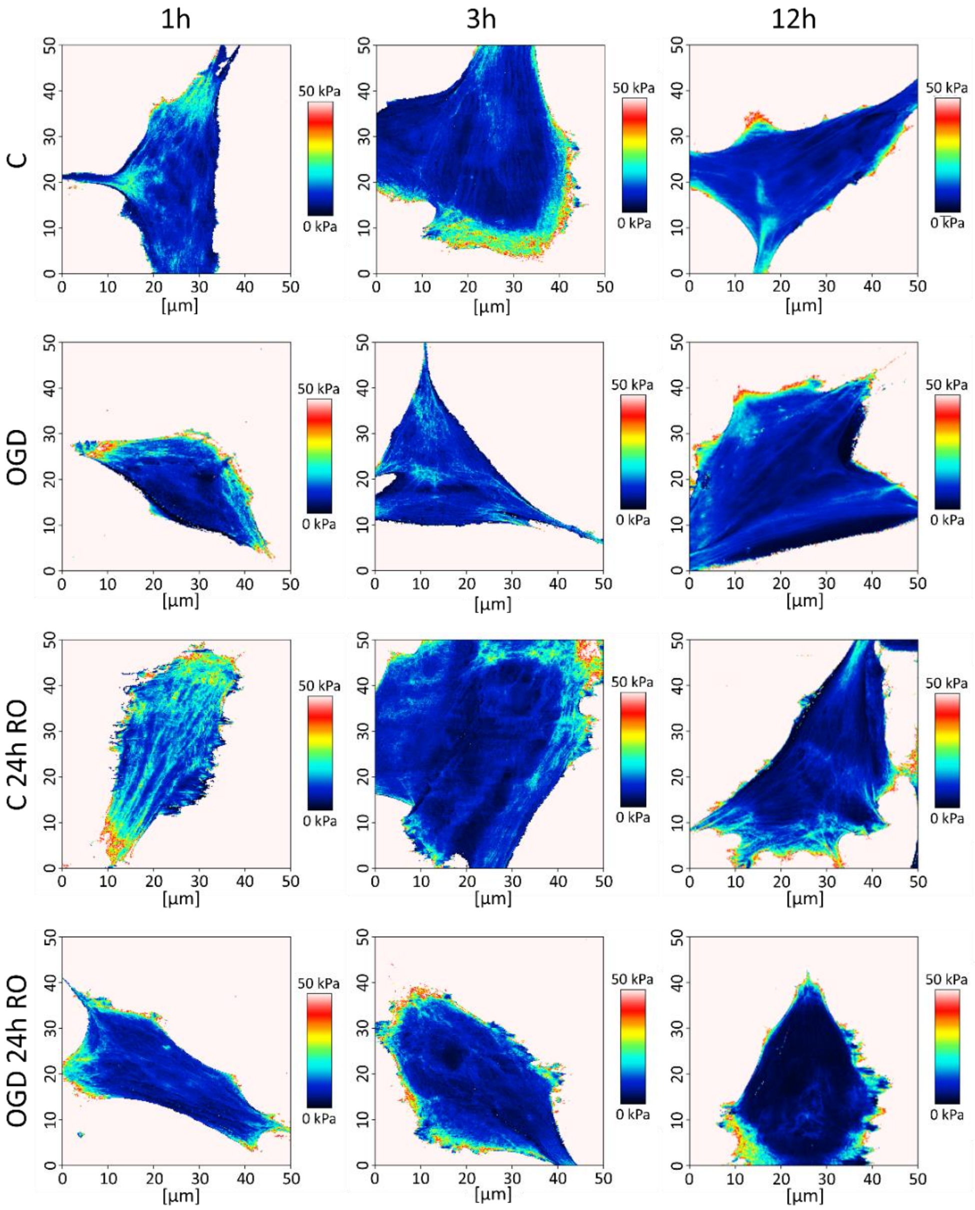

Figure 5.1. Elasticity maps, recorded using SH-SY5Y cells after OGD and RO. Control cells (C, in NB(+G)), OGD cells (OGD 1h, 3h, or 12h, in NBA(-G)), reoxygenated OGD cells (RO 24h, in DMEM(+G)) QI mode, of control and OGD-treated SH-SY5Y cells.

The results showed heterogeneity of Young's modulus distributions, regardless of the experimental conditions. A larger Young's modulus is observed at the cell edges, which probably results from the effect of stiff substrate (here, Petri dish surface) on the mechanics of cells. Such an effect dominates at the peripheral parts where the cell height is smaller. Importantly, a small modulus variability was observed within the cell nuclear region. Thus, the final Young's modulus of cells exposed to OGD for 1h, 3h, and 12h, followed by 24h re-oxygenation, was determined from the data collected above the cell nucleus (**Figure 5.2**).

For smaller indentation depths (400 nm), the direct comparison of OGD-treated and non-treated cells (n = 60 measured cells for all conditions) shows a decrease of Young's modulus of about 39.2% (1 h OGD; $p < 0.001$), 10.7% (3h OGD; $p = 0.045$), and 19.4% (12h OGD; $p = 0.042$), measured directly after OGD exposure. The lower Young's modulus denotes larger deformability of the OGD-treated cells. Cells measured after 24h culture in re-oxygenation conditions (DMEM + (G)) display restoration of Young’s moduli to values obtained for control cells: for 1h OGD-treated cells after 24h RO, Young's modulus were 2.40 ± 1.31 kPa and 2.22 ± 1.46 kPa ($p = 0.401$), for 3h OGD-treated cells after 24h RO, the moduli were 2.46 ± 1.09 kPa and 2.12 ± 1.03 kPa ($p = 0.084$)), and for 12h OGD-treated cells after 24h RO moduli were 1.55 ± 0.98 kPa and 1.05 ± 1.48 kPa ($p = 0.110$)), for OGD-treated and control cells, respectively. Having in mind that at 400 nm indentation depts, the mechanical response of cells can be attributed to the remodeling of actin filaments, these results show that such restoration is independent of the OGD duration and can be connected with the activation of some cytoskeletal compensatory mechanisms.

Insight into alterations of the combined contribution of actin and deeper parts of the cell (microtubules, cell nuclei) can be provided by analyzing deeper indentation (here, 1200 nm). Obtained results showed the deformability increase in cells measured directly after 1h and 3h OGD. Young’s modulus of measured cells decreased by 35.5% ($p > 0.001$) and 16.8% ($p = 0.007$) as compared to control non-OGD-treated cells, respectively. No changes in mechanical properties were noted for cells measured directly after 12h of the OGD exposure ($p = 0.188$). The comparison of the deformability of cells measured directly after OGD and after 24 of RO shows statistically insignificant changes, indicating that the mechanical contributions from the deeper cellular layers are not present.

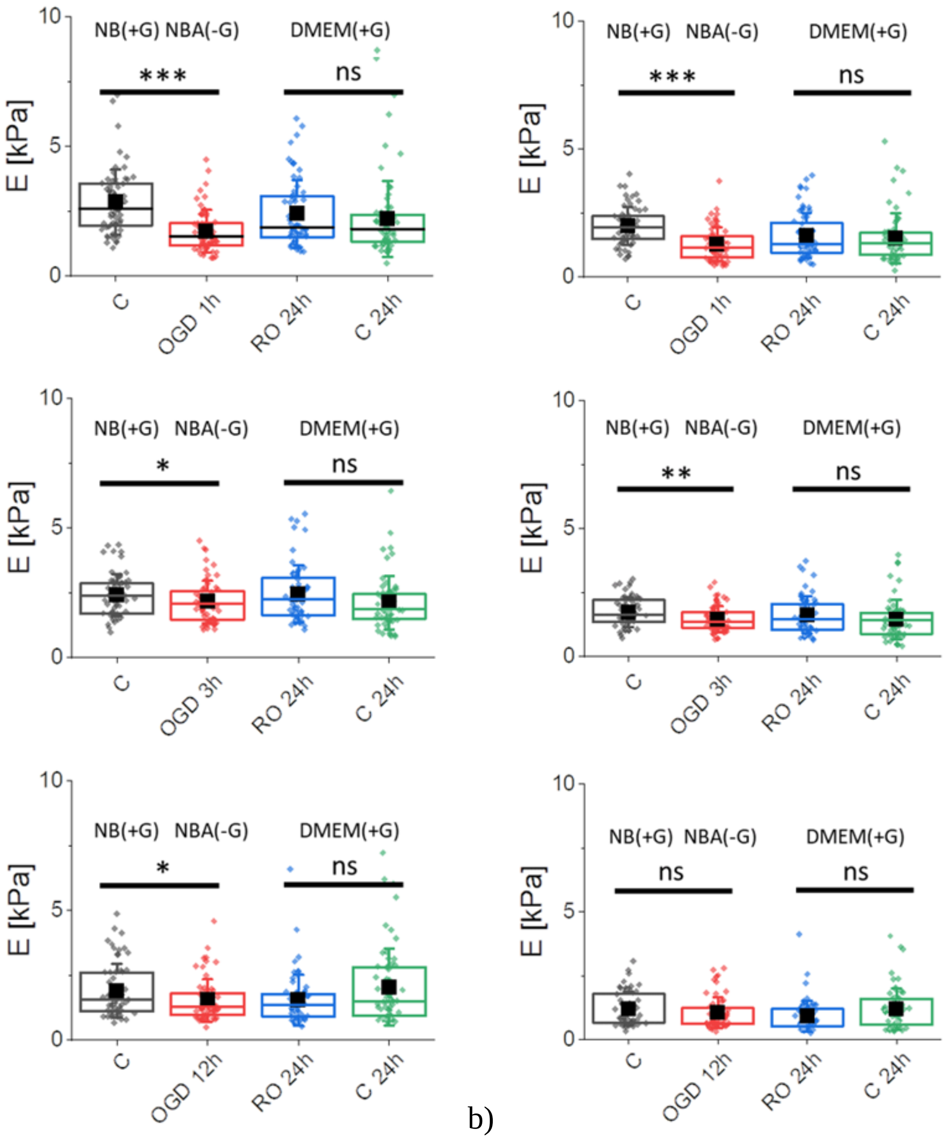

a) b)

Figure 5.2. Young's modulus of neuroblastoma SH-SY5Y cells exposed to OGD, determined for the indentation depths of 400 nm (a) and 1200 nm (b). Box plots show a median (line); a mean (solid square); standard deviation (box); 25% and 75% percentiles (box); n = 60 cells (notation: C – control cells in NB(+G)), OGD cells (OGD 1h, 3h, or 12h, NBA(-G)), reoxygenated OGD cells (RO 24h, DMEM(+G)), and control, non-OGD cells (C 24h) cultured in the same conditions as reoxygenated OGD cells), Statistical significance: *ns* – not significant ($p > 0.05$), *$p < 0.05$, **$p < 0.01$, ***$p < 0.001$ (reprinted from Zielinski et al. *Scientific Reports* **12** (2022) 16276 under CC-BY 4.0 license).

Finally, by comparing Young's moduli calculated for smaller (400 nm) and larger (1200 nm) indentation depths, it is possible to state that mechanical contribution from the deeper lying organelles, such as microtubules or cell nucleus, on biomechanical properties of OGD-treated cells is weakly present. This together with the results of cell deformability after re-oxygenation of OGD-treated cells, show that nanomechanical properties of SH-SY5Y cells largely respond to the organization of the actin cytoskeleton.

5.3. Viability of OGD-treated SH-SY5Y cells

To investigate the effect of OGD exposure on the survival of SH-SY5Y cells and its relation to mechanical properties of these cells, cell viability (LDH assay determining lactate dehydrogenase release to culture media indicating membrane damage [207]), and metabolic activity (MTS assay determining the level of the reduced tetrazolium related to impaired NAD(P)H metabolism [208]) were assessed. Samples were collected directly after OGD and after 24h of re-oxygenation. The results revealed that cell viability and metabolism depend on the OGD duration (**Figure 5.3)**. Additionally, a reduction of metabolic activity was present in cell cultures following the 24-hour re-oxygenation period.

The membrane integrity is directly linked with cell viability [207]; thus, LDH assay relates lactase dehydrogenase to the number of viable cells. After OGD exposure, cell viability dropped from 13% to 17% (**Figure 5.3a**). A similar decrease in cell viability was observed for cells measured after 24h RO, i.e. (12%-15; **Figure 5.3b**). The results of the MTS assay could be related to cell metabolism because cells reduce tetrazolium to soluble in medium formazan. Large absorbance values correspond to the high metabolism of cells, while lower absorbance correlates with a decrease in the metabolic activity of cells. For prolonged OGD exposures (i.e., 3h and 12h, **Figure 5.3c**), the level of metabolic activity of cells significantly decreased by 7.1% ($p < 0.001$) and 41.5% ($p < 0.001$), respectively. In the case of 1h-exposure (**Figure 5.3c)**, the metabolic activity of OGD-treated cells was similar to control non-OGD-treated cells ($p = 0.262$). After 24h re-oxygenation, a significant drop of absorbance was observed for all three groups of cells subjected to OGD (**Figure 5.3d)**.

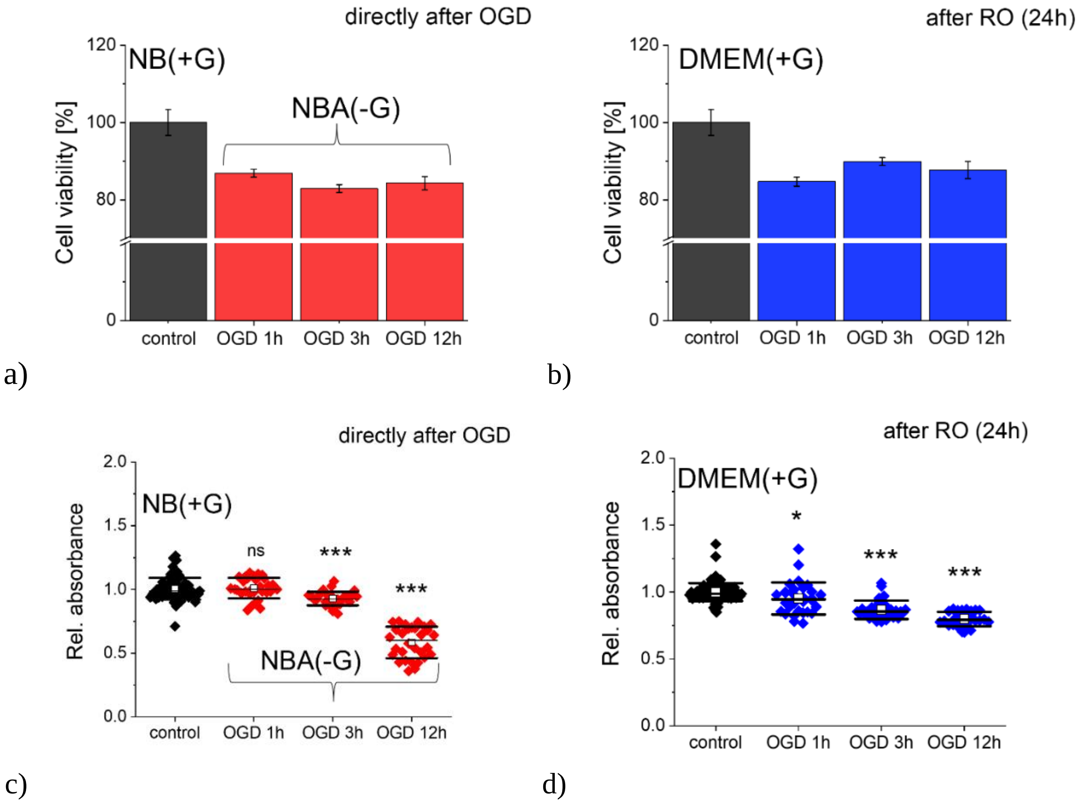

Figure 5.3. Viability and metabolic activity of SH-SY5Y neuroblastoma cells after OGD exposure and following 24h RO. (a, b) LDH results are represented by the mean value calculated from 12 ELISA readouts after normalization of relative absorbance to values obtained for the control samples. (c, d) MTS results show a distribution of single dots (one dot refers to one readout from the ELISA reader). A mean (open square), median (middle black line), and standard deviation (black line above and below a middle one) were determined from data gathered in 3 independent repetitions. Statistical significance: $p > 0.05$, $*p < 0.05$, $***p < 0.001$, *ns* – not statistically significant (reprinted from Zielinski et al. *Scientific Reports* **12** (2022) 16276 CC-BY 4.0 license).

The obtained finding suggests no correlation between metabolic activity and cell viability in applied experimental conditions.

5.4. Morphology and cytoskeleton of OGD-treated SH-SY5Y cells

Before AFM measurements and fluorescence microscopy examination, phase-contrast imaging was applied to investigate potential changes in cell morphology during OGD exposure (**Figure 5.4**).

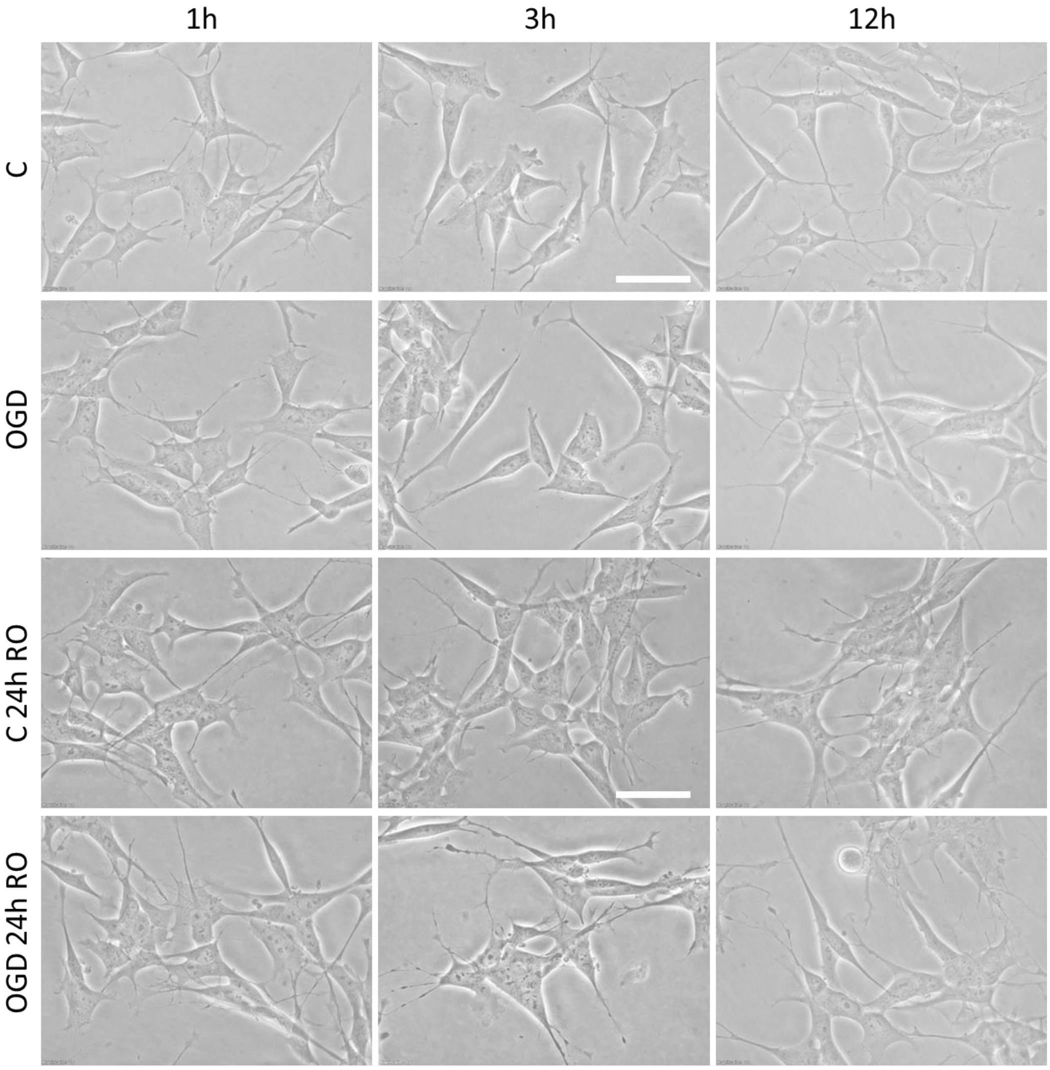

Figure 5.4. Phase-contrast images of SH-SY5Y cells after OGD and RO. Control cells (C, in NB(+G)), OGD cells (OGD 1h, 3h, or 12h, in NBA(-G)), reoxygenated OGD cells (RO 24h, in DMEM(+G)), and control, non-OGD cells (C 24h, in DMEM(+G)). Scale bar 50 μm (reprinted from Zielinski et al. *Scientific Reports* **12** (2022) 16276 under CC-BY 4.0 license).

A rough analysis of obtained images does not reveal any particular changes in cell morphology adhesion and organization of cell clusters. OGD-treated cells display similar spindle and neuron-like morphology as control, and non-treated cells, regardless of the OGD and RO duration. Changes in cell mechanics are often correlated with alterations in the organization of crucial components of the cytoskeleton: actin filaments and microtubules. Therefore, confocal images with fluorescently labeled F-actin, β-tubulin, and cell nucleus were collected for SH-SY5Y cells immediately after OGD exposure (**Figure 5.5**) and followed 24h re-oxygenation (**Figure 5.6**).

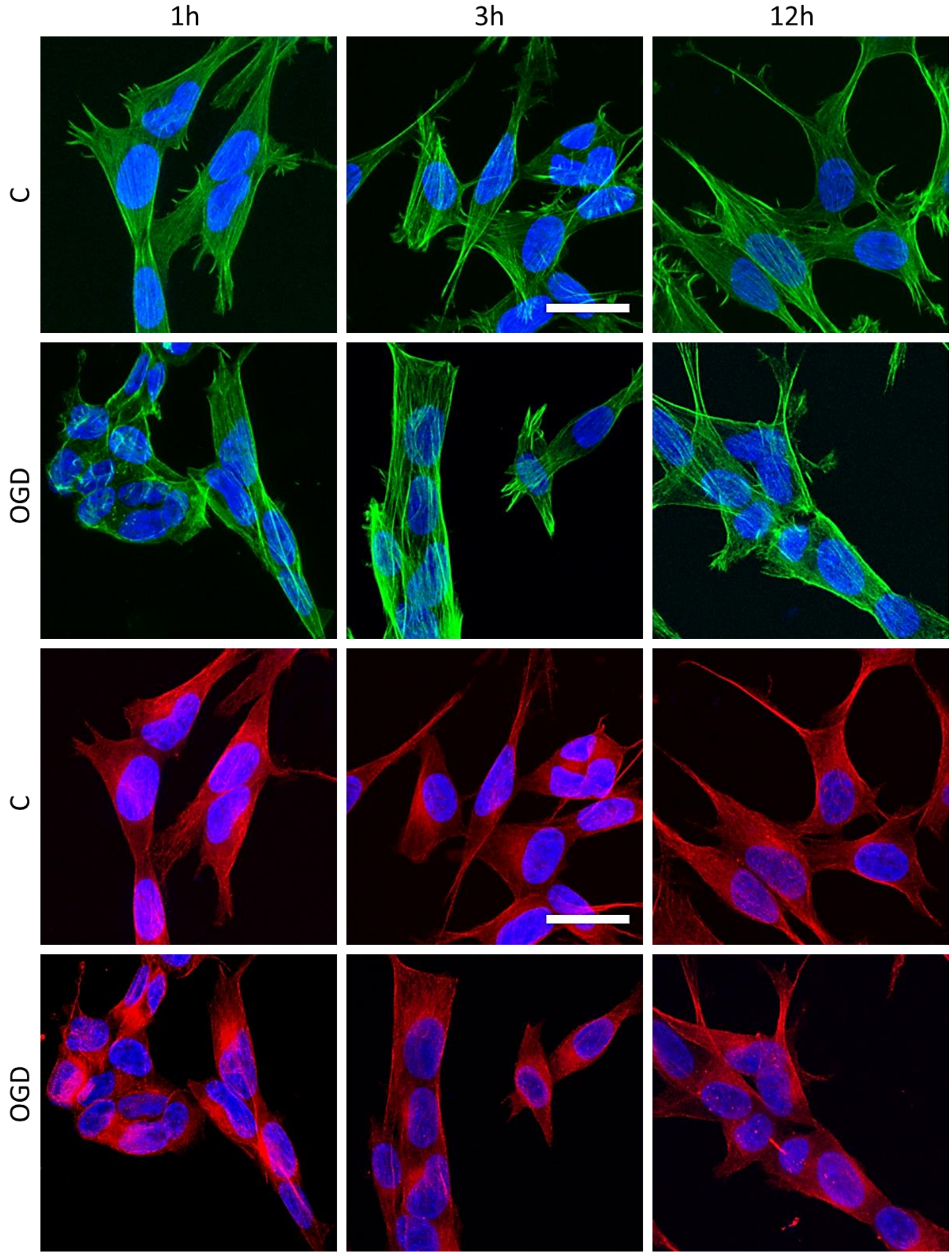

Figure 5.5. Confocal images of the actin and microtubular cytoskeleton in OGD-treated cells immediately after exposure. C (C, NB(+G)), OGD cells (OGD 1h, 3h, or 12h,NBA(-G)). Actin filaments were labeled with phalloidin conjugated with Alexa Fluor 488, microtubules with primary antibody conjugated with Cy3, and cell nuclei with Hoechst33342; scale bar 25 µm (reprinted from Zielinski et al. *Scientific Reports* **12** (2022) 16276 under CC-BY 4.0 license).

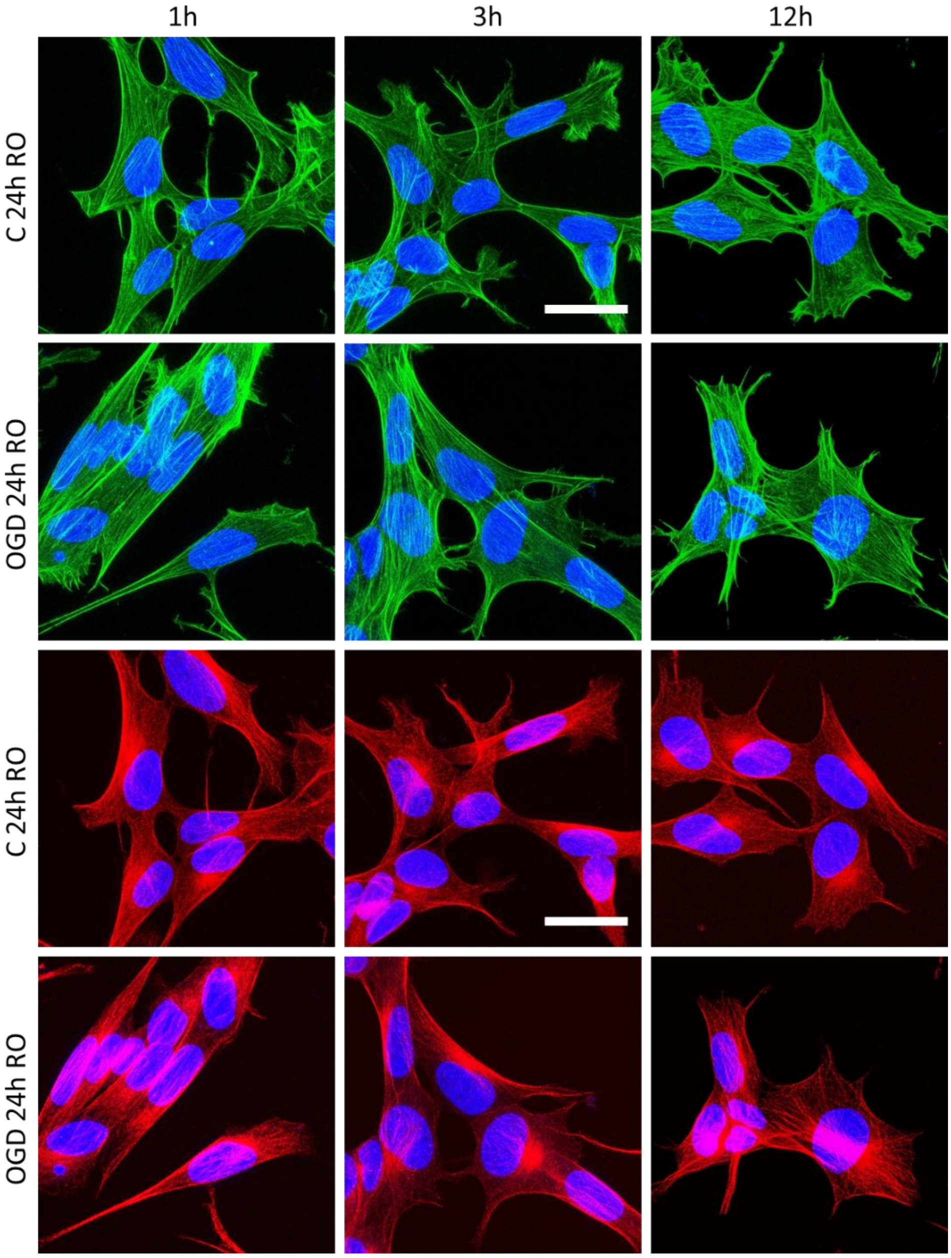

Figure 5.6. Confocal images of the actin and microtubular cytoskeleton in OGD-treated cells after 24h re-oxygenation. C (non-OGD cells (C 24h) kept in DMEM(+G) for the same time as reoxygenated OGD cells), OGD (reoxygenated OGD cells (RO 24h, DMEM(+G)). Actin filaments were labeled with phalloidin conjugated with Alexa Fluor 488, microtubules with primary antibody conjugated with Cy3, and cell nuclei with Hoechst33342; scale bar 25 µm (reprinted from Zielinski et al. *Scientific Reports* **12** (2022) 16276 under CC-BY 4.0 license).

The morphology of actin and microtubular cytoskeleton was similar regardless form the experimental group. Control and OGD-treated cells exhibit similar actin organization, showing actin bundles spanning over the whole cell without actin rods. The microtubule organization does not reveal any significant alterations regardless of the experimental group. The only exception was for cells visualized directly after 1h exposure to OGD conditions. SH-SY5Y cells altered their morphology from a widely spread to a packed one, suggesting a change of heigh and geometrical perimeters and coverage surface and, consequently, alterations in adhesion to the surface. These results are consistent with the AFM mechanical results showing the largest drop in the apparent Young's (elastic) modulus in the case of short conditioning. During prolonged exposure to OGD (3h and 12h), the organization of actin filaments was barely visible, supporting weak changes in nanomechanical properties. Altogether, these results indicate that the nanomechanical properties of SH-SY5Y cells in the OGD model are dominated by actin filament organization.

5.5. The effective spreading surface area of single cells

On the base of confocal images, to expand the analysis of cytoskeleton organization, a deeper analysis of the size of individual cells using images recorded by epi-fluorescent microscopy was performed (**Figure 5.7**).

Analysis of epi-fluorescence images revealed that OGD-treated cells exhibit lower surface area, indicating impairment in their spreading abilities and, consequently, decreased adhesion to the surface (**Figure 5.7**). After 24h of re-oxygenation, restoration of adhesive properties has been observed, which occurred in the recovery of surface area to values comparable with conditioned control groups. The most significant alterations in the spreading area were observed for OGD-treated cells (visualized immediately after the OGD exposure). Re-oxygenation allows SH-SY5Y cells to remodel the cytoskeleton and restore the surface area to the level in control, non-treated cells.

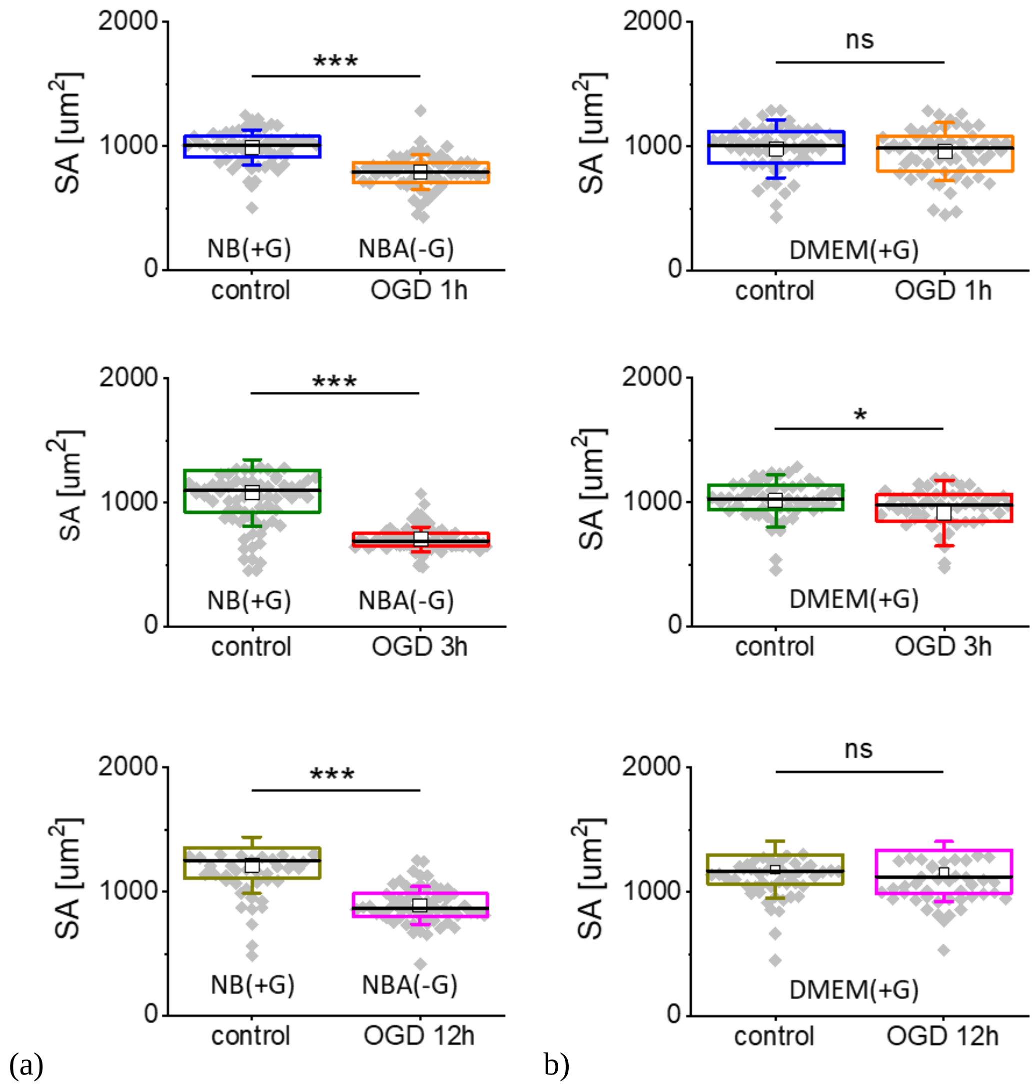

Figure 5.7. The effective spreading surface area of a single cell (SA) of SH-SY5Y cells after OGD (a) and following re-oxygenation (b). A single dot is the average surface area of individual cells. Boxplot represents mean (open square), median (black line), standard deviation (box), and 25% and 75% percentiles (whiskers) from $n = 60$ fluorescent images. Statistical significance determined: $p > 0.05$, $*p < 0.05$, $***p < 0.001$, and *ns* – not statistically significant (reprinted from Zielinski et al. *Scientific Reports* **12** (2022) 16276 under CC-BY 4.0 license).

Obtained results suggest that changes in the spreading area are responsible for alterations in the organization of the actin cytoskeleton, which in our case is strongly related to the OGD treatment of SH-SY5Y cells.

5.6. The nucleus-to-cell ratio confirms the shrinking of the cells

Alterations in the effective spreading surface area of a single cell and negligible reorganization of the actin cytoskeleton indicate that other mechanisms can be involved in changes in the nanomechanical properties of OGD-treated cells. One of the suggested factors might be an alteration in cell volume, which can be investigated by quantifying the ratio between cell surface (C) and cell nucleus (N) areas (**Figure 5.8**).

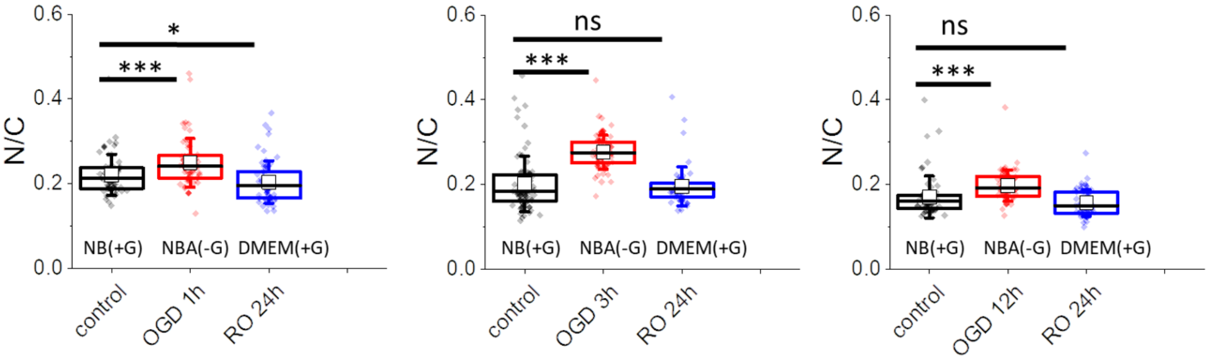

Figure 5.8. Nucleus to the cytoplasm (*N/C*) ratio of SH-SY5Y cells after OGD and following re-oxygenation. Single dots represent the average value of individual cells. Boxplots show mean (open square), median (line), and standard deviation (box) calculated from $n = 60$ cells. Statistical significance: *$p < 0.05$, ***$p < 0.001$, *ns* – not statistically significant (reprinted from Zielinski et al. *Scientific Reports* **12** (2022) 16276 under CC-BY 4.0 license).

The N/C ratio allows for assessing the contribution of cell nuclei in the surface area of a single cell. If N/C close to 1 indicates the high impact of the nucleus in the cell surface area. N/C close to 0 shows a low contribution of the nucleus in the projection area of a single cell. Analysis of the N/C ratio for SH-SY5Y cells affected with OGD conditions revealed that immediately after OGD, cell nuclei contribution in the cell surface area significantly increased in all examined experimental groups. Following 24h period of re-oxygenation, the N/C ratio returns to the control level suggesting the restoration of actin cytoskeleton architecture. A rough analysis of the cross-section of confocal images (from **Figure 5.5**) shows the OGD-induced alterations in cell height taken at the central area. The obtained values were 7.3 ± 1.4 μm ($n = 14$ cells), 8.3 ± 2.0 μm ($n = 11$), and 10.9 ± 2.8 μm ($n = 10$) for OGD-treated cells after 1h, 3h, and 12h exposure, correspondingly.

These data suggest that during OGD exposure, cells lose contact area to the surface due to lower adhesion. Alterations in cell adhesion results in decreased surface area, increased N/C ratio, and cell high.

5.7. Cofilin expression level in OGD-treated SH-SY5Y cells

Cofilin is an actin-regulating protein responsible for governing various cell processes such as migration and change of shape of the cell body. Cofilin activity can result, among others, from changes in calcium ions, reactive oxygen species, or ATP concentration [120,121]. Cofilin is responsible for the modulation of actin mesh organization by severing actin filaments and modulating the actin-depolymerization rate [209-211]. The results of cofilin expression presented as a relation between cofilin and phosphocofilin (referred to as p-cofilin) in control and OGD-treated SH-SY5Y cells are presented in **Figure 5.9.**

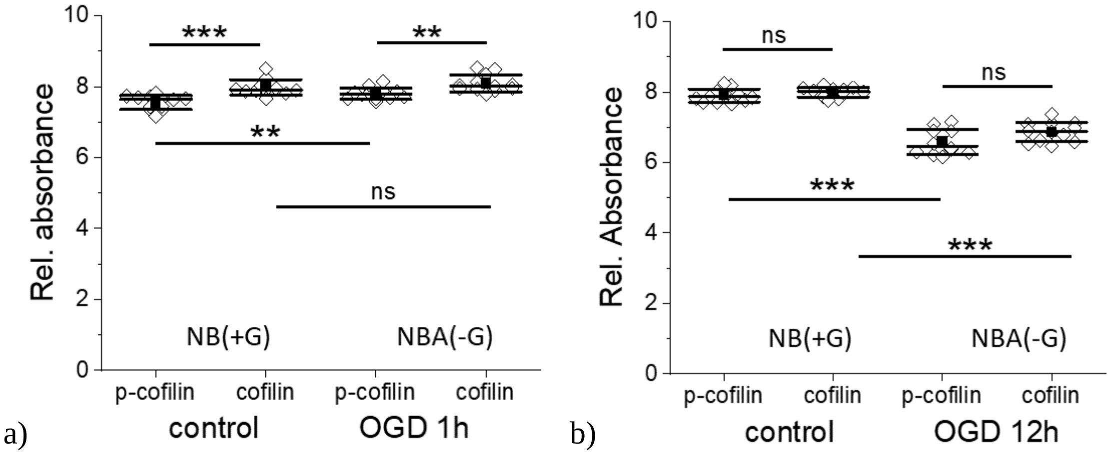

Figure 5.9. Expression of cofilin and phospho-cofilin (p-cofilin) corresponding to actin-severing activity in SH-SY5Y cell line evaluated immediately after 1h (a) and 12h (b) OGD exposure. Control cells were kept in NB(+G), while OGD cells were kept in NBA(-G). A mean (black square), median (black middle line), and standard deviation (SD, black lines below and above the middle one) were obtained from 3 independent repetitions. Statistical significance: $^{**}p < 0.01$, $^{***}p < 0.001$, *ns* – not statistically significant (reprinted from Zielinski et al. *Scientific Reports* **12** (2022) 16276 under CC-BY 4.0 license).

Observed alteration in the cofilin and p-cofilin levels in control cells could be explained by the consumption of glucose by proliferating cells. The glucose level in a given volume decreases during a certain culture time [212]. Notably, the results show that the cofilin and p-cofilin expression decreases with OGD duration. Cofilin/p-cofilin level assessed in control cells showed a 5% higher level of cofilin than p-cofilin ($p < 0.001$). Cells exposed to 1h OGD showed only a 3.5% higher concentration of cofilin than p-cofilin ($p < 0.002$). Cofilin expression in relation to p-cofilin vanishes in cells exposed to prolonged OGD (a similar protein level was observed in cells after 3h and 12h OGD). Comparison of the expression level of cofilins (or p-cofilins) for control and OGD-treated cells revealed particular changes. A significant change was found between control and 1h-OGD-treated cells ($p = 0.006$) for p-cofilin) and no difference was found for these cells in cofilin expression ($p = 0.198$). Regardless of the cofilin status, a large difference was noted between control and 3h-OGD-treated cells ($p < 0.0001$).

To conclude, the ratio between cofilin/p-cofilin alters significantly during 1h exposure to OGD (regardless of control or OGD group) and vanishes after prolonged (12h) exposure of cells to OGD. Since cofilin regulates the actin cytoskeleton by balancing its level with p-cofilin, the obtained results indicate that during the first hours after OGD strong remodeling of the actin cytoskeleton occurs.

5.8. Summary

Results obtained by using MTS and LDH assays show that SH-SY5Y cell culture exposure to OGD conditions leads to changes in the metabolic activity of living cells without significant alterations in cell survival between distinct OGD groups. Alterations in metabolic activity are related to disturbances in equilibrium (polymerization and depolymerization) of particular cytoskeleton components such as actin filaments and microtubules. A significant decrease in average cell projection area was observed for all mentioned experimental groups (1,3 and 12h), suggesting that actin integrity is crucial in OGD-induced cytoskeletal changes - failure in ATP production results in the reduction of actin polymerization. The non-changed activity of actin remodeling proteins, combined with disability in the polymerization of new actin fibers, results in changes in nanomechanical properties of short (1 h) exposure to OGD cells. During prolonged OGD exposure (12 h), cells respond to oxygen and glucose deprivation via compensation severing of actin via depletion in cofilin expression.

Additionally, the ratio of cofilin phosphorylation significantly increases in 12 h exposure samples. Following 24 h re-oxygenation, geometry perimeters of living cells, such as SA and N/C, return to the control level. The final summation of results obtained from the undifferentiated SH-SY5Y cell line is included in the following points:

- During OGD conditioning of SH-SY5Y, metabolic activity fluctuations are correlated with the alteration of biomechanical properties
- Changes in biomechanical properties are caused by the re-organization of the actin network and microtubular cytoskeleton (observed in the confocal microscope and quantitatively by analysis of the projection area of a single cell)
- SH-SY5Y cells modify biomechanical properties during short OGD conditioning; after 24h, re-oxygenation organization of the cytoskeleton recovers to control
- Prolonged exposition to OGD (12h) results in a permanent alteration of biomechanical properties of SH-SY5Y cells
- Re-organization of the actin cytoskeleton is related to alterations in diminished ATP production and activity of cofilin

The introduction of nanomechanical studies on undifferentiated SH-SY5Y cell models gave insight into actin-related changes in the deformability of cells. The application of this model allowed for the investigation role of actin in the deformability of OGD-treated cells in duration related manner.

6. Nanomechanical properties of primary hippocampal neurons after OGD

6.1. Objectives

Stroke induces changes in the brain; thus, the main targets are neurons. Here, the results on the effect of OGD on mice primary hippocampal neurons are presented. Analogously as for neuroblastoma SH-SY5Y cells, the nanomechanical properties of neurons were assessed by applying AFM to quantify the biomechanical and rheological properties of mice primary hippocampal E18 neurons subjected to OGD and RO. The main objectives of the study were the following. First, how do the mechanical and rheological of neurons changes in response to OGD exposure? Can such changes be associated with actin filaments and/or microtubule organization? Does the mechanism related to the regulatory role of cofilin participate in neuron response to OGD? To answer these questions, AFM indentation and microrheological measurements were applied to OGD-treated neurons. These measurements were accompanied by fluorescent visualization of actin and microtubular networks inside the neurons and determination of cofilin/p-cofilin expression level.

6.2. Nanomechanical properties of neurons at indentation depths

AFM measurements on neurons were conducted analogously, like for SH-SY5Y cells. Indenting neurons was carried out within the nuclear region of the cells. Recalling that AFM can measure only cells attached to the underlying substrate, in the first step, the mechanical properties of neurons were determined for cells exposed to OGD with two oxygen concentrations, i.e., 5% and 0.1%. In both cases, cells were exposed to OGD conditions for 1h. The oxygen concentration in control cells was set to 18% (**Figure 6.1**).

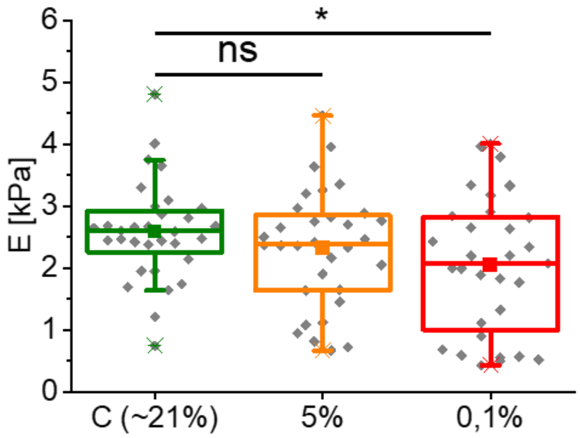

Figure 6.1. Young's modulus of neurons exposed to OGD at two oxygen concentrations (5% and 0.1%). The total number of neurons measured for each condition was 30. Box-plot represents mean (square), median (middle line), and standard deviation (SD, outside lines) were obtained from at least 3 independent repetitions. Statistical significance (*ns* – not statistically significant, $*p < 0.05$).

The results show that neurons soften (Young's modulus decreases) as oxygen concentration decreases (2.59 ± 0.80 kPa, n = 32 cells; 2.33 ± 0.95 kPa, n = 32 cells, 2.05 ± 1.09 kPa, n = 32 cells for control (~21%), 5% and 0.1% oxygen concentration in the atmosphere). As the significant drop of Young's modulus was observed for neurons exposed to OGD with 0.1% oxygen concentration ($p = 0.04193$), this oxygen concentration was kept constant while OGD exposure time was extended to 3h. The results showing the comparison between the control, untreated and OGD-treated neurons are presented in **Figure 6.2**. Mechanical properties of neurons were determined for two indentation depths, i.e., 400 nm and 1200 nm. Five groups of results were compared: *(1)* control, untreated neurons (C, NB(+G)), *(2)* two sham-operated control, untreated neurons (C 1 1h & C 3h; culture medium NB(G+) replaced NB(G+) for 1 and 3h, respectively), and two groups of OGD-treated neurons (neurons were exposed to OGD for 1h and 3h being cultured in NBA(-G) medium).

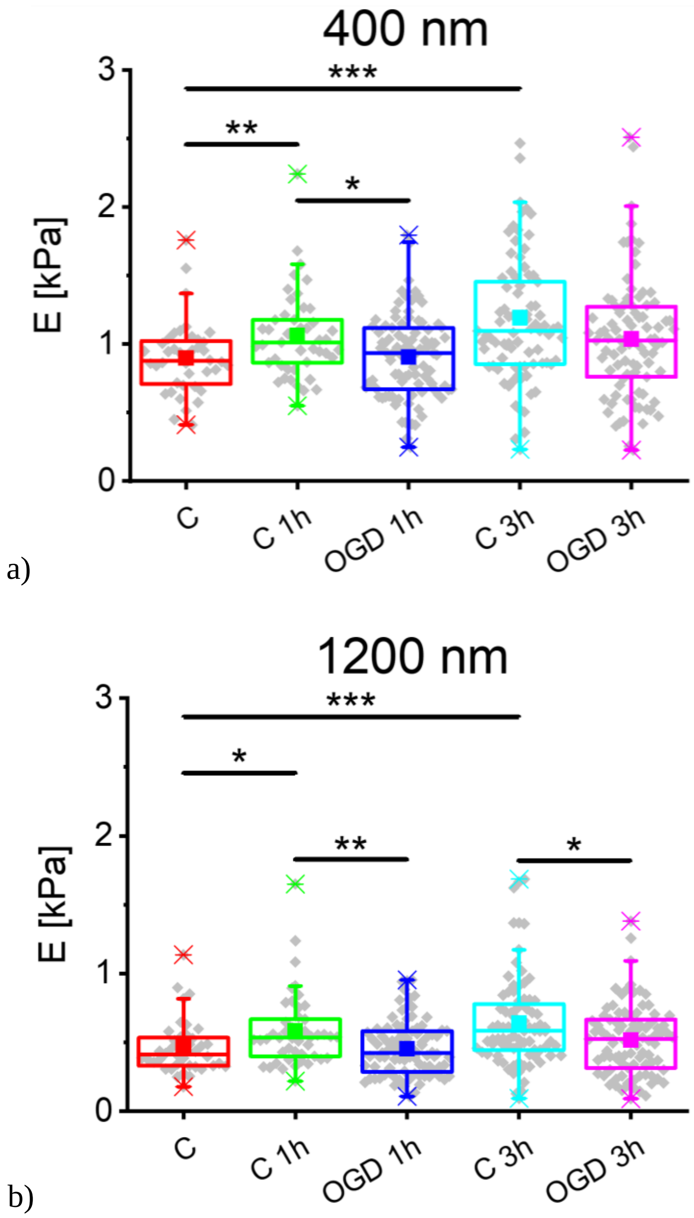

Figure 6.2. Nanomechanical properties of mice primary hippocampal neurons after OGD treatment, quantified by the apparent Young's modulus calculated for the indentation depth of 400 nm **(a)** and 1200 nm **(b)**. Notation: C – control, untreated neurons cultured in NB(+G)); C 1h & C 3h – sham-operated controls (untreated neuron culture in which NB(+G) was replaced with NB(G+) kept in culture for 1 and 3h, respectively; OGD 1h & OGD 3h – neurons exposed to OGD for 1h and 3h, in NBA(-G) medium. Box plots represent mean (square), median (middle line), and standard deviation (SD, outside lines) were obtained from at least 3 independent repetitions. Statistical significance (*$p < 0.05$; **$p < 0.01$).

The results show that at the indentation depths of 400 nm, the elastic modulus decreased only for neurons after 1h OGD (0.91 ± 0.30 kPa, n = 91 neurons, p = 0.01181) compared to sham operating control (C 1h, 1.06 ± 0.32 kPa, n = 45). For longer exposure to OGD (3h), the mechanical properties of neurons remained unaltered. The elastic modulus was 1.04 ± 0.43 kPa (n = 90), while Young's modulus for neurons belonging to the corresponding sham operating control was 1.19 ± 0.52 kPa (n = 85). Interestingly, the elastic modulus of neurons cultured in NB(+G) without medium exchange was lower, i.e., 0.90 ± 0.27 kPa (n = 40).

In contrast to results obtained for SH-SY5Y cells (**Figure 5.2**), the mechanical properties of neurons determined for larger indentation depth (1200 nm) were more visible and dependent on the OGD exposure. After 1h exposure to OGD, Young's modulus of neurons was smaller, i.e., 0.45 ± 0.20 kPa (n = 91, p = 0.00593), than the modulus for control, untreated neurons 0.58 ± 0.27 kPa (n = 45). Neurons after 3h exposure to OGD were characterized by moduli of 0.52 ± 0.25 kPa (n = 90, p = 0.01672). The modulus value of the corresponding sham operating control was 0.64 ± 0.33 kPa (n = 85). Summarizing, neurons exposed to OGD became softer (Young's modulus decreases). The larger neuron deformability was observed for more prolonged exposure to OGD but only for larger indentation depth (1200 nm).

6.3. Microrheology of OGD-treated neurons

Few studies have shown that nanoindentation measurements are insufficient to fully describe cell mechanical properties (e.g.,[213]). It agrees with the results presented in the previous section showing a smaller difference between untreated and OGD-treated neurons. Therefore, in the next step, the rheological properties of neurons were quantified. (**Figure 6.3)**. In microrheological measurements, sinusoidal oscillations with an amplitude of 50 nm are applied at a certain indentation depth (below 1 micron). From these measurements, the storage G' and loss G'' moduli were determined and plotted as a function of oscillation frequency ranging from 0.5 Hz to 120 Hz

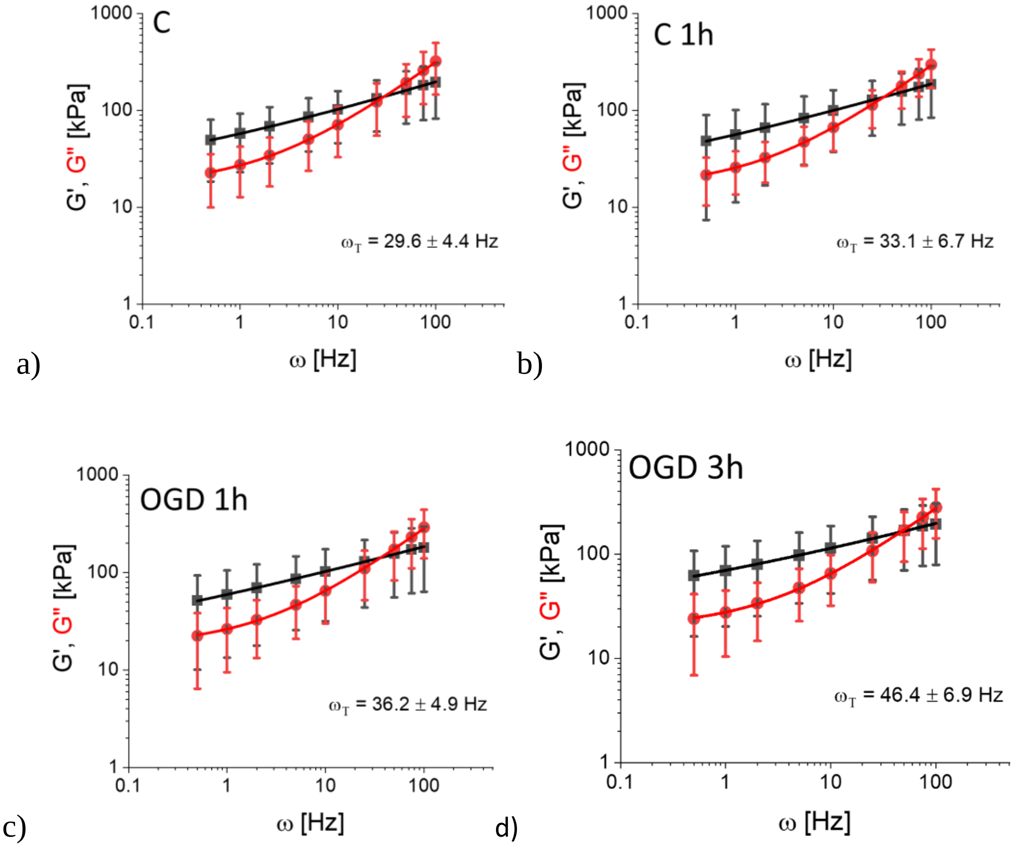

Figure 6.3. The log-log relations of the storage G’ (black dots) and loss G” (red dots) moduli plotted as a function of the frequency of oscillation of mice primary neurons exposed to (a) control (C), (b) sham-operated control (C 1h), (c) OGD 1h, and (d) OGD 3h. Each point denotes a mean and standard deviation of 30 to 50 neurons.

The results show power-law relationships between storage and loss modulus, which allows for applying the theoretical models (described in detail in the 3.6.4). Based on this, the transition frequency was determined. The transition frequency is a frequency where storage modulus equals loss modulus. Its value describes at which frequency the material passes from a solid-like to a fluid-like regime. The values of transition frequency were the following: 29.6 Hz ± 4.4 Hz for control, untreated neurons, 33.1 Hz ± 6.7 Hz for untreated neurons in sham operating control conditions, 36.2 Hz ± 4.9 Hz for neurons exposed for 1h OGD, and 46.4 Hz ± 6.9 Hz for neurons exposed for 3h OGD. To conclude, these findings showed that longer exposure of neurons to OGD inhibits the neuron transition to the fluid-like regime.

6.4. Viability of mice primary hippocampal neurons in OGD conditions

To evaluate the survival of mice primary hippocampal neurons exposed to OGD, live/dead staining was applied. Four groups of neurons were compared, C – non-treated (NB(+G)), no medium exchange), C S-O – sham operating control, in which culture media was exchanged (NB(+G)), OGD 1h – neurons exposed to 1h OGD, and OGD 3h – neurons exposed to 3h OGD (NBA(-G)). In parallel, to assess the survival of cells in re-oxygenation, a viability assay was conducted after 24 hours of re-oxygenation (RO-24h) in oxygen conditions (O_2 and CO_2 concentration: 18% and 5%, respectively) and in the presence of glucose (4500 mg/l). **Figure 6.4.** presents fluorescent images of cells after live/dead staining. The live/dead staining shows that the number of dead neurons increased upon OGD exposure. For longer OGD exposure, a larger number of dead cells was observed. Applied re-oxygenation of neurons (24 h culture in complete oxygen and glucose conditions) did not revert the process as the number of dead cells increased. This denotes that OGD damages the neurons, causing their death on a longer time scale. The level of immediate death after OGD was smaller.

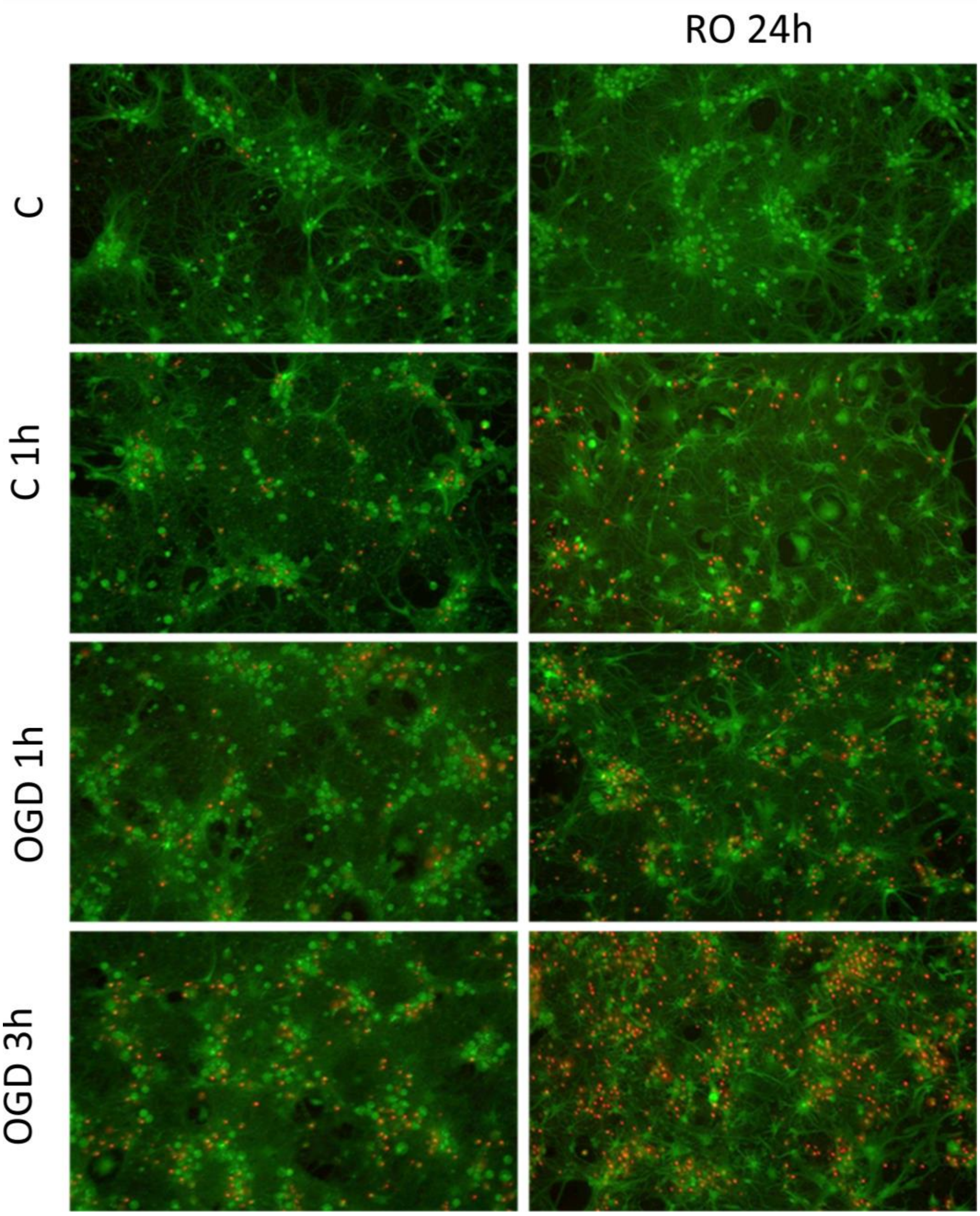

Figure 6.4. Epi-fluorescence images of mice primary hippocampal neurons stained with live/dead assay. Notation: C – control, untreated cells (NB(+G)); C 1h – sham-operated control NB(+G) exchanged to NB(+G); OGD 1h & OGD 3h – OGD treated neurons (NB(+G) exchanged to NBA(-G)), RO 24h – reoxygenated neurons in the corresponding culture conditions. Staining: green – calcein-AM fluorescence marking living neurons; red – propidium iodide intercalated with DNA, indicating dead neurons.

A quantitative analysis of neuron viability is shown in **Figure 6.5**.

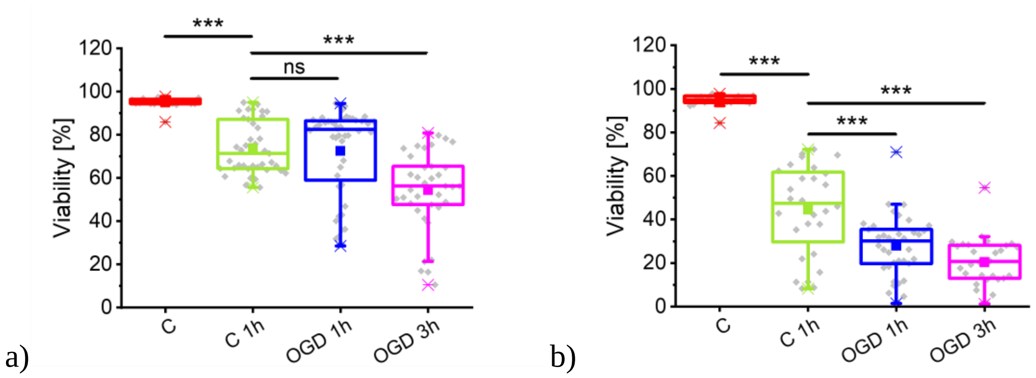

Figure 6.5. Neuron viability determined directly after OGD exposure (a) and after 24 h of re-oxygenation (b). Notation: C – control, untreated cells (NB(+G)); C S-O – sham-operated control NB(+G) exchanged to NB(+G); OGD 1h & OGD 3h – OGD treated neurons (NB(+G) exchanged to NBA(-G)), R-O 24h – reoxygenated neurons in the corresponding culture conditions. A mean (square), median (middle line), and standard deviation (SD, outside lines) were obtained from 3 independent repetitions. Statistical significance (*ns* – not statistically significant, ***$p < 0.001$).

Control, untreated neurons maintain a high level of viability throughout the experiments (OGD and R-O). The viability level was 94.997% ± 2.424% and 94.647% ± 2.885%, respectively. In sham-operating control, the culture exchange (NB(+G) to NB(+G)) affected the neuron viability, which dropped to 73.841% ± 12.067% (OGD) and to 44.518% ± 20.589% (R-O). After 1h exposure to OGD, there was no significant drop in the viability of neurons compared to sham-operating controls (72.593% ± 20.536%) determined directly after OGD. However, after 24h R-O, a drop to 27.886% ± 13.9995% was observed. After 3h OGD exposure, a further decrease in neuron viability was noted, i.e., viability level equals 54.352% ± 18.570% determined directly after OGD. It was even lower after 24h R-O (20.418% ± 10.962%). These results indicate that neurons underwent permanent injury after exposure to OGD.

6.5. Cytoskeleton in neurons exposed to OGD

Knowing that both mechanical and rheological properties of cells manifest the status of the cytoskeleton, especially the actin filament and microtubule organization [199,213,214], the two main cytoskeletal components were visualized by confocal microscope (**Figures 6.6 and 6.7**).

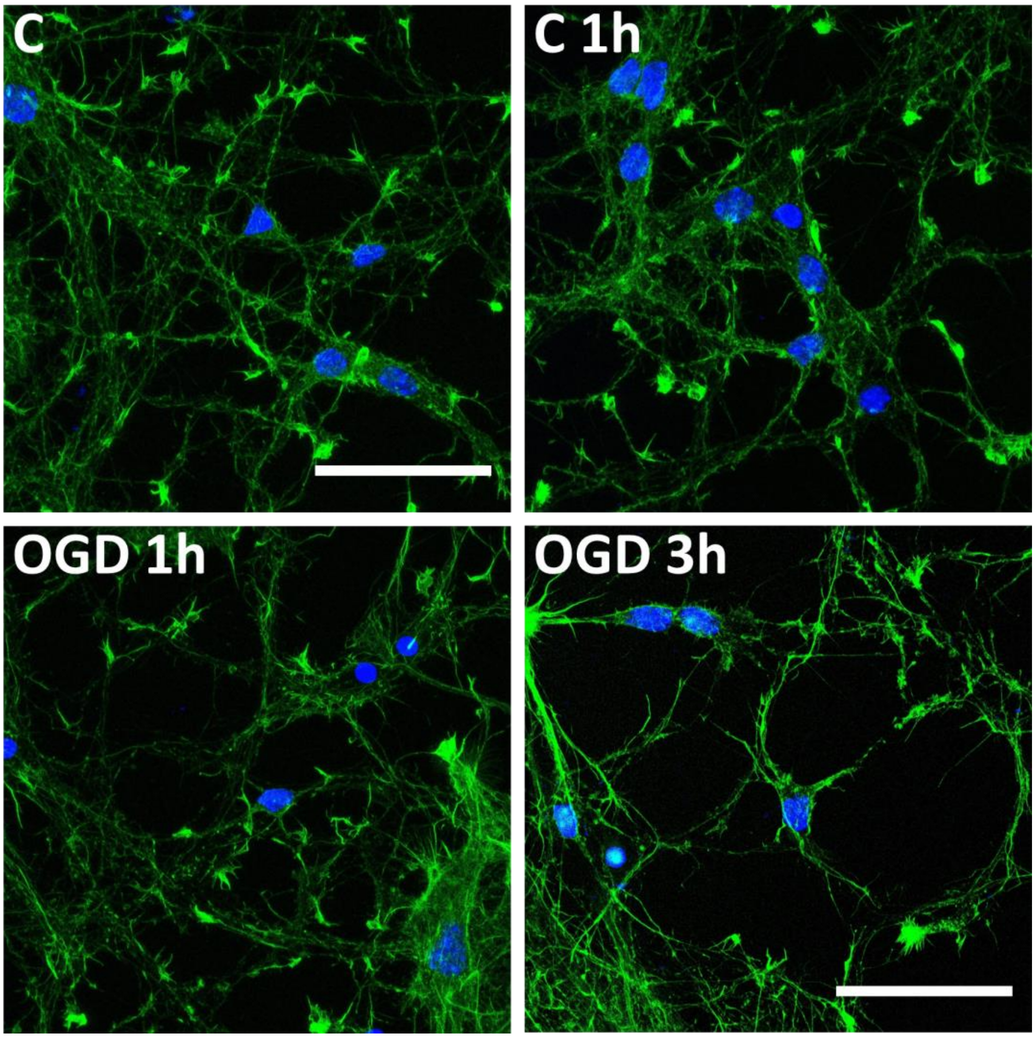

Figure 6.6. Confocal images of the actin cytoskeleton in OGD-treated cells. Notation: C – control, untreated cells (NB(+G)); C 1h – sham-operated control NB(+G) exchanged to NB(+G); OGD 1h & OGD 3h – OGD treated neurons (NB(+G) exchanged to NBA(-G)), R-O 24h – reoxygenated neurons in the corresponding culture conditions. Staining: actin filaments (green) – phalloidin conjugated with Alexa Fluor 488, cell nuclei (blue) – Hoechst33342.

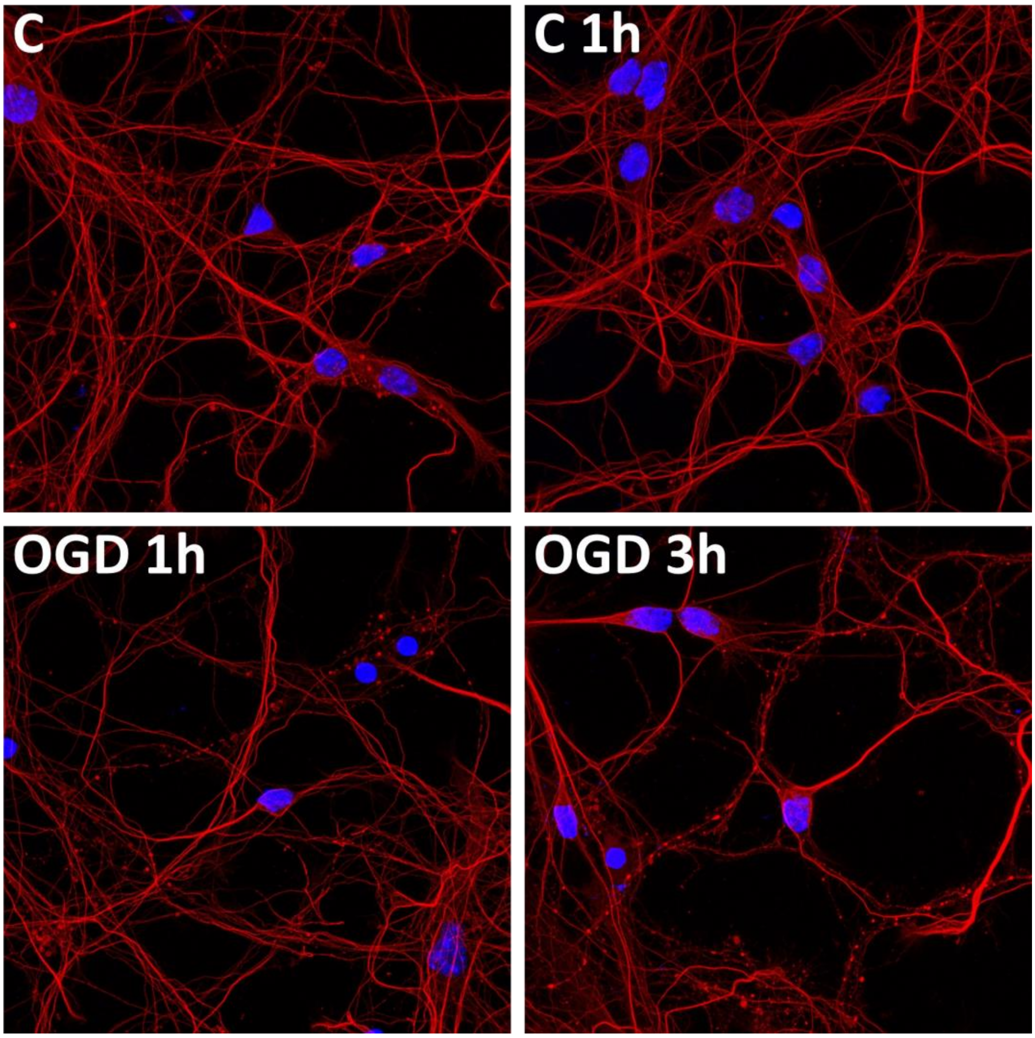

Figure 6.7. Confocal images of the microtubular cytoskeleton in OGD-treated cells. Notation: C – control, untreated cells (NB(+G)); C 1h – sham-operated control NB(+G) exchanged to NB(+G); OGD 1h & OGD 3h – OGD treated neurons (NB(+G) exchanged to NBA(-G)), R-O 24h – reoxygenated neurons in the corresponding culture conditions. Staining: microtubules (red) – primary antibody conjugated with Cy3, cell nuclei (blue) – Hoechst33342.

The fluorescent images show that the morphology of actin and the microtubular networks for control and OGD-treated neurons. The untreated neurons (control) and sham-operated control samples showed that both actin filaments and microtubular networks are similar. These cytoskeletal elements remained unaffected in cells attached to the surface after media exchange. The changes are observed in OGD-treated neurons. After 1h OGD, the actin filaments seem unchanged, but the microtubular network is altered. Longer exposure of neurons to OGD resulted in the deterioration of microtubule organization and disruption of their integrity. Additionally, changes in the network of actin filaments became visible. The intensity and presence of actin located in regions of dendritic spines drop significantly after OGD exposure. The actin cytoskeleton present in the cell body region shows disordered and dense structures.

6.6. Topography of mice primary hippocampal neurons

Topography images of dried neurons, recorded by AFM, delivered complementary information on cell morphology to that acquired by confocal microscopy (**Figure 6.8**).

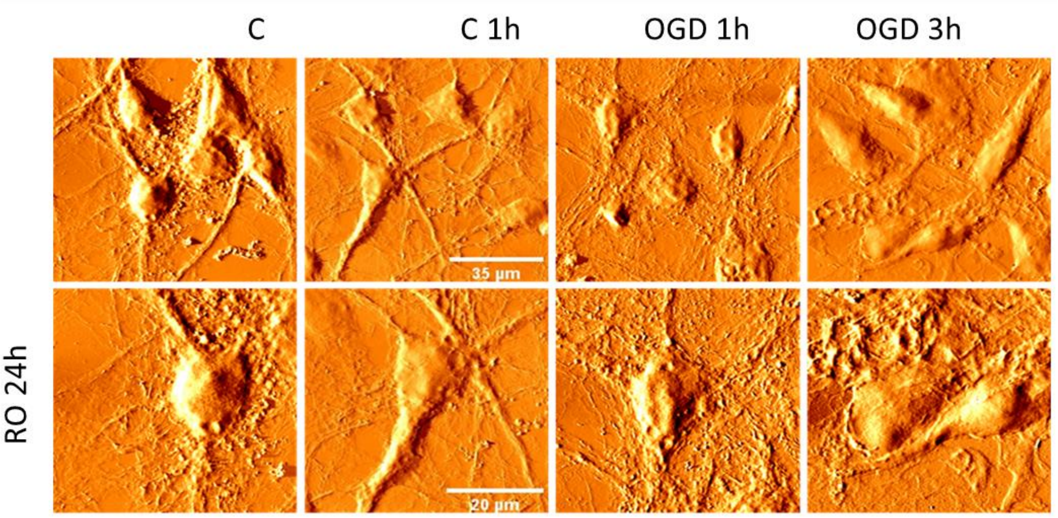

Figure 6.8. AFM topography images of neurons exposed to OGD compared to control, untreated cells, and sham-operating control. Notation: C – control, untreated cells (NB(+G)); C 1h – sham-operated control NB(+G) exchanged to NB(+G); OGD 1h & OGD 3h – OGD treated neurons (NB(+G) exchanged to NBA(-G)), RO 24h – reoxygenated neurons in the corresponding culture conditions.

Scanning the neuron's surface with an AFM tip revealed lower integrity neuronal protrusions (dendrites, axons), which decreased in contrast to cell protrusions. Obtained images suggest disturbances in the organization of the cytoskeleton of protrusions.

6.7. Cofilin and phospho-cofilin phosphorylation level

Changes in the mechanics of SH-SY5Y cells were explained by a mechanism involving the relation between cofilin and phospho-cofilin (Chapter 5). Therefore, by analogy, the expression level of this actin-regulatory protein was assessed for neurons exposed to OGD using the Western blot (**Figure 6.9**).

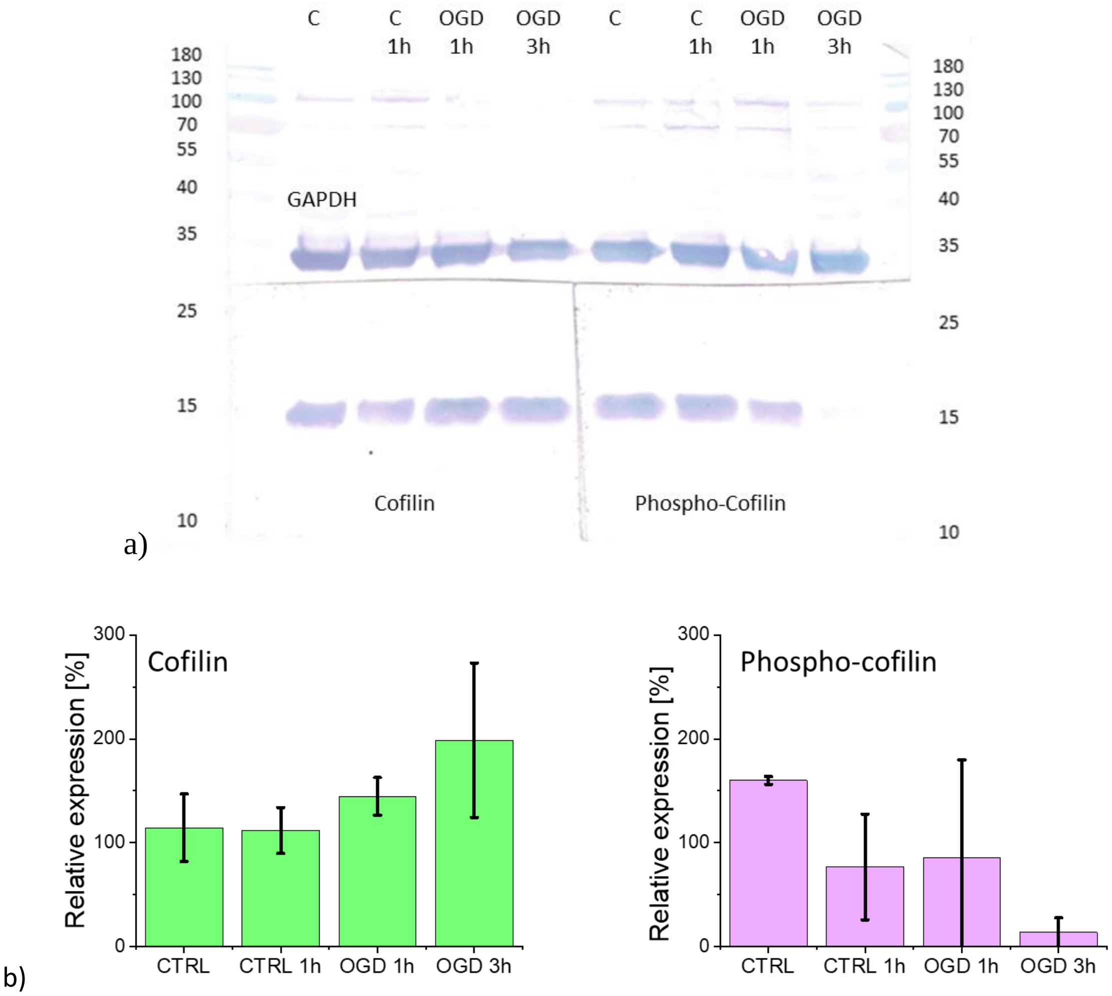

Figure 6.9. (a) Exemplary Western blot showing cofilin and phospho-cofilin expression in OGD-treated neurons, accompanied by densitometry-based quantification of the relative expression level. **(b)** A mean and standard deviation were calculated from data gathered from 3 independent repetitions. Notation: C – control, untreated cells (NB(+G)); C 1h – sham-operated control NB(+G) exchanged to NB(+G); OGD 1h & OGD 3h – OGD treated neurons (NB(+G) exchanged to NBA(-G)), RO 24h – reoxygenated neurons in the corresponding culture conditions.

The relative expression level was calculated from 3 independent repetitions applying the densitometric approach. The results showed that in OGD-treated neurons, the level of cofilin increased, accompanied by a simultaneous decrease in the phospho-cofilin level, which indicates that maintaining the balance between cofilin and phospho-cofilin is involved in OGD-related remodeling of the cell cytoskeleton.

6.8. Summary

Mice primary hippocampal neurons, exposed to OGD, respond in various ways, including alteration in mechanical and rheological properties of individual neurons. Such changes reflect, among others, alterations in neuron viability, actin filaments and microtubule organization, and expression level of cofilin/phospho-cofilin. By applying several methods like AFM, confocal microscopy, and Western blot, it was possible to observe how mechanical and rheological properties are related to biological markers of dysfunctions of neurons exposed to OGD. The main findings of the experiments described in this Chapter can be summarized as follows.

- Various mechanical and rheological properties characterize neurons exposed to OGD. The larger neuron deformability was observed for more prolonged exposure to OGD and at a larger indentation depth (1200 nm).
- Microrheological measurements revealed that longer OGD exposure of neurons to OGD inhibits the neuron transition to the fluid-like regime.
- Neuron viability results indicated that neurons underwent permanent injury after exposure to OGD, not recoverable by 24h R-O
- Changes in the actin filaments and microtubule organizations showed visible alterations after long exposure of neurons to OGD.
- In neurons, increased cofilin and decreased phospho-cofilin expression levels correlated with OGD exposure.

7. Discussion and conclusions

Oxygen and glucose deprivation (OGD) is applied to study cerebral ischemic stroke *in vitro* because it mimics the sudden disruption of blood flow to the brain [215]. Lots are known about the biological and medical aspects of stroke; however, to what extent the mechanics is involved is weakly elaborated. To fill the gap, in the study presented here, the atomic force microscope (AFM) was applied to quantify the mechanical and rheological properties of two cell models exposed to OGD, mimicking stroke conditions. AFM can be applied to quantify the mechanical or rheological properties of living cells [165-172]. Therefore, it can be widely applied to study the effects of various drugs (like cytoskeletal drugs, including cytochalasin D or nocodazole [199,214]) or of physical stimuli that affect cell mechanics [72]. The research has demonstrated that AFM-based elasticity measurements can detect changes early in the progression of various diseases, such as multiple sclerosis, various cancers, or muscular dystrophy [1, 3, 4, 180]. Current studies have also shown that tissue mechanics changes within the region affected by stroke and, at a distance from the stroke site, in a region of the contralateral and ipsilateral hemispheres [217]. Ultrasound elastography and AFM have shown the alterations in mechanical properties of the brain region severely affected by ischemia. Tissue affected by stroke reveals increased deformability as the shear modulus of the entire brain significantly decreases. Neuronal cells exhibit mechanosensitive characteristics and are highly responsive to altered mechanics of the surrounding environment [72,218]. Thus, alterations in the deformability of ischemic tissue also denote changes in the functioning of neurons and their nanomechanical response.

The mechanical and rheological properties of cells can be attributed to the organization of actin filaments [198,219]. To evaluate how cell morphology is related to mechanical properties, glioblastoma U118 MG and cervix cancer HeLa cells were measured by AFM. These cells display fibroblast-like and keratinocyte-like morphology, respectively. By applying cytochalasin D, an agent inhibiting actin filament polymerization, it was possible to relate cell shape to mechanical properties. Simultaneously, it has been demonstrated that the mechanical response of cells can be attributed to the remodeling of actin filaments.

Mechanisms governing alterations in the mechanical properties of neurons or even nervous tissue can be derived by measuring various cell types originating from normal and pathological nervous tissue. One of them is the neuroblastoma cell line SH-SY5Y because these undifferentiated cells exhibit neuroblast-like non-polarized morphology (cell body with few protrusions) and display markers characteristic of immature neurons. In addition, based on an analogy to glioblastoma U118 MG cells, there was a premise that alterations in the organization of actin filaments by AFM can be detected.

The mechanical response of undifferentiated SH-SY5Y cells has already been reported in chemically induced glutamate-mediated neurodegeneration [220]. The results showed the increased rigidity of SH-SY5Y cells upon 50 mM N-methyl-D-aspartate (NMDA) treatment. However, in this study, the experimental time was limited to 60 minutes, and maximum rigidity was observed after 20 minutes. To observe how the mechanical properties of cells change for a longer time, SH-SY5Y cells were subjected to OGD for 1h, 3h, and 12h, followed by 24h of re-oxygenation. AFM-based elasticity measurements were conducted at the shallow (actin cytoskeleton) and deep indentations (actin, microtubules, and deeper-lying organelles like cell nuclei). The results show cell softening as Young's modulus decreased in cells exposed to OGD. The results suggested that the cell cytoskeleton is responsible for the larger deformability of SH-SY5Y cells. A similar effect is observed for shallow indentation depth (400 nm) and deep indentation (1200 nm). The percentage difference seems unchanged in the case of both analyzed indentations, whereas in the case of 1200 nm, the cumulative effect of nanomechanics of actin cortex, microtubules, and cell nucleus is observed. The most significant Young's modulus decrease was detected in SH-SY5Y cells measured directly after OGD, especially after short-time OGD (i.e., 1h). After 24h re-oxygenation, the elastic properties of cells returned to the level of control cells. The cell viability (LDH assay) showed that the number of alive cells remained within 83–88% for both control and OGD-treated cells, suggesting no significant effect of OGD conditions on cell survival. However, cell metabolic activity measured using the MTS technique decreases significantly with OGD duration, oppositely to changes observed in nanomechanical measurements.

The following mechanism of OGD-induced deformability changes was proposed. In the initial phase, alterations in cell deformability are limited mainly to actin filaments reorganization in the actin cortex. The time-dependent gradual decrease of Young's modulus in control, non-OGD treated SH-SY5Y cells, regardless of the indentation depths (400 nm and 1200 nm), probably reflects the impact of glucose consumption on the mechanical properties of cells. The dynamic process of polymerization and/or depolymerization of actin filaments depends strongly on ATP availability. The low level of ATP affects the cytoskeleton status causing slow disassembly of cytoskeletal elements [221,222], in consequence, a gradual increase in the deformability of cells (i.e., cell softening). Furthermore, during the initial OGD, the mechanical properties of cells can be linked with the effect of cofilin on the organization of cortical actin. Severing and depolymerizing actin filaments induced by cofilin activity create short actin filaments with new barbed ends needed for their polymerization [223]. The effect of actin remodeling is discernible in cells incubated for 1 hour of OGD conditions. It is detectable in the effective surface area of the single-cell experiment, where 1-hour OGD results in a significant (~ 20%) reduction of the mean single-cell surface area and an increase in the cell height. These alterations are the premise that the actin scaffold becomes more sparse, and the cell gets softer. In the case of prolonged OGD exposure (3h and 12h), the cofilin-induced actin de-polymerization seems to be diminished. Changes in nanomechanical properties of prolonged OGD-treated cells are less significant. In the case of long-lasting OGD exposure, cells are metabolically impaired, and the number of metabolically active cells decreases. Cofilin activity is inhibited by phosphorylation of the serine residues at position 3 near the N-end for a longer OGD duration, resulting in polymerization and stabilization of actin filaments [224,225]. In consequence, cells with low metabolic activity become more rigid. After re-oxygenation, the surface area returned to control levels, but mechanical properties did not fully recover. Alterations in nanomechanical properties are visible but not significant. Observations from actin and tubulin in confocal microscopy do not reveal any significant change in their organization, which indicates that variation in cell mechanics cannot be explained only by actin dynamics regulation.

The better model for studying the effect of OGD are mice primary hippocampal neurons. Neurons exhibit large sensitivity to the deprivation of oxygen and glucose. Examination of cell survival by using live/dead assay excluded from further AFM experiments re-oxygenated controls and OGD groups. In contrast to the SH-SY5Y cells, neurons showing fully differentiated morphology, different expression profile, and loss of proliferation potential are more prone to OGD exposure and exhibit more different response mechanisms to OGD. It might result in the oversecretion of neurotransmitter – glutamate, leading to excitotoxicity through the interaction with N-methyl-D-aspartate (NMDA) receptors. Some reported data have elucidated that glutamate induces excitotoxicity in primary cultured neurons through oxidative damage and over-stimulation of NMDA receptors, leading to calcium homeostasis destruction [220]. Overexcitation of neuronal cell membrane leads to the opening of ion channels and further influx of sodium (Na^+) and calcium (Ca^{2+}) ions. The influx of calcium ions affects the nanomechanical properties of cells via the ADF/cofilin family of actin-binding proteins. Fluctuations of cofilin and phospho-cofilin expression in mice primary neurons are much more significant compared to those observed in OGD-treated SH-SY5Y cells. Level of cofilin, the active form, increases, whereas phosphor-cofilin decreases with exposure time. Consequently, actin fibers are prone to sever; therefore, ATP supply failure does not allow re-organizing actin bundles to create a uniform web. Other data suggest disrupting the equilibrium between fibrillar and globular actin (F and G actin) [226]. Observed on confocal images, the architecture of the actin cytoskeleton alters, and actin relocation from regions of dendritic spines has been reported, resulting in the disturbing ability of cell-cell interactions. As a cortical layer, the actin cytoskeleton plays a crucial role in the nanomechanical properties of the cell. Alterations in the distribution of actin bundles, the ratio of F and G actin, activity of ADF/cofilin family, and decrease of cellular ATP level might increase cell deformability or result in a weaker response of cells to fluctuations of environmental conditions such as media exchange. Similar to data obtained for SH-SY5Y cells, a statistically significant decrease of Young’s modulus is observed only for 1h treated with OGD conditions cells.

A significant drop in Young’s modulus for deep indentation (1200 nm) suggests the role of both components of the cytoskeleton in the elastic properties of OGD-treated neurons. Analysis of confocal images showed significant changes in the organization of the microtubular cytoskeleton. OGD exposure induces cracks in microtubules. Apart from mechanical support, microtubules and actin filaments in neurons fulfill one other crucial role: transport of cargo through neuronal protrusions to synaptic terminations. Transport along microtubules is realized via the activity of kinesin and dynein, whereas actin-related transport is combined with the functionality of myosins [227]. Dysfunction of intracellular transport responding to the transport of neurotransmitters and partially processed proteins results in the loss of excitability of neurons and is one of the causes of neuronal death [228].

Decreased cell survival after 24-hour re-oxygenation could result from excitotoxicity and exposure to reactive oxygen species (ROS). Intense entry of Na^+ triggers a secondary increase in intracellular Cl^- required for neuronal swelling via increasing osmotic pressure, resulting in an accumulation of water that directly leads to cell death [229]. Lack of expression of aquaporin 4, a membrane transporter regulating hydration, makes neurons more prone to necrosis caused by cytotoxic cell swelling [230,231].

Finally, gathering the results obtained for neuroblastoma SH-SY5Y cells and mice primary hippocampal neurons isolated from E18 embryos should be performed. Neuroblastoma SH-SY5Y cells exhibit different responses to OGD than mice primary neurons; however, some regulatory mechanisms might be common. Prolonged exposure to OGD conditions alters cell metabolism. Various mechanisms in immortalized cell lines protect against the consequences of further-mentioned injuries [232]. Some of the factors differentiating cell lines from primary cell cultures are involved in the regulation of calcium ions sensitivity (*via* calpains), regulation of ion distribution (membrane transporters, voltage-gated ion channels), and osmolar potential (presence of aquaporins in the cell membrane) [230,231,233]. Induction of cellular injuries can be activated via various biochemical processes such as perturbation of calcium homeostasis and disruption of ion equilibrium [233-235], malfunction of endoplasmic reticulum and mitochondria [236], and increased level of oxidative stress linked with DNA damage [237], disturbances in osmolar potential [233-235]. All mentioned factors affect cell morphology and architecture of the cytoskeleton, which might suggest changes in the mechanical properties of OGD-treated cells.

The activity of numerous actin-associated proteins responsible for regulating actin dynamic assembly and disassembly (polymerization/depolymerization of actin cytoskeleton) is obligatory in many biological processes, such as cell division, cell motility, endocytosis, and morphogenesis. These actin regulatory proteins contribute to nucleation, depolymerization, and fragmentation of the actin filaments, but simultaneously, they contribute to ATP-dependent polymerization [238-241]. One of these proteins is cofilin. Its main role is disassembling F-actin into tiny fragments of fibrous actin [125]. Importantly, the process of actin severing by cofilin is independent of energy addition. However, the extensive reorganization of actin filaments, especially actin polymerization, requires high energy supplies [242]. With disturbances in ATP production, the effect of actin severing via cofilin activity might be detected by applying AFM working in force-volume mode.

In conclusions, actin rearrangement seems to be crucial in the regulation of the nanomechanics of cells. Regulation of microfilament dynamics is realized through the activity of various actin-associated proteins, including activation of profilin, cofilin, and gelsolin, phosphorylation of myosin light chain, and changes in membrane spectrin cytoskeleton [243]. In the OGD in vitro stroke model, nanomechanical studies did not yet reveal much information about the sequence of changes in the cytoskeleton. Numerous research that use the OGD model to understand mechanisms involved in brain dysfunction [244,245] has demonstrated that the pathological process of ischemic stroke involves numerous mechanisms affecting various cell types. Apart from the nanomechanical role, cofilin is involved in the dynamic turnover of actin filaments and affects membrane integrity, receptor transport, and signal transduction. A better understanding of mechanisms governing cofilin-related cytoskeleton remodeling and potential ways of cofilin activity inhibition might induce neuroprotection by targeting diverse cellular components and multiple pathways [246,247]. Additionally, this knowledge could also contribute to the development of potential anticancer drugs.

8. Bibliography

1. Pyka-Fościak, G., Zemła, J., Lis, G. J., Litwin, J. A., & Lekka, M. (2020). Changes in spinal cord stiffness in the course of experimental autoimmune encephalomyelitis, a mouse model of multiple sclerosis. Archives of biochemistry and biophysics, 680, 108221.
2. Alibert, C., Goud, B., & Manneville, J. B. (2017). Are cancer cells really softer than normal cells?. Biology of the Cell, 109(5), 167-189.
3. Cross, S. E., Jin, Y. S., Tondre, J., Wong, R., Rao, J., & Gimzewski, J. K. (2008). AFM-based analysis of human metastatic cancer cells. Nanotechnology, 19(38), 384003.
4. Li, Q. S., Lee, G. Y., Ong, C. N., & Lim, C. T. (2008). AFM indentation study of breast cancer cells. Biochemical and biophysical research communications, 374(4), 609-613.
5. Wirtz, D., Konstantopoulos, K., & Searson, P. C. (2011). The physics of cancer: the role of physical interactions and mechanical forces in metastasis. Nature Reviews Cancer, 11(7), 512-522.
6. Kumar, S., & Weaver, V. M. (2009). Mechanics, malignancy, and metastasis: the force journey of a tumor cell. Cancer and Metastasis Reviews, 28(1), 113-127.
7. El Amki, M., & Wegener, S. (2017). Improving cerebral blood flow after arterial recanalization: a novel therapeutic strategy in stroke. International journal of molecular sciences, 18(12), 2669.
8. Yew, K. S., & Cheng, E. (2009). Acute stroke diagnosis. American family physician, 80(1), 33.
9. Khoshnam, S. E., Winlow, W., Farzaneh, M., Farbood, Y., & Moghaddam, H. F. (2017). Pathogenic mechanisms following ischemic stroke. Neurological Sciences, 38(7), 1167-1186.
10. Nowak, M. A., Nowak, M. M., Walczak, P. I., Olszewski, M. W., Natalia Niedziela, M. D., Warmus, P., & Adamczyk-Sowa, M. (2018). Serum inflammatory markers as predictors of neurological status in patients with

stroke in the course of hypertension: a two-center study. arterial hypertension, 22(2), 87-94.

11. Grysiewicz, R. A., Thomas, K., & Pandey, D. K. (2008). Epidemiology of ischemic and hemorrhagic stroke: incidence, prevalence, mortality, and risk factors. Neurologic clinics, 26(4), 871-895.
12. Johnson, W., Onuma, O., Owolabi, M., & Sachdev, S. (2016). Stroke: a global response is needed. Bulletin of the World Health Organization, 94(9), 634.
13. Katan, M. & Luft, A. (2018) Global burden of stroke. Semin. Neurol. 38, 208–211.
14. Sennfält, S., Norrving, B., Petersson, J., & Ullberg, T. (2019). Long-term survival and function after stroke: a longitudinal observational study from the Swedish Stroke Register. Stroke, 50(1), 53-61.
15. Minnerup J, Sutherland BA, Buchan AM, Kleinschnitz C. Neuroprotection for stroke: current status and future perspectives. Int J Mol Sci. 2012;13:11753–11772.
16. Derex, L., & Cho, T. H. (2017). Mechanical thrombectomy in acute ischemic stroke. Revue neurologique, 173(3), 106-113.
17. Sutherland, B. A., Minnerup, J., Balami, J. S., Arba, F., Buchan, A. M., & Kleinschnitz, C. (2012). Neuroprotection for ischaemic stroke: translation from the bench to the bedside. International Journal of Stroke, 7(5), 407-418.
18. Mestas, J., & Hughes, C. C. (2004). Of mice and not men: differences between mouse and human immunology. The Journal of Immunology, 172(5), 2731-2738.
19. Syvänen, S., Lindhe, Ö., Palner, M., Kornum, B. R., Rahman, O., Långström, B., ... & Hammarlund-Udenaes, M. (2009). Species differences in blood-brain barrier transport of three positron emission tomography radioligands with emphasis on P-glycoprotein transport. Drug metabolism and disposition, 37(3), 635-643.
20. Dávalos, A., Castillo, J., Serena, J., & Noya, M. (1997). Duration of glutamate release after acute ischemic stroke. Stroke, 28(4), 708-710.
21. Pulsinelli, W. A., & Brierley, J. B. (1979). A new model of bilateral hemispheric ischemia in the unanesthetized rat. Stroke, 10(3), 267-272.

22. Eklöf, B., & Siesjö, B. K. (1972). The effect of bilateral carotid artery ligation upon the blood flow and the energy state of the rat brain. Acta Physiologica Scandinavica, 86(2), 155-165.
23. Eklöf, B., & Siesjö, B. K. (1972). The effect of bilateral carotid artery ligation upon acid-base parameters and substrate levels in the rat brain. Acta Physiologica Scandinavica, 86(4), 528-538.
24. Pulsinelli, W. A., & Buchan, A. M. (1988). The four-vessel occlusion rat model: method for complete occlusion of vertebral arteries and control of collateral circulation. Stroke, 19(7), 913-914.
25. Globus, M. Y. T., Busto, R., Dietrich, W. D., Martinez, E., Valdes, I., & Ginsberg, M. D. (1988). Intra-ischemic extracellular release of dopamine and glutamate is associated with striatal vulnerability to ischemia. Neuroscience letters, 91(1), 36-40.
26. Longa, E. Z., Weinstein, P. R., Carlson, S., & Cummins, R. (1989). Reversible middle cerebral artery occlusion without craniectomy in rats. stroke, 20(1), 84-91.
27. Tamura, A., Graham, D. I., McCulloch, J., & Teasdale, G. M. (1981). Focal cerebral ischaemia in the rat: 1. Description of technique and early neuropathological consequences following middle cerebral artery occlusion. Journal of Cerebral Blood Flow & Metabolism, 1(1), 53-60.
28. Duverger, D., & MacKenzie, E. T. (1988). The quantification of cerebral infarction following focal ischemia in the rat: influence of strain, arterial pressure, blood glucose concentration, and age. Journal of Cerebral Blood Flow & Metabolism, 8(4), 449-461.
29. Watson, B. D., Dietrich, W. D., Busto, R., Wachtel, M. S., & Ginsberg, M. D. (1985). Induction of reproducible brain infarction by photochemically initiated thrombosis. Annals of Neurology: Official Journal of the American Neurological Association and the Child Neurology Society, 17(5), 497-504.
30. Markgraf, C. G., Kraydieh, S., Prado, R., Watson, B. D., Dietrich, W. D., & Ginsberg, M. D. (1993). Comparative histopathologic consequences of photothrombotic occlusion of the distal middle cerebral artery in Sprague-Dawley and Wistar rats. Stroke, 24(2), 286-292.

31. Zhang, Z., Zhang, R. L., Jiang, Q., Raman, S. B., Cantwell, L., & Chopp, M. (1997). A new rat model of thrombotic focal cerebral ischemia. Journal of cerebral blood flow & metabolism, 17(2), 123-135.
32. Shi, S., Mörike, K., & Klotz, U. (2008). The clinical implications of ageing for rational drug therapy. European journal of clinical pharmacology, 64(2), 183-199.
33. Hurn, P. D., Vannucci, S. J., & Hagberg, H. (2005). Adult or perinatal brain injury: does sex matter?. Stroke, 36(2), 193-195.
34. Hattiangady, B., Rao, M. S., & Shetty, A. K. (2008). Plasticity of hippocampal stem/progenitor cells to enhance neurogenesis in response to kainate-induced injury is lost by middle age. Aging cell, 7(2), 207-224.
35. Schmid-Elsaesser, R., Zausinger, S., Hungerhuber, E., Baethmann, A., & Reulen, H. J. (1998). A critical reevaluation of the intraluminal thread model of focal cerebral ischemia: evidence of inadvertent premature reperfusion and subarachnoid hemorrhage in rats by laser-Doppler flowmetry. Stroke, 29(10), 2162-2170.
36. Belayev, L., Alonso, O. F., Busto, R., Zhao, W., & Ginsberg, M. D. (1996). Middle cerebral artery occlusion in the rat by intraluminal suture: neurological and pathological evaluation of an improved model. Stroke, 27(9), 1616-1623.
37. Garcia, J. H., Wagner, S., Liu, K. F., & Hu, X. J. (1995). Neurological deficit and extent of neuronal necrosis attributable to middle cerebral artery occlusion in rats: statistical validation. Stroke, 26(4), 627-635.
38. Kawamura, S., Li, Y., Shirasawa, M., Yasui, N., & Fukasawa, H. (1994). Reversible middle cerebral artery occlusion in rats using an intraluminal thread technique. Surgical neurology, 41(5), 368-373.
39. Kawamura, S., Yasui, N., Shirasawa, M., & Fukasawa, H. (1991). Rat middle cerebral artery occlusion using an intraluminal thread technique. Acta neurochirurgica, 109(3), 126-132.
40. Memezawa, H., Smith, M. L., & Siesjö, B. K. (1992). Penumbral tissues salvaged by reperfusion following middle cerebral artery occlusion in rats. Stroke, 23(4), 552-559.

41. Nomura, S., Inoue, T., Ishihara, H., Koizumi, H., Suehiro, E., Oka, F., & Suzuki, M. (2014). Reliability of laser speckle flow imaging for intraoperative monitoring of cerebral blood flow during cerebrovascular surgery: comparison with cerebral blood flow measurement by single photon emission computed tomography. World Neurosurgery, 82(6), e753-e757.
42. Geri, O., Shiran, S. I., Roth, J., Artzi, M., Ben-Sira, L., & Ben Bashat, D. (2017). Vascular territorial segmentation and volumetric blood flow measurement using dynamic contrast enhanced magnetic resonance angiography of the brain. Journal of Cerebral Blood Flow & Metabolism, 37(10), 3446-3456.
43. Ginsberg, M. D., & Busto, R. (1997). Animal models of global and focal cerebral ischemia. Primer on cerebrovascular diseases, 124-126.
44. Van der Worp, H. B., Howells, D. W., Sena, E. S., Porritt, M. J., Rewell, S., O'Collins, V., & Macleod, M. R. (2010). Can animal models of disease reliably inform human studies?. PLoS medicine, 7(3), e1000245.
45. Lees, J. S., Sena, E. S., Egan, K. J., Antonic, A., Koblar, S. A., Howells, D. W., & Macleod, M. R. (2012). Stem cell-based therapy for experimental stroke: a systematic review and meta-analysis. International Journal of Stroke, 7(7), 582-588.
46. Fukuda, S., & del Zoppo, G. J. (2003). Models of focal cerebral ischemia in the nonhuman primate. ILAR journal, 44(2), 96-104.
47. Hanke, T. (2006). Lessons from TGN1412. The Lancet, 368(9547), 1569-1570.
48. Römer, P. S., Berr, S., Avota, E., Na, S. Y., Battaglia, M., Ten Berge, I., ... & Hünig, T. (2011). Preculture of PBMCs at high cell density increases sensitivity of T-cell responses, revealing cytokine release by CD28 superagonist TGN1412. Blood, The Journal of the American Society of Hematology, 118(26), 6772-6782.
49. Antonic, A., Sena, E. S., Donnan, G. A., & Howells, D. W. (2012). Human in vitro models of ischaemic stroke: a test bed for translation. Translational Stroke Research, 3(3), 306-309.

50. Tasca, C. I., Dal-Cim, T., & Cimarosti, H. (2015). In vitro oxygen-glucose deprivation to study ischemic cell death. In Neuronal Cell Death (pp. 197-210). Humana Press, New York, NY.

51. Kalogeris, T., Baines, C. P., Krenz, M., & Korthuis, R. J. (2012). Cell biology of ischemia/reperfusion injury. International review of cell and molecular biology, 298, 229-317.

52. Kurian, G. A., & Pemaih, B. (2014). Standardization of in vitro cell-based model for renal ischemia and reperfusion injury. Indian journal of pharmaceutical sciences, 76(4), 348-353.

53. Brown, R. C., & Davis, T. P. (2005). Hypoxia/aglycemia alters expression of occludin and actin in brain endothelial cells. Biochemical and biophysical research communications, 327(4), 1114-1123.

54. Matsumoto, K., Yamada, K., Kohmura, E., Kinoshita, A., & Hayakawa, T. (1994). Role of pyruvate in ischaemia-like conditions on cultured neurons. Neurological research, 16(6), 460-464.

55. Kalda, A., Eriste, E., Vassiljev, V., & Zharkovsky, A. (1998). Medium transitory oxygen-glucose deprivation induced both apoptosis and necrosis in cerebellar granule cells. Neuroscience letters, 240(1), 21-24.

56. Gwag, B. J., Lobner, D., Koh, J. Y., Wie, M. B., & Choi, D. W. (1995). Blockade of glutamate receptors unmasks neuronal apoptosis after oxygen-glucose deprivation in vitro. Neuroscience, 68(3), 615-619.

57. Goldberg, M. P., & Choi, D. W. (1993). Combined oxygen and glucose deprivation in cortical cell culture: calcium-dependent and calcium-independent mechanisms of neuronal injury. Journal of neuroscience, 13(8), 3510-3524.

58. Estevez, A. Y., Pritchard, S., Harper, K., Aston, J. W., Lynch, A., Lucky, J. J., ... & Erlichman, J. S. (2011). Neuroprotective mechanisms of cerium oxide nanoparticles in a mouse hippocampal brain slice model of ischemia. Free Radical Biology and Medicine, 51(6), 1155-1163.

59. Dong, W. Q., Schurr, A., Reid, K. H., Shields, C. B., & West, C. A. (1988). The rat hippocampal slice preparation as an in vitro model of ischemia. Stroke, 19(4), 498-502.

60. Richard, M. J., Saleh, T. M., El Bahh, B., & Zidichouski, J. A. (2010). A novel method for inducing focal ischemia in vitro. Journal of neuroscience methods, 190(1), 20-27.

61. Werth, J. L., Park, T. S., Silbergeld, D. L., & Rothman, S. M. (1998). Excitotoxic swelling occurs in oxygen and glucose deprived human cortical slices. Brain research, 782(1-2), 248-254.

62. Vornov, J. J., Tasker, R. C., & Coyle, J. T. (1994). Delayed protection by MK-801 and tetrodotoxin in a rat organotypic hippocampal culture model of ischemia. Stroke, 25(2), 457-464.

63. Gumbleton, M., & Audus, K. L. (2001). Progress and limitations in the use of in vitro cell cultures to serve as a permeability screen for the blood-brain barrier. Journal of pharmaceutical sciences, 90(11), 1681-1698.

64. Szafranska, K., Kruse, L. D., Holte, C. F., McCourt, P., & Zapotoczny, B. (2021). The wHole Story About Fenestrations in LSEC. Frontiers in physiology, 1468.

65. Liu, Y., Eaton, E. D., Wills, T. E., McCann, S. K., Antonic, A., & Howells, D. W. (2018). Human ischaemic cascade studies using SH-SY5Y cells: a systematic review and meta-analysis. Translational stroke research, 9(6), 564-574.

66. Kovalevich, J., & Langford, D. (2013). Considerations for the use of SH-SY5Y neuroblastoma cells in neurobiology. In Neuronal Cell Culture (pp. 9-21). Humana Press, Totowa, NJ.

67. He, Y., Yao, Y., Tsirka, S. E., & Cao, Y. (2014). Cell-culture models of the blood–brain barrier. Stroke, 45(8), 2514-2526.

68. Selvaraj, V., Jiang, P., Chechneva, O., Lo, U. G., & Deng, W. (2012). Differentiating human stem cells into neurons and glial cells for neural repair. Frontiers in Bioscience-Landmark, 17(1), 65-89.

69. Takahashi, K., & Yamanaka, S. (2006). Induction of pluripotent stem cells from mouse embryonic and adult fibroblast cultures by defined factors. Cell, 126(4), 663-676.

70. Durnaoglu, S., Genc, S., & Genc, K. (2011). Patient-specific pluripotent stem cells in neurological diseases. Stem Cells International, 2011.

71. Imaizumi, Y., & Okano, H. (2014). Modeling human neurological disorders with induced pluripotent stem cells. Journal of neurochemistry, 129(3), 388-399.

72. Moshayedi, P., Ng, G., Kwok, J. C., Yeo, G. S., Bryant, C. E., Fawcett, J. W., Franze, K. & Guck, J. (2014). The relationship between glial cell mechanosensitivity and foreign body reactions in the central nervous system. Biomaterials, 35(13), 3919-3925.

73. Alberts, B., Bray, D., Hopkin, K., Johnson, A. D., Lewis, J., Raff, M., ... & Walter, P. (2015). Essential cell biology. Garland Science.

74. Etienne-Manneville, S. (2004). Actin and microtubules in cell motility: which one is in control?. Traffic, 5(7), 470-477.

75. Schoumacher, M., Goldman, R. D., Louvard, D., & Vignjevic, D. M. (2010). Actin, microtubules, and vimentin intermediate filaments cooperate for elongation of invadopodia. Journal of Cell Biology, 189(3), 541-556.

76. Hohmann, T., & Dehghani, F. (2019). The cytoskeleton—a complex interacting meshwork. Cells, 8(4), 362.

77. Kristó, I., Bajusz, I., Bajusz, C., Borkúti, P., & Vilmos, P. (2016). Actin, actin-binding proteins, and actin-related proteins in the nucleus. Histochemistry and cell biology, 145(4), 373-388.

78. Yuan, A., Rao, M. V., & Nixon, R. A. (2012). Neurofilaments at a glance. Journal of cell science, 125(14), 3257-3263.

79. Hoffman, P. N., Cleveland, D. W., Griffin, J. W., Landes, P. W., Cowan, N. J., & Price, D. (1987). Neurofilament gene expression: a major determinant of axonal caliber. Proceedings of the National Academy of Sciences, 84(10), 3472-3476.

80. Xu, Z., Marszalek, J. R., Lee, M. K., Wong, P. C., Folmer, J., Crawford, T. O., ... & Cleveland, D. W. (1996). Subunit composition of neurofilaments specifies axonal diameter. The Journal of cell biology, 133(5), 1061-1069.

81. Križ, J., Zhu, Q., Julien, J. P., & Padjen, A. L. (2000). Electrophysiological properties of axons in mice lacking neurofilament subunit genes: disparity between conduction velocity and axon diameter in absence of NF-H. Brain research, 885(1), 32-44.

82. Perrot, R., Lonchampt, P., Peterson, A. C., & Eyer, J. (2007). Axonal neurofilaments control multiple fiber properties but do not influence structure or spacing of nodes of Ranvier. Journal of Neuroscience, 27(36), 9573-9584.

83. Gentil, B. J., Lai, G. T., Menade, M., Larivière, R., Minotti, S., Gehring, K., ... & Durham, H. D. (2019). Sacsin, mutated in the ataxia ARSACS, regulates intermediate filament assembly and dynamics. The FASEB Journal, 33(2), 2982-2994.

84. Akhmanova, A., & Steinmetz, M. O. (2010). Microtubule+ TIPs at a glance. Journal of cell science, 123(20), 3415-3419.

85. Helfand, B. T., Mendez, M. G., Pugh, J., Delsert, C., & Goldman, R. D. (2003). A role for intermediate filaments in determining and maintaining the shape of nerve cells. Molecular biology of the cell, 14(12), 5069-5081.

86. Jung, C., Chylinski, T. M., Pimenta, A., Ortiz, D., & Shea, T. B. (2004). Neurofilament transport is dependent on actin and myosin. Journal of Neuroscience, 24(43), 9486-9496.

87. Roy, S., Coffee, P., Smith, G., Liem, R. K., Brady, S. T., & Black, M. M. (2000). Neurofilaments are transported rapidly but intermittently in axons: implications for slow axonal transport. Journal of Neuroscience, 20(18), 6849-6861.

88. Frappier, T., Stetzkowski-Marden, F., & Pradel, L. A. (1991). Interaction domains of neurofilament light chain and brain spectrin. Biochemical journal, 275(2), 521-527.

89. Heimann, R., Shelanski, M. L., & Liem, R. K. (1985). Microtubule-associated proteins bind specifically to the 70-kDa neurofilament protein. Journal of Biological Chemistry, 260(22), 12160-12166.

90. Hirokawa, N., Hisanaga, S. H., & Shiomura, Y. (1988). MAP2 is a component of crossbridges between microtubules and neurofilaments in the neuronal cytoskeleton: quick-freeze, deep-etch immunoelectron microscopy and reconstitution studies. Journal of Neuroscience, 8(8), 2769-2779.

91. Barón-Mendoza, I., García, O., Calvo-Ochoa, E., Rebollar-García, J. O., Garzón-Cortés, D., Haro, R., & González-Arenas, A. (2018). Alterations in

neuronal cytoskeletal and astrocytic proteins content in the brain of the autistic-like mouse strain C58/J. Neuroscience Letters, 682, 32-38.

92. Dent, E. W., & Kalil, K. (2001). Axon branching requires interactions between dynamic microtubules and actin filaments. Journal of Neuroscience, 21(24), 9757-9769.

93. Gaillard, J., Ramabhadran, V., Neumanne, E., Gurel, P., Blanchoin, L., Vantard, M., & Higgs, H. N. (2011). Differential interactions of the formins INF2, mDia1, and mDia2 with microtubules. Molecular biology of the cell, 22(23), 4575-4587.

94. Lewkowicz, E., Herit, F., Le Clainche, C., Bourdoncle, P., Perez, F., & Niedergang, F. (2008). The microtubule-binding protein CLIP-170 coordinates mDia1 and actin reorganization during CR3-mediated phagocytosis. The Journal of cell biology, 183(7), 1287-1298.

95. Swiech, L., Blazejczyk, M., Urbanska, M., Pietruszka, P., Dortland, B. R., Malik, A. R., ... & Jaworski, J. (2011). CLIP-170 and IQGAP1 cooperatively regulate dendrite morphology. Journal of Neuroscience, 31(12), 4555-4568.

96. Cueille, N., Blanc, C. T., Popa-Nita, S., Kasas, S., Catsicas, S., Dietler, G., & Riederer, B. M. (2007). Characterization of MAP1B heavy chain interaction with actin. Brain research bulletin, 71(6), 610-618.

97. Kempf, M., Clement, A., Faissner, A., Lee, G., & Brandt, R. (1996). Tau binds to the distal axon early in development of polarity in a microtubule-and microfilament-dependent manner. Journal of Neuroscience, 16(18), 5583-5592.

98. Ridley, A. J., & Hall, A. (1992). The small GTP-binding protein rho regulates the assembly of focal adhesions and actin stress fibers in response to growth factors. Cell, 70(3), 389-399.

99. Ridley, A. J., Paterson, H. F., Johnston, C. L., Diekmann, D., & Hall, A. (1992). The small GTP-binding protein rac regulates growth factor-induced membrane ruffling. Cell, 70(3), 401-410.

100. Norman, J. C., Price, L. S., Ridley, A. J., Hall, A., & Koffer, A. (1994). Actin filament organization in activated mast cells is regulated by heterotrimeric and small GTP-binding proteins. The Journal of cell biology, 126(4), 1005-1015.

101. Ridley, A. J., & Hall, A. (1994). Signal transduction pathways regulating Rho-mediated stress fibre formation: requirement for a tyrosine kinase. The EMBO Journal, 13(11), 2600-2610.

102. Chrzanowska-Wodnicka, M., & Burridge, K. (1996). Rho-stimulated contractility drives the formation of stress fibers and focal adhesions. The Journal of cell biology, 133(6), 1403-1415.

103. Machesky, L. M., & Hall, A. (1997). Role of actin polymerization and adhesion to extracellular matrix in Rac-and Rho-induced cytoskeletal reorganization. The Journal of cell biology, 138(4), 913-926.

104. Subauste, M. C., Von Herrath, M., Benard, V., Chamberlain, C. E., Chuang, T. H., Chu, K., ... & Hahn, K. M. (2000). Rho family proteins modulate rapid apoptosis induced by cytotoxic T lymphocytes and Fas. Journal of Biological Chemistry, 275(13), 9725-9733.

105. Bourne, H. R., Sanders, D. A., & McCormick, F. (1991). The GTPase superfamily: conserved structure and molecular mechanism. nature, 349(6305), 117-127.

106. Bourne, H. R., Sanders, D. A., & McCormick, F. (1990). The GTPase superfamily: a conserved switch for diverse cell functions. Nature, 348(6297), 125-132.

107. Li, Z., Van Aelst, L., & Cline, H. T. (2000). Rho GTPases regulate distinct aspects of dendritic arbor growth in Xenopus central neurons in vivo. Nature neuroscience, 3(3), 217-225.

108. Spiering, D., & Hodgson, L. (2011). Dynamics of the Rho-family small GTPases in actin regulation and motility. Cell adhesion & migration, 5(2), 170-180.

109. Narumiya, S., Tanji, M., & Ishizaki, T. (2009). Rho signaling, ROCK and mDia1, in transformation, metastasis and invasion. Cancer and Metastasis Reviews, 28(1), 65-76.

110. Maekawa, M., Ishizaki, T., Boku, S., Watanabe, N., Fujita, A., Iwamatsu, A., ... & Narumiya, S. (1999). Signaling from Rho to the actin cytoskeleton through protein kinases ROCK and LIM-kinase. Science, 285(5429), 895-898.

111. Riento, K., & Ridley, A. J. (2003). ROCKs: multifunctional kinases in cell behaviour. Nature reviews Molecular cell biology, 4(6), 446-456.

112. Ohashi, K., Nagata, K., Maekawa, M., Ishizaki, T., Narumiya, S., & Mizuno, K. (2000). Rho-associated kinase ROCK activates LIM-kinase 1 by phosphorylation at threonine 508 within the activation loop. Journal of Biological Chemistry, 275(5), 3577-3582.

113. Lin, T., Zeng, L., Liu, Y., DeFea, K., Schwartz, M. A., Chien, S., & Shyy, J. Y. J. (2003). Rho-ROCK-LIMK-cofilin pathway regulates shear stress activation of sterol regulatory element binding proteins. Circulation research, 92(12), 1296-1304.

114. Song, X., Chen, X., Yamaguchi, H., Mouneimne, G., Condeelis, J. S., & Eddy, R. J. (2006). Initiation of cofilin activity in response to EGF is uncoupled from cofilin phosphorylation and dephosphorylation in carcinoma cells. Journal of cell science, 119(14), 2871-2881.

115. Bernstein, B. W., Painter, W. B., Chen, H., Minamide, L. S., Abe, H., & Bamburg, J. R. (2000). Intracellular pH modulation of ADF/cofilin proteins. Cell motility and the cytoskeleton, 47(4), 319-336.

116. Bowman, G. D., Nodelman, I. M., Hong, Y., Chua, N. H., Lindberg, U., & Schutt, C. E. (2000). A comparative structural analysis of the ADF/cofilin family. Proteins: Structure, Function, and Bioinformatics, 41(3), 374-384.

117. DesMarais, V., Ichetovkin, I., Condeelis, J., & Hitchcock-DeGregori, S. E. (2002). Spatial regulation of actin dynamics: a tropomyosin-free, actin-rich compartment at the leading edge. Journal of cell science, 115(23), 4649-4660.

118. Zigmond, S. H. (2004). Beginning and Ending an Actin Filament: Control at the Barbed End. current topics in developmental biology, 63, 146-189.

119. Andrianantoandro, E., & Pollard, T. D. (2006). Mechanism of actin filament turnover by severing and nucleation at different concentrations of ADF/cofilin. Molecular cell, 24(1), 13-23.

120. Bamburg, J. R., & Bernstein, B. W. (2008). ADF/cofilin. Current Biology, 18(7), 273-275.

121. Bernstein, B. W., & Bamburg, J. R. (2010). ADF/cofilin: a functional node in cell biology. Trends in cell biology, 20(4), 187-195.

122. Gibbs, J. B., Marshall, M. S., Scolnick, E. M., Dixon, R. A., & Vogel, U. S. (1990). Modulation of guanine nucleotides bound to Ras in NIH3T3 cells by oncogenes, growth factors, and the GTPase activating protein (GAP). Journal of Biological Chemistry, 265(33), 20437-20442.
123. DesMarais, V., Ghosh, M., Eddy, R., & Condeelis, J. (2005). Cofilin takes the lead. Journal of cell science, 118(1), 19-26.
124. van Rheenen, J., Condeelis, J., & Glogauer, M. (2009). A common cofilin activity cycle in invasive tumor cells and inflammatory cells. Journal of cell science, 122(3), 305-311.
125. Oser, M., & Condeelis, J. (2009). The cofilin activity cycle in lamellipodia and invadopodia. Journal of cellular biochemistry, 108(6), 1252-1262.
126. Condeelis, J. (2001). How is actin polymerization nucleated in vivo?. Trends in cell biology, 11(7), 288-293.
127. Nobes, C. D., & Hall, A. (1995). Rho, rac, and cdc42 GTPases regulate the assembly of multimolecular focal complexes associated with actin stress fibers, lamellipodia, and filopodia. Cell, 81(1), 53-62.
128. Rossman, K. L., Der, C. J., & Sondek, J. (2005). GEF means go: turning on RHO GTPases with guanine nucleotide-exchange factors. Nature reviews Molecular cell biology, 6(2), 167-180.
129. Snyder, J. T., Worthylake, D. K., Rossman, K. L., Betts, L., Pruitt, W. M., Siderovski, D. P., ... & Sondek, J. (2002). Structural basis for the selective activation of Rho GTPases by Dbl exchange factors. Nature structural biology, 9(6), 468-475.
130. Kligys, K., Claiborne, J. N., DeBiase, P. J., Hopkinson, S. B., Wu, Y., Mizuno, K., & Jones, J. C. (2007). The slingshot family of phosphatases mediates Rac1 regulation of cofilin phosphorylation, laminin-332 organization, and motility behavior of keratinocytes. Journal of Biological Chemistry, 282(44), 32520-32528.
131. Huang, T. Y., DerMardirossian, C., & Bokoch, G. M. (2006). Cofilin phosphatases and regulation of actin dynamics. Current opinion in cell biology, 18(1), 26-31.

132. Hall, A. (1992). Ras-related GTPases and the cytoskeleton. Molecular biology of the cell, 3(5), 475-479.
133. Nobes, C., & Hall, A. (1994). Regulation and function of the Rho subfamily of small GTPases. Current opinion in genetics & development, 4(1), 77-81.
134. Nobes, C. D., & Hall, A. (1995). Rho, Rac and Cdc42 GTPases: regulators of actin structures, cell adhesion and motility. Biochemical Society Transactions, 23(3), 456-459.
135. Shi, Y., Zhang, L., Pu, H., Mao, L., Hu, X., Jiang, X., ... & Chen, J. (2016). Rapid endothelial cytoskeletal reorganization enables early blood–brain barrier disruption and long-term ischaemic reperfusion brain injury. Nature communications, 7(1), 1-18.
136. Wang, R., Zhang, X., Zhang, J., Fan, Y., Shen, Y., Hu, W., & Chen, Z. (2012). Oxygen-glucose deprivation induced glial scar-like change in astrocytes. PLoS One, 7(5), e37574.
137. Spence, E. F., & Soderling, S. H. (2015). Actin out: regulation of the synaptic cytoskeleton. Journal of Biological Chemistry, 290(48), 28613-28622.
138. Tilve, S., Difato, F., & Chieregatti, E. (2015). Cofilin 1 activation prevents the defects in axon elongation and guidance induced by extracellular alpha-synuclein. Scientific reports, 5(1), 1-13.
139. Bamburg, J. R., Minamide, L. S., Wiggan, O. N., Tahtamouni, L. H., & Kuhn, T. B. (2021). Cofilin and actin dynamics: Multiple modes of regulation and their impacts in neuronal development and degeneration. Cells, 10(10), 2726.
140. Suurna, M. V., Ashworth, S. L., Hosford, M., Sandoval, R. M., Wean, S. E., Shah, B. M., ... & Molitoris, B. A. (2006). Cofilin mediates ATP depletion-induced endothelial cell actin alterations. American Journal of Physiology-Renal Physiology, 290(6), F1398-F1407.
141. Shaw, A. E., DeLuca, J. G., & Bamburg, J. R. (2012). ADF/cofilin regulates actomyosin assembly through competitive inhibition of myosin II binding to F-actin. Developmental cell, 22(3), 530-543.
142. Lekka, M., Laidler, P., Gil, D., Lekki, J., Stachura, Z., & Hrynkiewicz, A. Z. (1999). Elasticity of normal and cancerous human bladder cells studied by scanning force microscopy. European Biophysics Journal, 28(4), 312-316.

143. Rotsch, C., Jacobson, K., & Radmacher, M. (1999). Dimensional and mechanical dynamics of active and stable edges in motile fibroblasts investigated by using atomic force microscopy. Proceedings of the National Academy of Sciences, 96(3), 921-926.

144. Lekka, M., Pogoda, K., Gostek, J., Klymenko, O., Prauzner-Bechcicki, S., Wiltowska-Zuber, J., ... & Stachura, Z. (2012). Cancer cell recognition–mechanical phenotype. Micron, 43(12), 1259-1266.

145. Gardel, M. L., Shin, J. H., MacKintosh, F. C., Mahadevan, L., Matsudaira, P., & Weitz, D. A. (2004). Elastic behavior of cross-linked and bundled actin networks. Science, 304(5675), 1301-1305.

146. Guilluy, C., Osborne, L. D., Van Landeghem, L., Sharek, L., Superfine, R., Garcia-Mata, R., & Burridge, K. (2014). Isolated nuclei adapt to force and reveal a mechanotransduction pathway in the nucleus. Nature cell biology, 16(4), 376-381.

147. Hong-Lian, G., Chun-Xiang, L., Jian-Fa, D., Yu-Qiang, J., Xue-Hai, H., Zhao-Lin, L., ... & Dao-Zhong, Z. (2004). Mechanical properties of breast cancer cell membrane studied with optical tweezers. Chinese Physics Letters, 21(12), 2543.

148. Hochmuth, R. M. (2000). Micropipette aspiration of living cells. Journal of biomechanics, 33(1), 15-22.

149. Binnig, G., Quate, C. F., & Gerber, C. (1986). Atomic force microscope. Physical review letters, 56(9), 930.

150. Morris, V. J., Kirby, A. R., & Gunning, P. A. (2009). Atomic force microscopy for biologists. World Scientific.

151. Rotsch, C., & Radmacher, M. (2000). Drug-induced changes of cytoskeletal structure and mechanics in fibroblasts: an atomic force microscopy study. Biophysical journal, 78(1), 520-535.

152. Stylianou, A., Lekka, M., & Stylianopoulos, T. (2018). AFM assessing of nanomechanical fingerprints for cancer early diagnosis and classification: from single cell to tissue level. Nanoscale, 10(45), 20930-20945.

153. Allison, D. P., Mortensen, N. P., Sullivan, C. J., & Doktycz, M. J. (2010). Atomic force microscopy of biological samples. Wiley Interdisciplinary Reviews: Nanomedicine and Nanobiotechnology, 2(6), 618-634.

154. Stachurski, Z. H. (2009). Mechanical behavior of materials. Materials Today, 12(3), 44.

155. Ashby, M. F. (1992). Physical modelling of materials problems. Materials Science and Technology, 8(2), 102-111.

156. Silver, F. H. (1987). Biological materials: structure, mechanical propiertes, and modeling of soft tissues (No. 04; QP88. 23, S5.).

157. Lim, C. T., Zhou, E. H., & Quek, S. T. (2006). Mechanical models for living cells—a review. Journal of biomechanics, 39(2), 195-216.

158. Du, G., Ravetto, A., Fang, Q., & den Toonder, J. M. (2011). Cell types can be distinguished by measuring their viscoelastic recovery times using a micro-fluidic device. Biomedical microdevices, 13(1), 29-40.

159. Starodubtseva, M. N. (2011). Mechanical properties of cells and ageing. Ageing research reviews, 10(1), 16-25.

160. Wellbrock, C., Rana, S., Paterson, H., Pickersgill, H., Brummelkamp, T., & Marais, R. (2008). Oncogenic BRAF regulates melanoma proliferation through the lineage specific factor MITF. PloS one, 3(7), e2734.

161. Moeendarbary, E., & Harris, A. R. (2014). Cell mechanics: principles, practices, and prospects. Wiley Interdisciplinary Reviews: Systems Biology and Medicine, 6(5), 371-388.

162. Wolff, L., Fernandez, P., & Kroy, K. (2010). Inelastic mechanics of sticky biopolymer networks. New Journal of Physics, 12(5), 053024.

163. Verdier, C., Etienne, J., Duperray, A., & Preziosi, L. (2009). Rheological properties of biological materials. Comptes Rendus Physique, 10(8), 790-811.

164. Wells, R. G. (2013). Tissue mechanics and fibrosis. Biochimica et Biophysica Acta (BBA)-Molecular Basis of Disease, 1832(7), 884-890.

165. Radmacher, M., Fritz, M., Kacher, C. M., Cleveland, J. P., & Hansma, P. K. (1996). Measuring the viscoelastic properties of human platelets with the atomic force microscope.

166. Alcaraz, J., Buscemi, L., Grabulosa, M., Trepat, X., Fabry, B., Farré, R., & Navajas, D. (2003). Microrheology of human lung epithelial cells measured by atomic force microscopy. Biophysical journal, 84(3), 2071-2079.
167. Lekka, M. (2017). Cellular analysis by atomic force microscopy. Jenny Stanford Publishing.
168. González-Cruz, R. D., Fonseca, V. C., & Darling, E. M. (2012). Cellular mechanical properties reflect the differentiation potential of adipose-derived mesenchymal stem cells. Proceedings of the National Academy of Sciences, 109(24), E1523-E1529.
169. Szydlak, R., Majka, M., Lekka, M., Kot, M., & Laidler, P. (2019). AFM-based Analysis of Wharton's jelly mesenchymal stem cells. International Journal of Molecular Sciences, 20(18), 4351.
170. Raczkowska, J., Orzechowska, B., Patryas, S., Awsiuk, K., Kubiak, A., Kinoshita, M., ... & Lekka, M. (2020). Effect of substrate stiffness on physicochemical properties of normal and fibrotic lung fibroblasts. Materials, 13(20), 4495.
171. Orzechowska, B., Pabijan, J., Wiltowska-Zuber, J., Zemła, J., & Lekka, M. (2018). Fibroblasts change spreading capability and mechanical properties in a direct interaction with keratinocytes in conditions mimicking wound healing. Journal of Biomechanics, 74, 134-142.
172. Mathur, A. B., Collinsworth, A. M., Reichert, W. M., Kraus, W. E., & Truskey, G. A. (2001). Endothelial, cardiac muscle and skeletal muscle exhibit different viscous and elastic properties as determined by atomic force microscopy. Journal of biomechanics, 34(12), 1545-1553.
173. Spedden, E., White, J. D., Naumova, E. N., Kaplan, D. L., & Staii, C. (2012). Elasticity maps of living neurons measured by combined fluorescence and atomic force microscopy. Biophysical journal, 103(5), 868-877.
174. Zemła, J., Bobrowska, J., Kubiak, A., Zieliński, T., Pabijan, J., Pogoda, K., ... & Lekka, M. (2020). Indenting soft samples (hydrogels and cells) with cantilevers possessing various shapes of probing tip. European Biophysics Journal, 49(6), 485-495.

175. Tian, M., Li, Y., Liu, W., Jin, L., Jiang, X., Wang, X., ... & Shi, Y. (2015). The nanomechanical signature of liver cancer tissues and its molecular origin. Nanoscale, 7(30), 12998-13010.

176. Ansardamavandi, A., Tafazzoli-Shadpour, M., Omidvar, R., & Jahanzad, I. (2016). Quantification of effects of cancer on elastic properties of breast tissue by atomic force microscopy. Journal of the mechanical behavior of biomedical materials, 60, 234-242.

177. Plodinec, M., & Lim, R. Y. (2015). Nanomechanical characterization of living mammary tissues by atomic force microscopy. In Mammary Stem Cells (pp. 231-246). Humana Press, New York, NY.

178. Plodinec, M., Loparic, M., Monnier, C. A., Obermann, E. C., Zanetti-Dallenbach, R., Oertle, P., ... & Schoenenberger, C. A. (2012). The nanomechanical signature of breast cancer. Nature nanotechnology, 7(11), 757-765.

179. Puttini, S., Lekka, M., Dorchies, O. M., Saugy, D., Incitti, T., Ruegg, U. T., ... & Mermod, N. (2009). Gene-mediated restoration of normal myofiber elasticity in dystrophic muscles. Molecular Therapy, 17(1), 19-25.

180. Iyer, P. S., Mavoungou, L. O., Ronzoni, F., Zemla, J., Schmid-Siegert, E., Antonini, S., ... & Mermod, N. (2018). Autologous cell therapy approach for Duchenne muscular dystrophy using piggybac transposons and mesoangioblasts. Molecular Therapy, 26(4), 1093-1108.

181. Van Zwieten, R. W., Puttini, S., Lekka, M., Witz, G., Gicquel-Zouida, E., Richard, I., ... & Mermod, N. (2014). Assessing dystrophies and other muscle diseases at the nanometer scale by atomic force microscopy. Nanomedicine, 9(4), 393-406.

182. Puttini, S., van Zwieten, R. W., Saugy, D., Lekka, M., Hogger, F., Ley, D., ... & Mermod, N. (2013). MAR-mediated integration of plasmid vectors for in vivo gene transfer and regulation. BMC molecular biology, 14(1), 1-12.

183. Michalski, D., Härtig, W., Krueger, M., Hobohm, C., Käs, J. A., & Fuhs, T. (2015). A novel approach for mechanical tissue characterization indicates decreased elastic strength in brain areas affected by experimental thromboembolic stroke. Neuroreport, 26(10), 583.

184. Lopez, J. I., Kang, I., You, W. K., McDonald, D. M., & Weaver, V. M. (2011). In situ force mapping of mammary gland transformation. Integrative Biology, 3(9), 910-921.

185. Mohamed, M. S., Kobayashi, A., Taoka, A., Watanabe-Nakayama, T., Kikuchi, Y., Hazawa, M., ... & Wong, R. W. (2017). High-speed atomic force microscopy reveals loss of nuclear pore resilience as a dying code in colorectal cancer cells. ACS nano, 11(6), 5567-5578.

186. Ando, T. (2014). High-speed AFM imaging. Current opinion in structural biology, 28, 63-68.

187. Lyubchenko, Y. L. (2018). Direct AFM visualization of the nanoscale dynamics of biomolecular complexes. Journal of physics D: Applied physics, 51(40), 403001.

188. Crabb, R. A., Chau, E. P., Decoteau, D. M., & Hubel, A. (2006). Microstructural characteristics of extracellular matrix produced by stromal fibroblasts. Annals of biomedical engineering, 34(10), 1615-1627.

189. Kassies, R., Van der Werf, K. O., Lenferink, A., Hunter, C. N., Olsen, J. D., Subramaniam, V., & Otto, C. (2005). Combined AFM and confocal fluorescence microscope for applications in bio-nanotechnology. Journal of microscopy, 217(1), 109-116.

190. Stylianou, A., Politopoulos, K., Kyriazi, M., & Yova, D. (2011). Combined information from AFM imaging and SHG signal analysis of collagen thin films. Biomedical Signal Processing and Control, 6(3), 307-313.

191. Maver, U., Velnar, T., Gaberščec, M., Planinšek, O., & Finšgar, M. (2016). Recent progressive use of atomic force microscopy in biomedical applications. TrAC Trends in Analytical Chemistry, 80, 96-111.

192. Landry, J. J., Pyl, P. T., Rausch, T., Zichner, T., Tekkedil, M. M., Stütz, A. M., ... & Steinmetz, L. M. (2013). The genomic and transcriptomic landscape of a HeLa cell line. G3: Genes, Genomes, Genetics, 3(8), 1213-1224.

193. Seibenhener, M. L., & Wooten, M. W. (2012). Isolation and culture of hippocampal neurons from prenatal mice. JoVE (Journal of Visualized Experiments), (65), e3634.

194. Sader, J. E., Larson, I., Mulvaney, P., & White, L. R. (1995). Method for the calibration of atomic force microscope cantilevers. Review of Scientific Instruments, 66(7), 3789-3798.

195. Vlassak, J. J., & Nix, W. D. (1992). A new bulge test technique for the determination of Young's modulus and Poisson's ratio of thin films. Journal of materials research, 7(12), 3242-3249.

196. Pogoda, K., Jaczewska, J., Wiltowska-Zuber, J., Klymenko, O., Zuber, K., Fornal, M., & Lekka, M. (2012). Depth-sensing analysis of cytoskeleton organization based on AFM data. European Biophysics Journal, 41(1), 79-87.

197. Gostek, J., Prauzner-Bechcicki, S., Nimmervoll, B., Mayr, K., Pabijan, J., Hinterdorfer, P., ... & Lekka, M. (2015). Nano-characterization of two closely related melanoma cell lines with different metastatic potential. European Biophysics Journal, 44(1), 49-55.

198. Martens, J. C., & Radmacher, M. (2008). Softening of the actin cytoskeleton by inhibition of myosin II. Pflügers Archiv-European Journal of Physiology, 456(1), 95-100.

199. Kubiak, A., Zieliński, T., Pabijan, J., & Lekka, M. (2020). Nanomechanics in monitoring the effectiveness of drugs targeting the cancer cell cytoskeleton. International Journal of Molecular Sciences, 21(22), 8786.

200. Schliwa, M. (1982). Action of cytochalasin D on cytoskeletal networks. The Journal of cell biology, 92(1), 79-91.

201. Lekka, M., Laidler, P., Ignacak, J., Łabędź, M., Lekki, J., Struszczyk, H., ... & Hrynkiewicz, A. Z. (2001). The effect of chitosan on stiffness and glycolytic activity of human bladder cells. Biochimica et Biophysica Acta (BBA)-Molecular Cell Research, 1540(2), 127-136.

202. Ramos, J. R., Pabijan, J., Garcia, R., & Lekka, M. (2014). The softening of human bladder cancer cells happens at an early stage of the malignancy process. Beilstein journal of nanotechnology, 5(1), 447-457.

203. Barnes, J. M., Przybyla, L., & Weaver, V. M. (2017). Tissue mechanics regulate brain development, homeostasis and disease. Journal of cell science, 130(1), 71-82.

204. Lekka, M. (2016). Discrimination between normal and cancerous cells using AFM. Bionanoscience, 6(1), 65-80.

205. Sneddon, I. N. (1965). The relation between load and penetration in the axisymmetric Boussinesq problem for a punch of arbitrary profile. International journal of engineering science, 3(1), 47-57.

206. Rebelo, L. M., de Sousa, J. S., Mendes Filho, J., & Radmacher, M. (2013). Comparison of the viscoelastic properties of cells from different kidney cancer phenotypes measured with atomic force microscopy. Nanotechnology, 24(5), 055102.

207. Lee, W. T., Hong, S., Yoon, S. H., Kim, J. H., Park, K. A., Seong, G. J., & Lee, J. E. (2009). Neuroprotective effects of agmatine on oxygen-glucose deprived primary-cultured astrocytes and nuclear translocation of nuclear factor-kappa B. Brain research, 1281, 64-70.

208. Scudiero, D. A., Shoemaker, R. H., Paull, K. D., Monks, A., Tierney, S., Nofziger, T. H., ... & Boyd, M. R. (1988). Evaluation of a soluble tetrazolium/formazan assay for cell growth and drug sensitivity in culture using human and other tumor cell lines. Cancer research, 48(17), 4827-4833.

209. Vitriol, E. A., Wise, A. L., Berginski, M. E., Bamburg, J. R., & Zheng, J. Q. (2013). Instantaneous inactivation of cofilin reveals its function of F-actin disassembly in lamellipodia. Molecular biology of the cell, 24(14), 2238-2247.

210. Bravo-Cordero, J. J., Magalhaes, M. A., Eddy, R. J., Hodgson, L., & Condeelis, J. (2013). Functions of cofilin in cell locomotion and invasion. Nature reviews Molecular cell biology, 14(7), 405-415.

211. Bamburg, J. R., & Bernstein, B. W. (2010). Roles of ADF/cofilin in actin polymerization and beyond. F1000 biology reports, 2.

212. Fujii, Y., Koizumi, W. C., Imai, T., Yokobori, M., Matsuo, T., Oka, K., ... & Okajima, T. (2021). Spatiotemporal dynamics of single cell stiffness in the early developing ascidian chordate embryo. Communications biology, 4(1), 1-12.

213. Gnanachandran, K., Kędracka-Krok, S., Pabijan, J., & Lekka, M. (2022). Discriminating bladder cancer cells through rheological mechanomarkers at cell and spheroid levels. Journal of Biomechanics, 111346.

214. Kubiak, A., Chighizola, M., Schulte, C., Bryniarska, N., Wesołowska, J., Pudełek, M., ... & Lekka, M. (2021). Stiffening of DU145 prostate cancer cells driven by actin filaments–microtubule crosstalk conferring resistance to microtubule-targeting drugs. Nanoscale, 13(12), 6212-6226.

215. Kleman, A. M., Yuan, J. Y., Aja, S., Ronnett, G. V., & Landree, L. E. (2008). Physiological glucose is critical for optimized neuronal viability and AMPK responsiveness in vitro. Journal of neuroscience methods, 167(2), 292-301.

216. Lekka, M. (2022). Applicability of atomic force microscopy to determine cancer-related changes in cells. Philosophical Transactions of the Royal Society A, 380(2232), 20210346.

217. Xu, Z. S., Lee, R. J., Chu, S. S., Yao, A., Paun, M. K., Murphy, S. P., & Mourad, P. D. (2013). Evidence of changes in brain tissue stiffness after ischemic stroke derived from ultrasound-based elastography. Journal of Ultrasound in Medicine, 32(3), 485-494.

218. Discher, D. E., Janmey, P., & Wang, Y. L. (2005). Tissue cells feel and respond to the stiffness of their substrate. Science, 310(5751), 1139-1143.

219. Martens, J. C., & Radmacher, M. (2008). Softening of the actin cytoskeleton by inhibition of myosin II. Pflügers Archiv-European Journal of Physiology, 456(1), 95-100.

220. Fang, Y., Iu, C. Y., Lui, C. N., Zou, Y., Fung, C. K., Li, H. W., ... & Lai, K. W. (2014). Investigating dynamic structural and mechanical changes of neuroblastoma cells associated with glutamate-mediated neurodegeneration. Scientific Reports, 4(1), 1-10.

221. Korn, E. D., Carlier, M. F., & Pantaloni, D. (1987). Actin polymerization and ATP hydrolysis. Science, 238(4827), 638-644.

222. Aronoff, S. L., Berkowitz, K., Shreiner, B., & Want, L. (2004). Glucose metabolism and regulation: beyond insulin and glucagon. Diabetes spectrum, 17(3), 183-190.

223. Papakonstanti, E. A., & Stournaras, C. (2008). Cell responses regulated by early reorganization of actin cytoskeleton. FEBS letters, 582(14), 2120-2127.

224. Moriyama, K., Iida, K., & Yahara, I. (1996). Phosphorylation of Ser-3 of cofilin regulates its essential function on actin. Genes to Cells, 1(1), 73-86.

225. Li, H., Yang, J., Chu, T. T., Naidu, R., Lu, L., Chandramohanadas, R., ... & Karniadakis, G. E. (2018). Cytoskeleton remodeling induces membrane stiffness and stability changes of maturing reticulocytes. Biophysical Journal, 114(8), 2014-2023.

226. Guo, C. Y., Xiong, T. Q., Tan, B. H., Gui, Y., Ye, N., Li, S. L., & Li, Y. C. (2019). The temporal and spatial changes of actin cytoskeleton in the hippocampal CA1 neurons following transient global ischemia. Brain Research, 1720, 146297.

227. Kamal, A., & Goldstein, L. S. (2000). Connecting vesicle transport to the cytoskeleton. Current opinion in cell biology, 12(4), 503-508.

228. Perlson, E., Maday, S., Fu, M. M., Moughamian, A. J., & Holzbaur, E. L. (2010). Retrograde axonal transport: pathways to cell death?. Trends in neurosciences, 33(7), 335-344.

229. Song, M., & Yu, S. P. (2014). Ionic regulation of cell volume changes and cell death after ischemic stroke. Translational stroke research, 5(1), 17-27.

230. Hellas, J. A., & Andrew, R. D. (2021). Neuronal swelling: a non-osmotic consequence of spreading depolarization. Neurocritical Care, 35(2), 112-134.

231. Rungta, R. L., Choi, H. B., Tyson, J. R., Malik, A., Dissing-Olesen, L., Lin, P. J., ... & MacVicar, B. A. (2015). The cellular mechanisms of neuronal swelling underlying cytotoxic edema. Cell, 161(3), 610-621.

232. Wang, Y., Blandino, G., Oren, M., & Givol, D. (1998). Induced p53 expression in lung cancer cell line promotes cell senescence and differentially modifies the cytotoxicity of anti-cancer drugs. Oncogene, 17(15), 1923-1930.

233. Raynaud, F., & Marcilhac, A. (2006). Implication of calpain in neuronal apoptosis: a possible regulation of Alzheimer's disease. The FEBS journal, 273(15), 3437-3443.

234. Kalogeris, T., Baines, C. P., Krenz, M., & Korthuis, R. J. (2012). Cell biology of ischemia/reperfusion injury. International review of cell and molecular biology, 298, 229-317.

235. Cross, J. L., Meloni, B. P., Bakker, A. J., Lee, S., & Knuckey, N. W. (2010). Modes of neuronal calcium entry and homeostasis following cerebral ischemia. Stroke research and treatment, 2010.

236. Carinci, M., Vezzani, B., Patergnani, S., Ludewig, P., Lessmann, K., Magnus, T., ... & Giorgi, C. (2021). Different roles of mitochondria in cell death and inflammation: Focusing on mitochondrial quality control in ischemic stroke and reperfusion. Biomedicines, 9(2), 169.

237. Chen, H., Yoshioka, H., Kim, G. S., Jung, J. E., Okami, N., Sakata, H., ... & Chan, P. H. (2011). Oxidative stress in ischemic brain damage: mechanisms of cell death and potential molecular targets for neuroprotection. Antioxidants & redox signaling, 14(8), 1505-1517.

238. Pollard, T. D., Blanchoin, L., & Mullins, R. D. (2000). Molecular mechanisms controlling actin filament dynamics in nonmuscle cells. Annual review of biophysics and biomolecular structure, 29(1), 545-576.

239. Brunello, E., Fusi, L., Ghisleni, A., Park-Holohan, S. J., Ovejero, J. G., Narayanan, T., & Irving, M. (2020). Myosin filament-based regulation of the dynamics of contraction in heart muscle. Proceedings of the National Academy of Sciences, 117(14), 8177-8186.

240. Schaks, M., Giannone, G., & Rottner, K. (2019). Actin dynamics in cell migration. Essays in Biochemistry, 63(5), 483-495.

241. Le, S., Yu, M., Bershadsky, A., & Yan, J. (2020). Mechanical regulation of formin-dependent actin polymerization. In Seminars in Cell & Developmental Biology (Vol. 102, pp. 73-80). Academic Press.

242. Kuiper, J. W. P., Pluk, H., Oerlemans, F., Van Leeuwen, F. N., De Lange, F., Fransen, J., & Wieringa, B. (2008). Creatine kinase–mediated ATP supply fuels actin-based events in phagocytosis. PLoS biology, 6(3), 0568–0580.

243. Mathews, E. H., Stander, B. A., Joubert, A. M., & Liebenberg, L. (2014). Tumor cell culture survival following glucose and glutamine deprivation at typical physiological concentrations. Nutrition, 30(2), 218-227.

244. Hoshi, Y., Okabe, K., Shibasaki, K., Funatsu, T., Matsuki, N., Ikegaya, Y., & Koyama, R. (2018). Ischemic brain injury leads to brain edema via hyperthermia-induced TRPV4 activation. Journal of Neuroscience, 38(25), 5700-5709.

245. Tornabene, E., Helms, H. C. C., Pedersen, S. F., & Brodin, B. (2019). Effects of oxygen-glucose deprivation (OGD) on barrier properties and mRNA

transcript levels of selected marker proteins in brain endothelial cells/astrocyte co-cultures. PLoS One, 14(8), e0221103.

246. Alhadidi, Q., Bin Sayeed, M. S., & Shah, Z. A. (2016). Cofilin as a promising therapeutic target for ischemic and hemorrhagic stroke. Translational stroke research, 7(1), 33-41.

247. Xu, M. S., Yin, L. M., Cheng, A. F., Zhang, Y. J., Zhang, D., Tao, M. M., ... & Shan, C. L. (2021). Cerebral ischemia-reperfusion is associated with upregulation of cofilin-1 in the motor cortex. Frontiers in Cell and Developmental Biology, 9, 634347.

9. List of Figures

Figure 3.16. Illustration of the AFM-based microrheological measurements. Cantilever deflection is measured while applying sinusoidal oscillations at a constant amplitude to the sample. The oscillation amplitude is kept constant during the measurements. The oscillation frequency changes (here, f_1 to f_4).

Figure 3.17. Example of storage G' and loss G'' moduli plotted as a function of the oscillation frequency. The plot is in log scale, and the transition frequency, where the storage and loss moduli are equivalent, is indicated by a green dashed line.

Figure 3.18. The idea of a single-cell effective surface area (SA) determination based on fluorescent images of HeLa cells.

Figure 4.1. Morphology and organization of actin cytoskeleton of U118 MG (a) and HeLa (b) cells, observed under the epi-fluorescent microscope. Staining: actin filaments – phalloidin conjugated with Alexa Fluor 488 dye, cell nuclei – Hoechst 33342 dye.

Figure 4.2. Epi-fluorescence images of cell morphology in control and cyto D treated U118 MG and HeLa cells. Staining: actin filaments – phalloidin conjugated with Alexa Fluor 488 dye, cell nuclei – Hoechst 33342 dye.

Figure 4.3. The effective spreading area of a single U118 MG and HeLa cell before and after cyto D treatment for 10 and 30 min, respectively. Data are expressed as mean with standard error.

Figure 4.4. Young's modulus of U118 MG (a) and HeLa (b) cells before and after cytoD, determined for the indentations of 200 nm and 800 nm. Data are expressed as mean with standard error. Statistical significance determined: $p > 0.05$, $^{*}p < 0.05$, $^{**}p < 0.01$, $^{***}p < 0.001$.

Figure 4.5. R factor, defined as a ratio between Young's modulus determined at 200 nm and 800 nm, for U118 MG (a) and HeLa (b) cells before and after cytochalasin D

treatment. Data are expressed as mean with standard error. Statistically significant changes were not observed.

Figure 5.1. Elasticity maps, recorded using SH-SY5Y cells after OGD and RO. Control cells (C, in NB(+G)), OGD cells (OGD 1h, 3h, or 12h, in NBA(-G)), reoxygenated OGD cells (RO 24h, in DMEM(+G)) QI mode, of control and OGD-treated SH-SY5Y cells.

Figure 5.2. Young's modulus of neuroblastoma SH-SY5Y cells exposed to OGD, determined for the indentation depths of 400 nm (a) and 1200 nm (b). Box plots show a median (line); a mean (solid square); standard deviation (box); 25% and 75% percentiles (box); $n = 60$ cells (notation: C – control cells in NB(+G)), OGD cells (OGD 1h, 3h, or 12h, NBA(-G)), reoxygenated OGD cells (RO 24h, DMEM(+G)), and control, non-OGD cells (C 24h) cultured in the same conditions as reoxygenated OGD cells), Statistical significance: *ns* – not significant ($p > 0.05$), $*p < 0.05$, $**p < 0.01$, $***p < 0.001$ (reprinted from Zielinski et al. *Scientific Reports* **12** (2022) 16276 under CC-BY 4.0 license).

Figure 5.3. Viability and metabolic activity of SH-SY5Y neuroblastoma cells after OGD exposure and following 24h RO. (a, b) LDH results are represented by the mean value calculated from 12 ELISA readouts after normalization of relative absorbance to values obtained for the control samples. (c, d) MTS results show a distribution of single dots (one dot refers to one readout from the ELISA reader). A mean (open square), median (middle black line), and standard deviation (black line above and below a middle one) were determined from data gathered in 3 independent repetitions. Statistical significance: $p > 0.05$, $*p < 0.05$, $***p < 0.001$, *ns* – not statistically significant (reprinted from Zielinski et al. *Scientific Reports* **12** (2022) 16276 CC-BY 4.0 license).

Figure 5.4. Phase-contrast images of SH-SY5Y cells after OGD and RO. Control cells (C, in NB(+G)), OGD cells (OGD 1h, 3h, or 12h, in NBA(-G)), reoxygenated OGD cells (RO 24h, in DMEM(+G)), and control, non-OGD cells (C 24h, in DMEM(+G)). Scale bar 50 µm (reprinted from Zielinski et al. *Scientific Reports* **12** (2022) 16276 under CC-BY 4.0 license).

Figure 5.5. Confocal images of the actin and microtubular cytoskeleton in OGD-treated cells immediately after exposure. C (C, NB(+G)), OGD cells (OGD 1h, 3h, or 12h,NBA(-G)). Actin filaments were labeled with phalloidin conjugated with Alexa Fluor 488, microtubules with primary antibody conjugated with Cy3, and cell nuclei with Hoechst33342; scale bar 25 μm (reprinted from Zielinski et al. *Scientific Reports* **12** (2022) 16276 under CC-BY 4.0 license).

Figure 5.6. Confocal images of the actin and microtubular cytoskeleton in OGD-treated cells after 24h re-oxygenation. C (non-OGD cells (C 24h) kept in DMEM(+G) for the same time as reoxygenated OGD cells), OGD (reoxygenated OGD cells (RO 24h, DMEM(+G)). Actin filaments were labeled with phalloidin conjugated with Alexa Fluor 488, microtubules with primary antibody conjugated with Cy3, and cell nuclei with Hoechst33342; scale bar 25 μm (reprinted from Zielinski et al. *Scientific Reports* **12** (2022) 16276 under CC-BY 4.0 license).

Figure 5.7. The effective spreading surface area of a single cell (SA) of SH-SY5Y cells after OGD (a) and following re-oxygenation (b). A single dot is the average surface area of individual cells. Boxplot represents mean (open square), median (black line), standard deviation (box), and 25% and 75% percentiles (whiskers) from $n = 60$ fluorescent images. Statistical significance determined: $p > 0.05$, $^{*}p < 0.05$, $^{***}p < 0.001$, and *ns* – not statistically significant (reprinted from Zielinski et al. *Scientific Reports* **12** (2022) 16276 under CC-BY 4.0 license).

Figure 5.8. Nucleus to the cytoplasm (*N/C*) ratio of SH-SY5Y cells after OGD and following re-oxygenation. Single dots represent the average value of individual cells. Boxplots show mean (open square), median (line), and standard deviation (box) calculated from $n = 60$ cells. Statistical significance: $^{*}p < 0.05$, $^{***}p < 0.001$, *ns* – not statistically significant (reprinted from Zielinski et al. *Scientific Reports* **12** (2022) 16276 under CC-BY 4.0 license).

Figure 5.9. Expression of cofilin and phospho-cofilin (p-cofilin) corresponding to actin-severing activity in SH-SY5Y cell line evaluated immediately after 1h (a) and 12h (b)

OGD exposure. Control cells were kept in NB(+G), while OGD cells were kept in NBA(-G). A mean (black square), median (black middle line), and standard deviation (SD, black lines below and above the middle one) were obtained from 3 independent repetitions. Statistical significance: ***p* < 0.01, ****p* < 0.001, *ns* – not statistically significant (reprinted from Zielinski et al. *Scientific Reports* **12** (2022) 16276 under CC-BY 4.0 license).

Figure 6.1. Young's modulus of neurons exposed to OGD at two oxygen concentrations (5% and 0.1%). The total number of neurons measured for each condition was 30. Box-plot represents mean (square), median (middle line), and standard deviation (SD, outside lines) were obtained from at least 3 independent repetitions. Statistical significance (*ns* – not statistically significant, **p* < 0.05).

Figure 6.2. Nanomechanical properties of mice primary hippocampal neurons after OGD treatment, quantified by the apparent Young's modulus calculated for the indentation depth of 400 nm **(a)** and 1200 nm **(b)**. Notation: C – control, untreated neurons cultured in NB(+G)); C 1h & C 3h – sham-operated controls (untreated neuron culture in which NB(+G) was replaced with NB(G+) kept in culture for 1 and 3h, respectively; OGD 1h & OGD 3h – neurons exposed to OGD for 1h and 3h, in NBA(-G) medium. Box plots represent mean (square), median (middle line), and standard deviation (SD, outside lines) were obtained from at least 3 independent repetitions. Statistical significance (**p* < 0.05; ***p* < 0.01).

Figure 6.3. The log-log relations of the storage G’ (black dots) and loss G” (red dots) moduli plotted as a function of the frequency of oscillation of mice primary neurons exposed to (a) control (C), (b) sham-operated control (C 1h), (c) OGD 1h, and (d) OGD 3h. Each point denotes a mean and standard deviation of 30 to 50 neurons.

Figure 6.4. Epi-fluorescence images of mice primary hippocampal neurons stained with live/dead assay. Notation: C – control, untreated cells (NB(+G)); C 1h – sham-operated control NB(+G) exchanged to NB(+G); OGD 1h & OGD 3h – OGD treated neurons (NB(+G) exchanged to NBA(-G)), RO 24h – reoxygenated neurons in the corresponding

culture conditions. Staining: green – calcein-AM fluorescence marking living neurons; red – propidium iodide intercalated with DNA, indicating dead neurons.

Figure 6.5. Neuron viability determined directly after OGD exposure (a) and after 24 h of re-oxygenation (b). Notation: C – control, untreated cells (NB(+G)); C S-O – sham-operated control NB(+G) exchanged to NB(+G); OGD 1h & OGD 3h – OGD treated neurons (NB(+G) exchanged to NBA(-G)), R-O 24h – reoxygenated neurons in the corresponding culture conditions. A mean (square), median (middle line), and standard deviation (SD, outside lines) were obtained from 3 independent repetitions. Statistical significance (*ns* – not statistically significant, ***$p< 0.001$).

Figure 6.6. Confocal images of the actin cytoskeleton in OGD-treated cells. Notation: C – control, untreated cells (NB(+G)); C 1h – sham-operated control NB(+G) exchanged to NB(+G); OGD 1h & OGD 3h – OGD treated neurons (NB(+G) exchanged to NBA(-G)), R-O 24h – reoxygenated neurons in the corresponding culture conditions. Staining: actin filaments (green) – phalloidin conjugated with Alexa Fluor 488, cell nuclei (blue) – Hoechst33342.

Figure 6.7. Confocal images of the microtubular cytoskeleton in OGD-treated cells. Notation: C – control, untreated cells (NB(+G)); C 1h – sham-operated control NB(+G) exchanged to NB(+G); OGD 1h & OGD 3h – OGD treated neurons (NB(+G) exchanged to NBA(-G)), R-O 24h – reoxygenated neurons in the corresponding culture conditions. Staining: microtubules (red) – primary antibody conjugated with Cy3, cell nuclei (blue) – Hoechst33342.

Figure 6.8. AFM topography images of neurons exposed to OGD compared to control, untreated cells, and sham-operating control. Notation: C – control, untreated cells (NB(+G)); C 1h – sham-operated control NB(+G) exchanged to NB(+G); OGD 1h & OGD 3h – OGD treated neurons (NB(+G) exchanged to NBA(-G)), RO 24h – reoxygenated neurons in the corresponding culture conditions.

Figure 6.9. (a) Exemplary Western blot showing cofilin and phospho-cofilin expression in OGD-treated neurons, accompanied by densitometry-based quantification of the relative expression level. **(b)** A mean and standard deviation were calculated from data gathered from 3 independent repetitions. Notation: C – control, untreated cells (NB(+G)); C 1h – sham-operated control NB(+G) exchanged to NB(+G); OGD 1h & OGD 3h – OGD treated neurons (NB(+G) exchanged to NBA(-G)), RO 24h – reoxygenated neurons in the corresponding culture conditions.